Chapter 7
Instrument Packages

Richard E. Cofield, William A. Imbriale, and Richard E. Hodges

This chapter describes antennas used on various instrument packages for science spacecraft. The instruments have been primarily used for the Earth Observing System (EOS), a series of spacecraft to observe Earth from the unique vantage point of space. This chapter includes radiometers (7.1–7.3), scatterometers (7.4), radars (7.5), and altimeters (7.6).

7.1 Radiometers

Richard E. Cofield

Radiometry is the measurement of electromagnetic radiation using highly sensitive receivers. The blackbody radiation spectrum given by Planck's radiation law provides a reference against which the radiation spectra of real bodies at the same physical temperature are compared. The spectral, polarization, and angular variations of a scene of interest are dictated by the geometrical configuration and physical properties (dielectric and thermal) of surfaces and interior regions of (1) the materials under study, and (2) the medium (atmosphere or space) through which we make observations. Radiometer parameters (such as frequency, viewing angle, and polarization) can be chosen to relate the radiometer's output signal strength to properties of the observed scenes.

This section describes passive microwave radiometry from spaceborne instruments developed at Jet Propulsion Laboratory (JPL): passive in contrast to active (radio detection and ranging [radar] or laser induced differential absorption radar [lidar]) systems such as altimeters and the scatterometers discussed below, and microwave as a consequence of Planck's law at the

temperature ranges of natural emitters. Hence, it is convenient to express radiometric signals (radiant power per unit bandwidth) as radiances having units of temperature (kelvin, or K). These radiances vary from 0 to 500 K for Earth and atmosphere, planets and other Solar System objects aside from the Sun itself. Microwave radiometric techniques were first developed from radio astronomy programs measuring electromagnetic energy of extraterrestrial origin. Thus, the requirements levied on spaceborne microwave radiometers are similar to those found in radio astronomy: spatial requirements include resolution (beamwidth), pointing accuracy and knowledge, polarization purity, and some measure of how well the antenna rejects energy from angles other than those desired (directivity, or beam efficiency). For super-heterodyne radiometers, spectral requirements usually appear as bandwidth about the center local oscillator frequency.

7.1.1 Microwave (Atmospheric) Sounder Unit

The Television Infrared Observation Satellite (TIROS)-N microwave sounder unit (MSU) is a direct descendant of the Scanning Microwave Spectrometer (SCAMS) flown in Earth orbit aboard the NIMBUS-6 meteorological satellite in 1975 [1]; SCAMS itself descends from the microwave radiometer flown in 1962 aboard Mariner 2 for remote sensing of the atmosphere of Venus. MSU observes thermal emission on the lower-side wing of the 60-gigahertz (GHz) oxygen line complex (at 50, 54, 55, and 58 GHz) for retrieving atmospheric temperature profiles. In the vertical temperature sounding technique, the radiometer sees thermal emission from frequency-dependent depths in the atmosphere, as determined by radiative transfer with Doppler and collisional broadening of wings of the oxygen line. For the MSU frequencies, the height of atmosphere parcels contributing to radiation varies from 0 (the surface) up to about 20 km. Twelve instrument units were delivered for temperature profiling aboard National Oceanic and Atmospheric Administration (NOAA) operational satellites.

7.1.1.1 Antenna Requirements. In order to meet a mission requirement of 1 K or better long term absolute instrument accuracy, the MSU footprint along the satellite ground track was to subtend 7.5-deg half-power beamwidth (HPBW) at the antenna, with a main beam efficiency >95 percent. (For Earth remote-sensing radiometers, beam efficiency is typically defined as the fraction of radiated power within 2.5 × the HPBW; the factor relates HPBW to the width between first nulls of the Airy pattern.) Horizontal resolution is provided by scanning the antenna field of view (FOV) at 11 positions across the ground track. With a scan of ±47.5 deg, the ground footprint size from a satellite height of 830 km varies from a 109-km circle at nadir to a 177 × 323-km ellipse at the scan extrema.

Additional scan positions permit radiometric calibration by directing the radiometer view to cold space (3 K) and to an ambient temperature black-body target (290 K). The scan period, including calibration, is 25.6 s.

7.1.1.2 Antenna Design. The antennas consist of two scanning reflectors fed at a 45-deg incidence angle in the near field of two fixed corrugated feed horns, Fig. 7-1. The scan axis, feed boresight, and spacecraft velocity vector all coincide. The reflectors have projected aperture diameters of 6 cm, and they are figured as hyperbolas slightly perturbed from parabolas, in order to reduce the frequency dependence of HPBW, from 15 percent (diffraction limited) to a measured range of 6 percent residual from non-ideal horn patterns and alignment. At the throat of each feed horn, an orthomode transducer separates the signal by polarization, resulting in the final four channels, which are then Dicke-switched before detection [2].

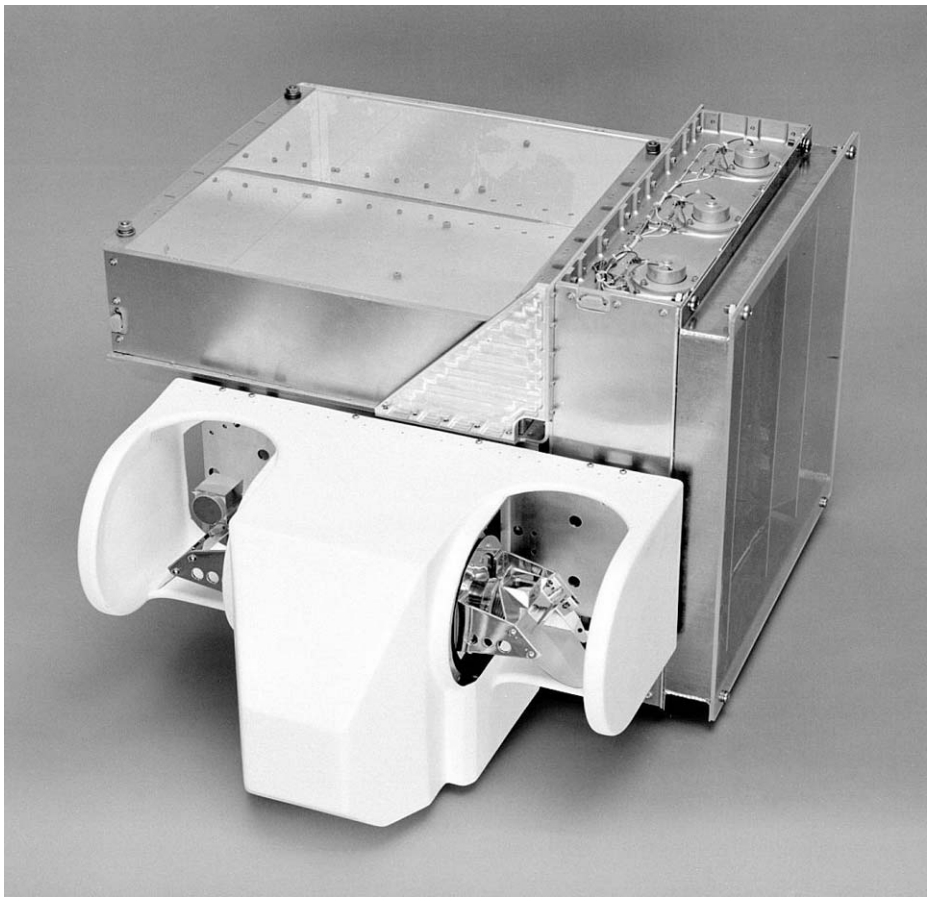

Fig. 7-1. TIROS microwave sounder unit (MSU).

7.1.1.3 Performance Estimates. The antenna patterns of the MSU instruments were measured in the far field at the JPL antenna test range. Complete patterns were measured at azimuth angle spacings of 22.5 deg for the first four units, then in principal planes and at selected scan positions for the remaining eight. The measurement's dynamic range was better than –51 dB, and amplitude measurement accuracy was 3 percent. These imply 10 percent accuracy in the knowledge of sidelobes –41 dB down from the main beam peak, corresponding to the required 95-percent beam efficiency. Angular resolution was 0.3 deg, and the polarization angle between MSU and mechanical alignment features was determined to <1 deg. Since the flight data reductions do not depend on polarization purity (atmospheric radiances for temperature sounding are uncorrelated and unpolarized), the co- and cross-polarized patterns were summed in quadrature to calculate beam efficiency (i.e., the only degradation caused here by cross-polarization is broadening of the antenna pattern). This is true of most atmospheric remote sensing of gaseous constituents (as opposed to ice clouds), with a few exceptions such as Zeeman splitting of oxygen emission in the mesosphere [3].

Antenna performance of a typical MSU is shown in Table 7-1. The beam efficiency met requirements, as did the beamwidth averaged over principal planes.

Space qualification of the MSU included extensive environmental tests, including a thermal vacuum test in which the radiometer was operated in vacuum over a temperature range exceeding that which would be seen in space. For this test, black-body targets like those used for on-board calibration were fabricated of iron-loaded epoxy and oriented for Brewster-angle incidence to achieve nearly unity emissivity. These targets were placed in front of the antennas, and their temperatures controlled in 25-K steps from 100 to 350 K to simulate cold space and the Earth [4]. This testing verified the linearity of the calibration of antenna temperatures to <1 percent, with a post fit residual of 0.5 K. Similar targets have been used for ground testing and on-board calibration in most of the spaceborne microwave radiometers subsequently flown by JPL.

Table 7-1. Antenna performance of MSU unit 4, from [2].

Frequency (GHz)	50.30	53.74	54.96	57.95
RF bandwidth (MHz)		220		
Beamwidth (deg)	7.8 × 7.1	7.3 × 7.0	7.6 × 7.3	7.3 × 7.0
Beam efficiency (percent)	95.3	95.5	95.2	97.4
Mass (kg)		29		
Power (W)		30		

7.1.1.4 Mission Status and Conclusions. The first of the TIROS-N/NOAA satellites was launched on October 13, 1978, and the MSU instruments continued to be deployed through the NOAA-J(14) satellite on December 1994, from which the MSU continues to operate to the present. Comparisons with ground truth for the first two satellites showed the MSU agreed to 0.5 K with the high resolution infrared sounder (on the same spacecraft), and to 3 K with a U.S. National Meteorological Center grid of radiosonde data. The latter improved to 1.5 K over a restricted height range corresponding to 300–700 hectopascals (hPa) pressure. This nearly meets the mission requirement of 1 K.

In a subsequent follow-on to the operational satellite series (NOAA K/L/M), the MSU has been replaced by the advanced microwave sounder unit (AMSU) for which the measurement channels extend from 50 to 183 GHz to include water vapor line spectroscopy. AMSU is supplied by an external vendor to NOAA and the Goddard Space Flight Center (GSFC), with scientific oversight by JPL.

7.1.2 Scanning Multichannel Microwave Radiometer on Seasat and Nimbus 7

The scanning multichannel microwave radiometer (SMMR) is a five-frequency imaging microwave radiometer launched on the Seasat-A and Nimbus-7 satellites. It measures dual-polarized radiation at 6.63, 10.69, 18, 21, and 37 GHz from Earth's atmosphere and surface. Geophysical quantities retrieved from these 10 channels include sea surface temperature and wind speed, sea-ice age and coverage, and atmospheric water in the forms of vapor, cloud, and rain. Sea surface temperature was the primary objective in the Seasat mission. The antenna system was designed for a 42-deg conical scan, covering a 50-deg swath angle in a sinusoidal motion of the reflector having a 4-s period. The choice of nadir angle gives an incidence angle favorable to temperature sensing [5,6]. The antenna feeds six Dicke-switched heterodyne radiometers: one for each polarization of 37 GHz, and one for each of the lower frequencies, with polarization switched on alternate scans.

7.1.2.1 Antenna Requirements. Table 7-2 summarizes the requirements for the SMMR antenna. Since collocation of footprints was critical to the science of both NIMBUS-7 and Seasat measurements, the design selected for SMMR was an offset-fed parabolic reflector coupled to a single feed horn having a novel design and arrangement of ports to accommodate the 10 radiometer channels.

In order to meet beamwidth and beam efficiency requirements, the clear aperture diameter was 79 cm. Strut brackets were attached to the periphery of the physical reflector diameter of 83 cm.

Table 7-2. SMMR antenna requirements.

Parameter	Values				
Frequency (GHz)	6.633	10.69	18	21	37
Tolerance (MHz), (1σ)	5	8	14	16	28
Antenna 3-dB beamwidth (deg)	4.2	2.6	1.6	1.4	0.8
Tolerance (deg), (1σ)	0.2	0.15	0.1	0.1	0.1
Polarization isolation (dB)	>25				
Pointing accuracy (deg), (1σ)	0.1				
Solid-angle beam efficiency	>87 percent				

The parent paraboloid diameter (D_p) of 173 cm and focal length (f) of 52 cm give f/D_p = 0:3, the minimum ratio for which reflector-induced cross-polarization would be <–25 dB as required. Reflector construction was of graphite/epoxy, with vacuum-deposited aluminum for both radio frequency (RF) performance and thermo-optical properties. The system of tubular struts, arranged to form a hexapod truss supporting the reflector at three points, was accepted despite the added blockage, after modal vibration testing of a breadboard model revealed that unacceptable deflections would occur during launch. Shims under the struts were used to boresight the beams and adjust focus. To achieve the conical scan, bearings and a drive mechanism were placed between the shim plates and the horn.

The reflector's as-manufactured contour was specified to be within 0.07 mm root mean square (rms) from the best fit paraboloid. Worst-case allowable thermal distortion was <0.25 mm to avoid pattern degradation. The antenna was to have a 100-Hz minimum resonant frequency. To minimize contamination by stray radiance, the design allowed <0.1 percent of antenna spillover energy and <7 percent of feed spillover energy to illuminate the spacecraft.

The multi-frequency feed horn (Fig. 7-2(a)) was the most innovative item in the SMMR design. A ring-loaded corrugated horn extends bandwidth beyond the octave characteristic of simple corrugations, to 3:1. Moreover, it was noted that capacitive surface impedance would recur at odd multiples of the fundamental range. Thus, if designed for 6–18 GHz, the surface should also be capacitive between 18 = 3 × 6 and 54 = 3 × 18 GHz. Orthogonal pairs of slots (one for radiometer input and another, cavity backed, for pattern symmetry) were placed at appropriate points in the side of the feed cone, along with the orthomode transducers to input the conventional highest modes through the vertex. This horn could then launch frequencies of any reasonably wide spacing with good polarization isolation.

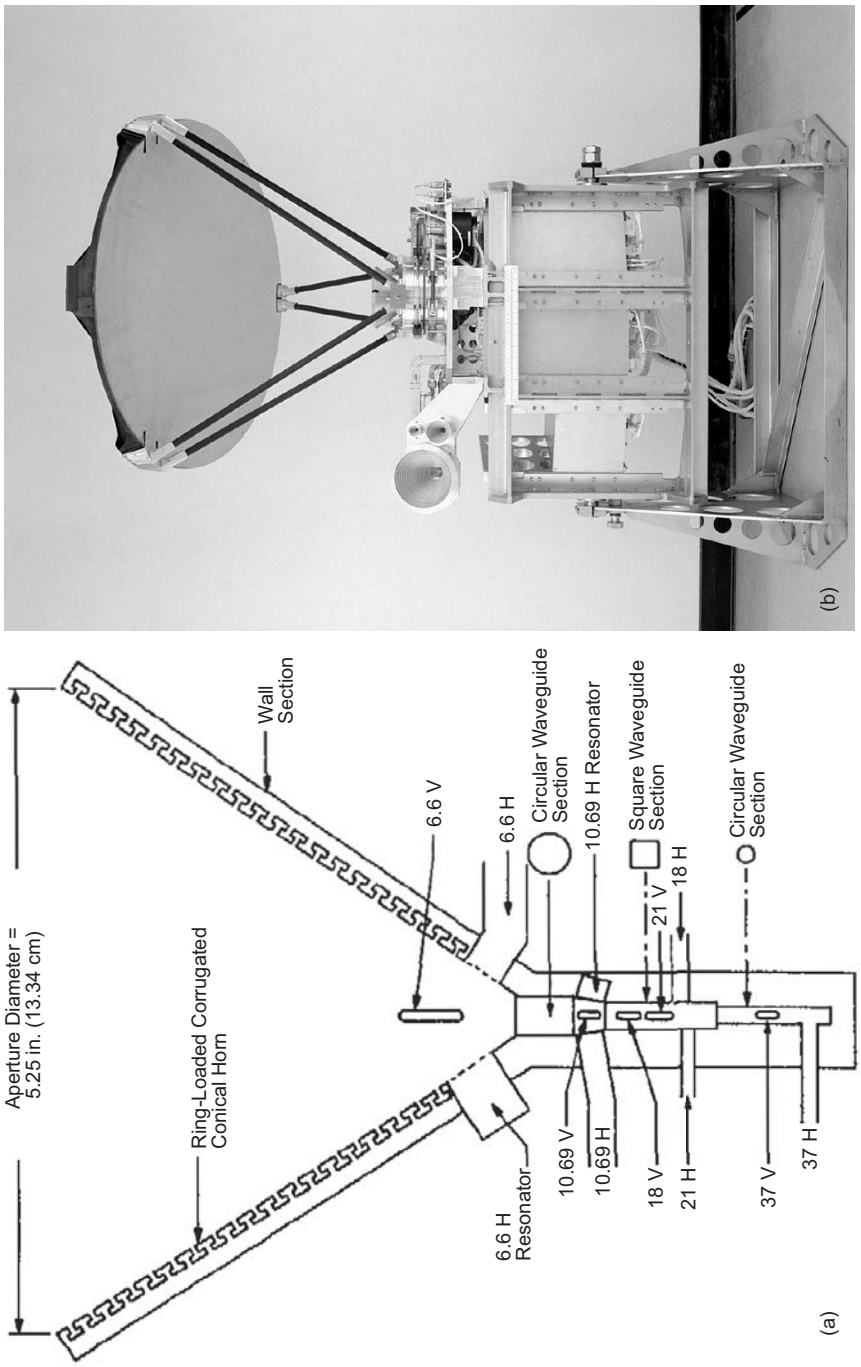

Fig. 7-2. Scanning multichannel microwave radiometer (SMMR) on Seasat-A and Nimbus-7: (a) multi-frequency feed horn (MFFH) and (b) assembled instrument.

The reflector was simulated during feed development tests using a lens sized to have the same edge taper (–22 dB) as the reflector. Coincidence of phase centers was verified by the lens collimating all frequencies simultaneously. The resulting design yielded highly efficient dual polarized primary patterns with nearly constant beamwidths at each of five frequencies needed in a 6:1 band. Near sidelobes ranged from –22 to –25 dB below the main beam [7].

Figure 7-2(b) is a photograph of the SMMR instrument. Antenna patterns of the fully assembled SMMR were measured on a 1200-foot (366-m) far-field range, over the entire 4π solid angle. Patterns at the three lowest frequencies (6.6, 10.69, and 18 GHz) showed that variation with scan angle, due to polarization rotation and to varying effects of the backup structure, was both weak and antisymmetric about a vertical plane through the antenna. Therefore, characterization for all frequencies was done at 0 deg and +25 deg only. Patterns were measured in amplitude only, since the radiances observed are incoherent; but one quantity, the relative phase between co- and cross-polarized patterns (β_p, where $p = h$ or v), was found to be needed by the data processing algorithms only after patterns were measured, and had to be estimated from subsets of in-flight data as a pseudo-geophysical quantity.

Figure 7-3 shows contours of amplitude patterns of the SMMR instrument at a particular scan position, frequency, and polarization. The pair of cross-polarization lobes about 20 dB down from the co-polarized main lobe are characteristic of offset-fed parabolic reflector antennas. The plots also show asymmetry in the sidelobes below –15 dB, which is attributed to the support struts. Numerical integration of the measured patterns provides the beam efficiencies and polarization isolations in Table 7-3. Beam efficiencies include both co- and cross-polarized power.

One science objective for the SMMR, to retrieve sea surface temperature with better than 1.5 deg C accuracy, imposed a stringent requirement for antenna pattern correction (APC), which inverts the set of antenna temperatures T_A to produce scene radiance, or (in the Rayleigh-Jeans limit) brightness temperatures T_B. These corrections can be quite large, due to (1) the disappointing beam efficiencies measured, and (2) a polarization coupling due partly to the 20-dB cross polarization but mostly to the feed horn remaining fixed while the reflector scans. The APC algorithm developed for SMMR and described in [8] corrected for these and other affects, such as spacecraft-attitude errors, Faraday rotation through the ionosphere, and retrieval of the relative phase β_p as a geophysical parameter.

In designing the SMMR, the reflector support struts had been expected to block 0.6 percent of the clear aperture area, all in the outer portion where RF illumination would be low. However, as Table 7-3 shows scattering from the

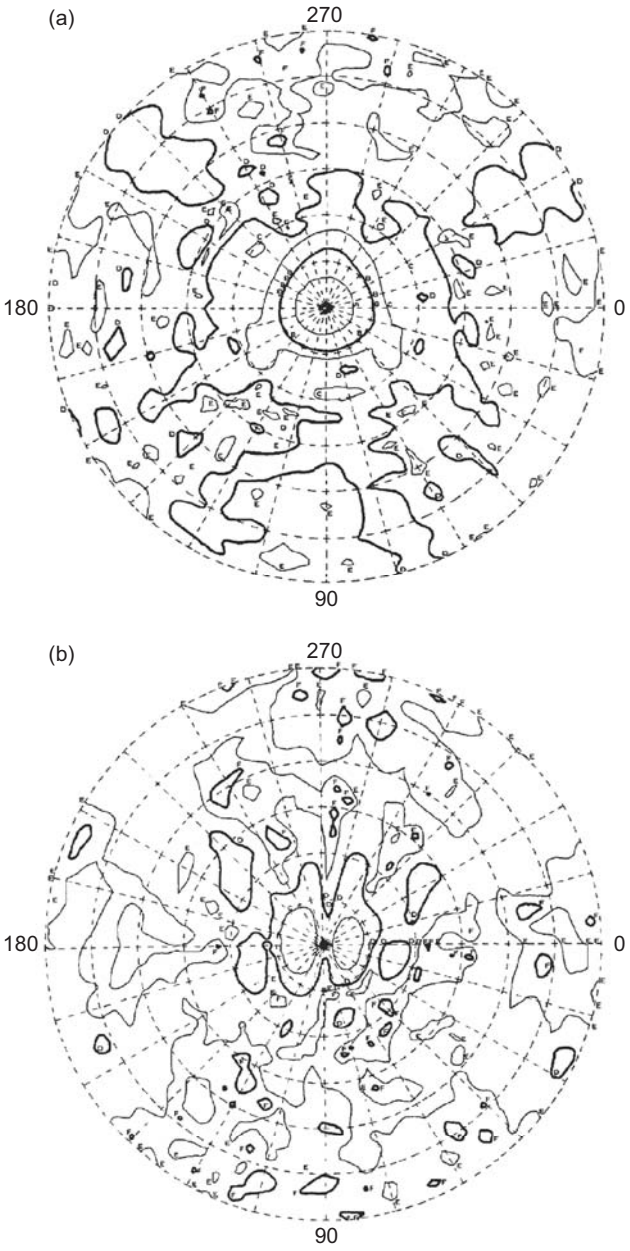

Fig. 7-3. Seasat SMMR antenna pattern contour plots at 6.6 GHz horizontal polarization, 0-deg scan position (the outer limit of the plots is at $|\theta|$ = 30 deg; contour lines are at decreasing intervals of 10 dB as follows: A = –5 dB, B = –15 dB, C = –25 dB, D = –35 dB, E = –45 dB, F = –55 dB): (a) co-polarized and (b) cross-polarized.

Table 7-3. Summary of Seasat SMMR antenna measurements.

Frequency (GHz)	Polarization	Half-Power Beamwidth (deg)	Beam Efficiency (percent)	Cross-Polarization Isolation (dB)	Dissipative Feed Loss (dB)
6.6	V	4.56	79.7	–21.5	0.55
	H	4.51	83.4	–19.9	0.55
10.69	V	2.93	83.8	–16.6	0.35
	H	2.91	86.2	–16.1	0.37
18	V	1.80	85.2	–21.2	0.50
	H	1.81	88.7	–20.1	0.52
21	V	1.50	84.2	–19.5	1.03
	H	1.49	85.8	–18.4	1.03
37	V	0.93	88.2	–17.9	0.7
	H	0.93	90.0	–17.4	0.7

H = horizontal; V = vertical

struts was a major factor in reducing the beam efficiency from the expected range (88–92 percent) to as low as 79 percent, for the 6.6-GHz V polarization. This in turn demanded high performance from the APC algorithm. In the final analysis, enough issues remained in the APC algorithm to reduce confidence in the accuracy of retrieved geophysical products. Hence, for subsequent antennas, there were significant efforts to reduce illumination of the struts or eliminate them altogether.

7.1.3 TOPEX/Poseidon Water Vapor Radiometer

The successful geophysical retrievals of the SMMR and (particularly) the radar altimeter on the Seasat mission led to proposals to use similar instruments on the Ocean Topography Explorer (TOPEX)/Poseidon mission, a joint U.S. and French effort to map ocean surface topography with precision approaching 1 cm.

Errors in the surface height measured by the altimeter result from orbit, attitude, and geoid uncertainties, from errors inherent in the radar measurement, and from inaccuracies in the time of flight of the radar signal, due to propagation effects. The TOPEX/Poseidon microwave radiometer (TMR) provides a correction to path delay due to tropospheric water vapor ranging from 5 to 50 cm, depending on temperature and humidity in the tropospheric portion of the path. After this correction (plus others due to dry air radiative transfer and ionospheric delay), the predicted accuracy of the radar altimeter was better than 1.2 cm. Experience with SMMR and the altimeter on Seasat showed unacceptably large errors due to the SMMR swath lying 42 deg ahead of the altimeter FOV at nadir; therefore the TMR configuration required co-

alignment of radiometer and altimeter boresights. The scanning capability of SMMR was also removed from the TMR [9]. The TMR reflector was a flight spare from the Nimbus-7 and Seasat SMMR programs.

The 6.6- and 10.69-GHz channels, used in SMMR for sea surface temperature and surface wind retrievals, were dropped from the TMR. Likewise, one polarization of each of the 18- and 37-GHz channels was discarded. Both polarizations were retained for the 21-GHz channel, deemed critical to the path delay retrieval, with one polarization redundant, to be activated only if the other failed. These changes also relaxed the requirements

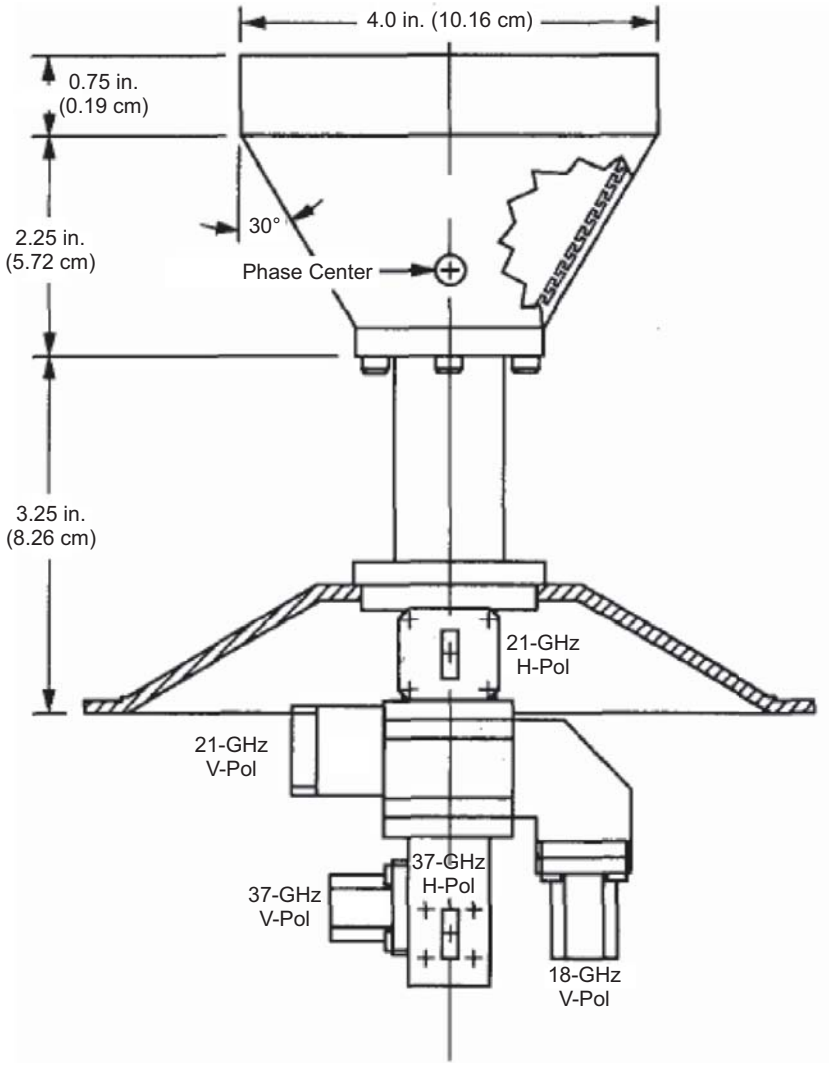

Fig. 7-4. TOPEX/Poseidon TMR multifrequency feed horn.

on the multifrequency feed horn (Fig. 7-4), for which the flare angle was reduced. Another beneficial result was to under-illuminate the reflector by 1 to 3 dB lower than SMMR, depending on frequency. This expands the HPBW by 5 percent but reduces spillover, and (with less illumination of the strut supports) it increases main beam efficiency by 2.4 percent, mitigating the need found in SMMR for extreme accuracy in the antenna pattern corrections.

Antenna patterns of all four channels of the TMR were measured on the JPL antenna range facility at a distance of 366 m, more than twice the far-field distance $2D^2/\lambda$. Patterns were measured in both polarizations over the full 4π solid angle. The effects of range asymmetry were seen in the low sidelobes between 130 and 180 deg from boresight, using the redundant pattern data obtained with the available positioner axes, and removed from the dataset used for processing of in-flight data [10]. Table 7-4 summarizes the measured performance of the TMR antenna and its lowest expected mechanical resonant frequency.

Figure 7-5 is a line drawing of the TOPEX/Poseidon spacecraft with the microwave radiometer viewed from behind its reflector. The mounting angle is for co-alignment of the radiometer and altimeter boresights. Not shown are the cold space calibration horns, which were pointed away from the Sun, to avoid radiometric contamination of the calibration noted in [6].

Radomes consisting of flat slabs of polystyrene (0.95 cm thick, with dielectric constants in the range 1.03–1.16) were also mounted in front of the multifrequency feed horn and sky horns, to reduce solar heating of these horns which results in antenna temperature fluctuations. The voltage standing wave ratio (VSWR) and insertion loss were determined radiometrically (using other ground-based water vapor radiometers) for inclusion in the antenna temperature calibration, and antenna patterns were made with radomes present. Ultraviolet

Table 7-4. TMR antenna specifications.

Parameter	Values			
Frequency (GHz)	18	H21	V21	37
Half-power beamwidth (±0.1 deg)	1.86	1.56	1.59	0.98
Solid-angle beam efficiency (percent)	91.1	89.3	87.4	90.5
Back-lobe artifact beam fraction	0.0018	0.0011	0.0017	0.0009
• Flight antenna beam fraction outside main beam	0.028	0.025	0.032	0.022
• Within Earth limb	0.005	0.003	0.003	0.004
Boresight co-alignment with altimeter (deg), (3σ)	0.4			
Minimum natural frequency (Hz)	>55			

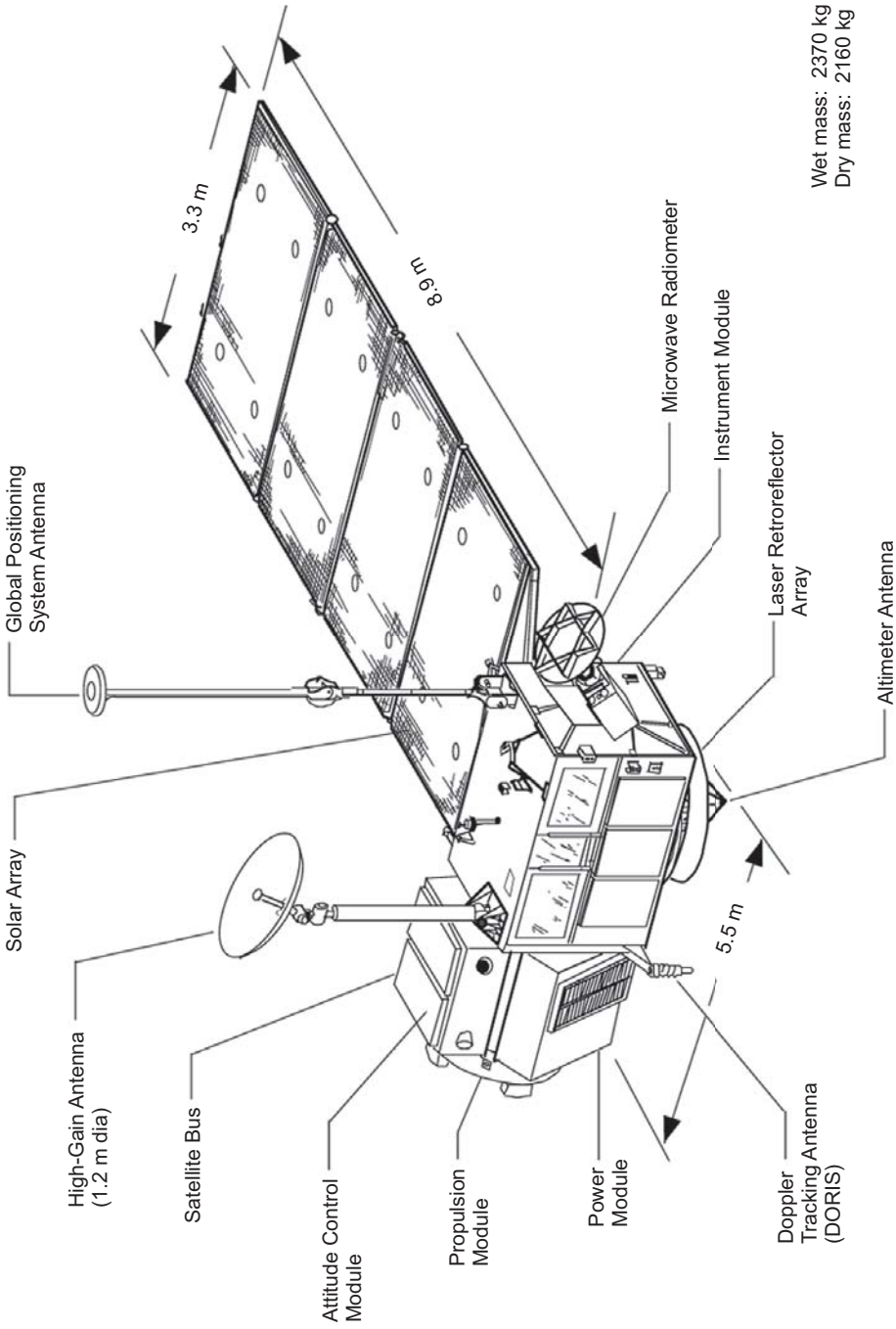

Fig. 7-5. TOPEX/Poseidon spacecraft.

exposure of the radomes, at several times the level expected in the orbital environment, resulted in some discoloration of the radome, but the darkening was self-limiting, and its ultimate effect on RF and thermo-optical performances was negligible.

Combining all known error sources from ground calibrations, the accuracy of the TMR data product was expected to be 0.57 K in antenna temperature, which when propagated through the antenna pattern-correction algorithm gives 0.77 K in brightness temperature, a significant improvement over SMMR.

TOPEX/Poseidon was launched on August 10, 1992; the TMR was activated and produced data 5 days later. Standard data sets in the final operational orbit began September 23 and have continued through the present, i.e., three times the planned prime mission lifetime of 3 years.

Engineering telemetry showed that the rate of change of antenna temperature during solar illumination of the feed and sky horns was below 0.001 deg C/s—again a significant improvement over 0.015 deg C/s experienced with SMMR and a validation of the feed redesign. The post-launch validation campaign revealed gain errors as large as 10 percent in the TMR water vapor retrieval, relative to ground truth obtained from upward-looking water vapor radiometer and radiosondes. This error was attributed partially to uncertainties in the 22-GHz water vapor absorption line strength, and partially to underestimates of the far sidelobe beam fractions of Table 7-4, which are applied in pattern correction [11]. These amendments to the ground calibration dataset were in some cases as large as a four-fold increase in the fraction of beam power missing the Earth. This reinforces the need for accurate pattern knowledge derived from both ground and in-orbit calibrations.

7.1.4 Jason Microwave Radiometer

The goal of the Jason-l mission is to further the understanding of global ocean dynamics by precise and accurate measurements of the ocean's topography, begun by the TOPEX/Poseidon mission. Jason-1 was launched in December 2001, and presently operates in tandem with TOPEX/Poseidon, which increases the data flow and allows cross checks between the two instrument platforms. As with TOPEX/Poseidon, the principal instrument carried by Jason-l is a radar altimeter, the accuracy of which is affected by the variable water content of the atmosphere, especially the troposphere. The objective of the Jason-l microwave radiometer (JMR) is passive measurement of the radiometric brightness temperature arising from water vapor and liquid water in the same FOV as the altimeter. These brightness temperatures, in turn, are converted to path-delay information required by the co-aligned altimeter for precise topography measurements. The JMR continuously measures the microwave radiation at 18.7, 23.8, and 34 GHz, and the data are used to

determine water-vapor and liquid-water content in the altimeter FOV. The JMR antenna system consists of:

1) A collecting aperture with the RF pointing axis aligned collinear with the pointing axis of the altimeter sensor.
2) A multifrequency feed assembly that illuminates the collecting aperture.
3) Multichannel microwave receivers coupled to the feed assembly.

Antenna requirements, given in Table 7-5 [12] are derived from orbital parameters for the Jason-l mission, viz.: (1) Altitude 1336 km, nominal (1000–1500 to be accommodated), (2) Inclination 66 deg.

The antenna/feed system, like that of SMMR and TMR, is an offset parabolic reflector illuminated by a single feed horn. The reflector surface consists of multiple layers of vapor-deposited aluminum and silicon dioxide. The feed horn is a multifrequency dual-polarized feed assembly that operates at both horizontal and vertical polarization, and it is designed to operate at the three center frequencies given above. Both the reflector and the feed are similar to the components flown as part of the TOPEX/Poseidon TMR.

Although TMR patterns had been measured in the far field on the JPL antenna range, JMR patterns were measured in the intermediate field (16 m «154 m= $2D^2/\lambda$) at a contractor facility. This indoor range enabled the patterns to be taken with a dynamic range of 63 dB, compared to 71 dB for TMR on the JPL range, and the beam fraction to be calculated to an accuracy of 0.25 percent vs. 0.43 percent on the JPL range. The intermediate range was operated as a spherical near-field range, in order to characterize the back lobes accurately. All performance requirements were met or exceeded on the flight model unit.

Figure 7-6 is a photograph of the JMR. Jason-1 was successfully launched on December 7, 2001, and its orbit was then adjusted to match that of TOPEX/Poseidon, with a 1-minute time separation. Both instruments then began a rigorous comparison and correlation of the two altimetry results from near-simultaneous measurements from the same altitude of the same sea surface locations. Initial results showed that the Jason altimeter and radiometer met all mission requirements. In August–September 2002 the orbit of

Table 7-5. JMR antenna requirements.

Parameter	Values			
Frequency (GHz ±25 MHz)	18.700	23.800 (H)	23.800 (V)	34.000
Pre-detection ± dB bandwidth (MHz)	200	400	400	700
Half-power beamwidth (±0.1 deg)	1.8	1.5	1.5	0.9
Solid-angle beam efficiency	>90 percent			
Boresight co-alignment with altimeter (3σ)	0.4 deg			
Minimum natural frequency	>55 Hz			

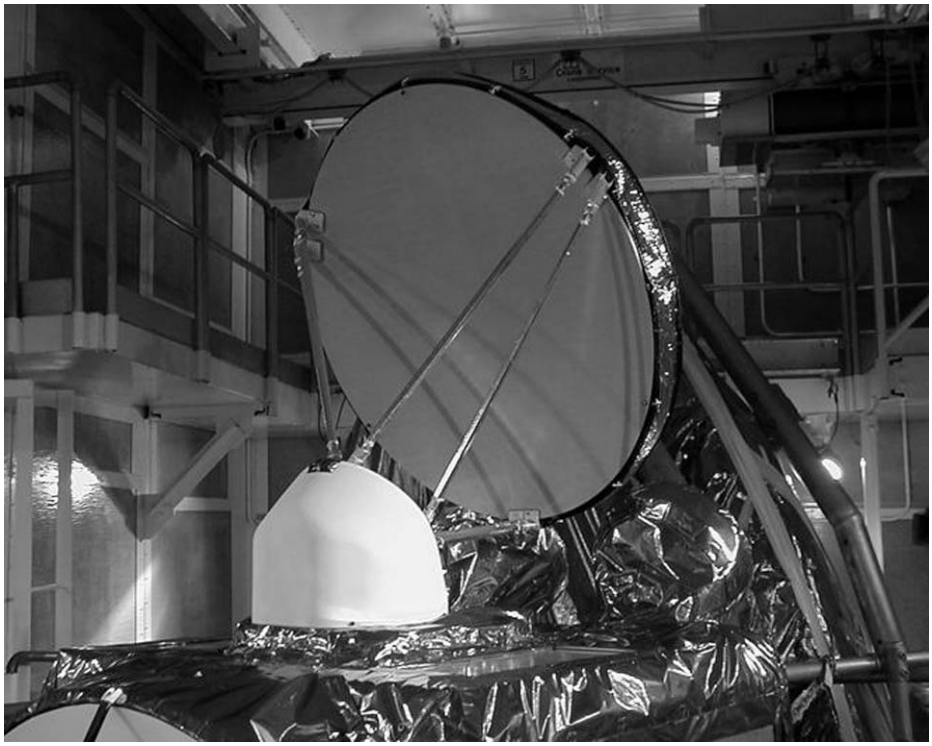

Fig. 7-6. JASON microwave radiometer (JMR) aboard JASON-1 spacecraft.

TOPEX/Poseidon was adjusted to have an orbital phase 180 deg from JASON, so that the two satellites increased global data coverage twofold.

7.1.5 Microwave Instrument for the Rosetta Orbiter

The microwave instrument for the Rosetta orbiter (MIRO) is a radiometer with millimeter and sub-millimeter receivers that will observe comet dynamics and composition; its mission also includes three planetary fly-bys and two asteroid flybys. After rendezvous with the comet at 4 AU and separation from the lander portion of the spacecraft, the orbiter will follow the comet through perihelion.

The sub-millimeter radiometer operates between 545 and 580 GHz, monitoring inner coma development by spectroscopy of several gasses at the comet, and measuring low levels of gas in the asteroid environment. A millimeter-wave radiometer operating at 190 GHz provides continuum measurements for temperature sensing and surface processes (to depths of a few centimeters at the comet nucleus or asteroid surface) [13].

7.1.5.1 Antenna Requirements. The performance requirements of the MIRO antenna and optics are made stringent by exposure to the Sun and to the cometary environment, and by the temperature extremes over which the radiometer must operate: between 100 K (comet rendezvous) and 300 K (perihelion). Further requirements for a robust mechanical design are imposed by the Ariane-5 launch vehicle, with a minimum instrument eigen-frequency of 150 Hz, and by the 15-year lifetime between launch and comet rendezvous. Table 7-6 gives the MIRO antenna requirements [14].

The antenna is completely exposed to the space environment, while the multiplexer optics and receivers are within the Rosetta spacecraft. Due to the resulting constraints on the antenna size, the requirement for low sidelobes, and a desire for main beam efficiency exceeding 90 percent, an offset Cassegrain reflector system was chosen for the design. The advantages of an unblocked optical path were shown to outweigh the penalty of an asymmetric support structure in the thermal-mechanical deformation phase of the design.

7.1.5.2 Selected Design. Both the support structure and the reflectors were made all of aluminum for lightness and to achieve a homologous deformation giving nearly constant antenna performance over temperature. For the same reason, a beamwaist was placed at the first internal mirror, close to the fixed point of the thermal deformation, keeping the phase center near the telescope focus for all environments. Supports were designed to be as symmetric as possible to minimize lateral misalignments due to thermal deformation.

Figure 7-7 is a photograph of the MIRO telescope assembly, showing primary and secondary reflectors and the hole through which the beam is focused onto the turning mirror. Figure 7-8 shows the schematic diagram of the optical system. The primary mirror is a paraboloid 300 mm in diameter, the

Table 7-6. MIRO antenna requirements.

Requirement	190 GHz	564 GHz
Loss contribution (dB)		
Spillover	0.1	0.1
Surface rms	0.1	0.3
Illumination	1.6	1.5
Total loss	1.8	1.9
Peak gain (dB)	53.7	63.0
HPBW (deg)	0.4	0.15
Tolerance limits		
Sidelobe level (dB)	–30	–30
Pointing (deg)	0.04	0.015

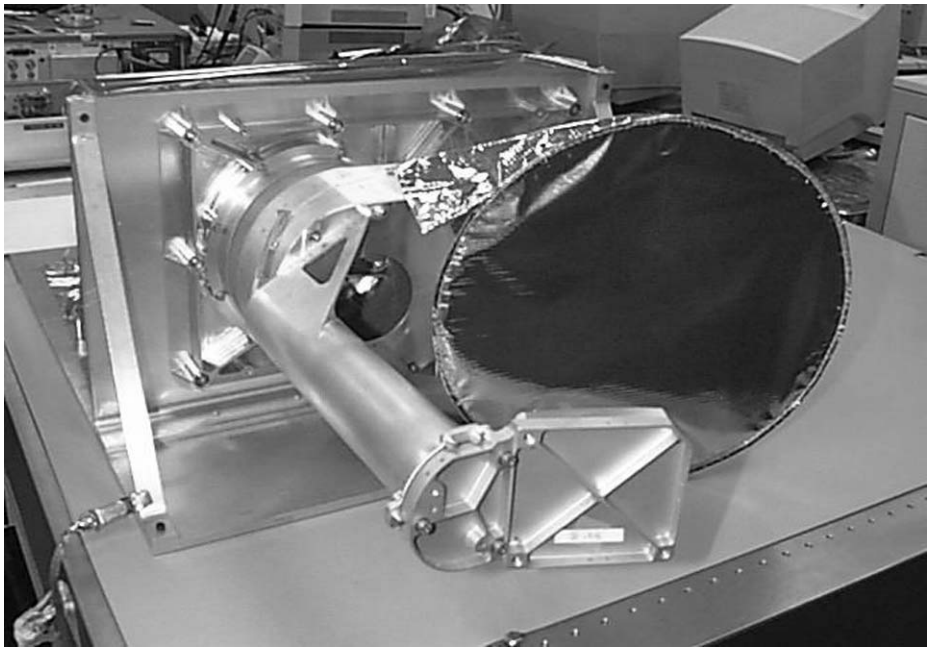

Fig. 7-7. Microwave instrument for the Rosetta Orbiter (MIRO) telescope.

secondary mirror is a hyperboloid 90 mm in diameter, and the turning mirror (at the beamwaist) is planar. This mirror is also the only moving mechanical part of the optical system; it switches radiometer views to the telescope or to either of two black-body calibration loads, which overfill the feed beams. One of these targets is kept near ambient temperature, while the other is thermally connected to cold space; their temperature difference gives two radiances, which are used for periodic radiometric calibration.

As is customary at these frequencies, the multiplexing between millimeter and sub-millimeter receivers is performed quasi-optically, using a wire-grid polarizer, to avoid ohmic losses of waveguide. Curved mirrors are used to match the large *f*/D beam, produced by the Cassegrain design, to corrugated feed horns attached to the mixer assemblies. Thermal analysis showed predicted temperature excursions of the optical bench to be small enough that alignment shifts would be negligible.

7.1.5.3 Performance Estimates. The antenna reflector surface figure was 11 μm rms, which was expected to contribute much less to sidelobe levels than larger-scale effects, such as feed pattern imperfections and distortions under vibration or thermal deformation. An extensive suite of mechanical, thermal, and RF design tools was developed to predict these changes in antenna patterns. Typically, undistorted sidelobe levels of –37.8 and –38.3 dBr respectively, for

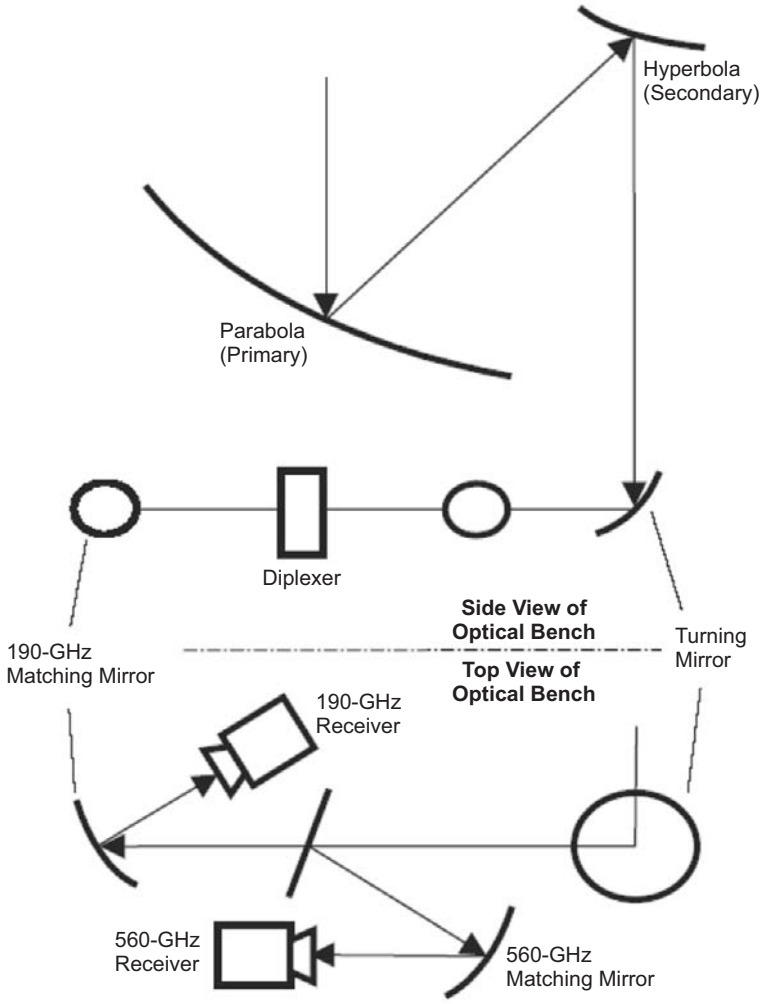

Fig. 7-8. Schematic diagram of the MIRO optical system, including side and top views of the optical bench.

the millimeter and sub-millimeter beams, would be distorted in the worst environments to just the –30 dBr level of the requirements.

Due to water vapor absorption near 550 GHz, the atmospheric path loss would be too large and too variable over even the modest $2D^2/\lambda = 360$ m required for far-field patterns. Therefore, a near-field range was obtained, and phase-locking electronics were developed at the receiver frequencies for measuring MIRO antenna patterns. Preliminary results of these patterns show HPBWs of 0.39 and 0.125, which meet the requirements of Table 7-6. Sidelobe levels range between –28 and –34 dB below the main beam, which nearly

meets the requirement. Main beam efficiency is about 92 percent, a typical value for tapered dual-offset reflector designs.

7.1.5.4 Conclusions. When the analysis of pattern measurement is completed, MIRO antenna requirements are expected to be met, although the elevation of sidelobe levels due to thermal deformation may remain an issue that cannot be resolved from pre-flight calibration.

Antenna performance under extreme environments is still verified by analysis, rather than by measurement during environmental qualification tests. However, recent advances in optomechanical metrology promise to give much better insight into the alignment of antenna components during test. This, plus the maturity of sophisticated RF scattering models over the past few decades, lets the designer expect to be able to prove much stronger statements about radiometer antenna performance in the extreme environments of deep-space missions.

The MIRO instrument was integrated with The European Space Agency's (ESA's) ROSETTA spacecraft and launched March 2, 2004, on board an Ariane-5 rocket from Europe's spaceport in Kourou, French Guiana. Rendezvous with the comet 67P/Churyumov-Gerasimenko is expected in November 2014.

7.2 Microwave Limb Sounders (MLS)

Richard E. Cofield

Microwave limb sounding is the measurement of thermal emission spectra at millimeter and sub-millimeter wavelengths by scanning the field of view (FOV) of a heterodyne radiometer instrument through a planetary atmospheric limb from above. Analysis of the measured spectra determine atmospheric profiles of temperature, pressure, wind, magnetic field, and molecular abundances, particularly of trace species with thermal emissions that can only be detected using the long path lengths involved. A strong motivation to measure such species comes from the need to understand the chemistry of ozone (O_3) destruction in Earth s stratosphere, and climate change in the upper troposphere. Thermal emission, requiring no external sources, can be observed continuously, and at these frequencies even in the presence of clouds and rain. Thus, instruments can be developed for orbiting satellites for long-term global coverage with reliable calibration [15].

For atmospheric limb sounding in optically thin spectral regions, most of the signal originates from thermal emission by that portion of the ray path which is normal to a radius vector from Earth center, i.e. tangent to a surface of constant height (or pressure). Thus, the two important heights are platform or observation height and tangent height, denoted h_0 and h_T, respectively.

Several airborne and balloon implementations of microwave limb sounders validated the technique before the first satellite implementation. They continue to provide invaluable tests as new technology evolves, plus opportunities for ground truth validation.

7.2.1 UARS MLS

The microwave limb sounder (MLS) instrument flown on the Upper Atmospheric Research Satellite (UARS) was the first spaceborne application of microwave limb sounding. MLS was one of 10 UARS instruments in a National Aeronautics and Space Administration (NASA) mission dedicated to the comprehensive and integrated study of the Earth's upper atmosphere. Table 7-7 [16] gives the measurement objectives, radiometer bands, and local oscillator (LO) frequencies of the UARS MLS. Chlorine monoxide (ClO) is the rate-limiting molecule in chlorine destruction of O_3, and MLS measurements of its abundance on a global scale indicated the rate at which chlorine destroys ozone. Simultaneous measurements of O_3 and water (H_2O) provided additional information on stratospheric ozone chemistry. Pressure measurements from molecular oxygen (O_2) provided the vertical coordinate for atmospheric profiles.

The MLS instrument is described in [17]. Figure 7-9 shows the MLS signal flow block diagram. Its antenna received radiation from the atmospheric limb and was mechanically scanned in the vertical. A switching mirror accepted radiation either from the antenna or, for calibration, from an internal target or a space view. An optical multiplexer then separated signals into the three heterodyne radiometers. Requirements for the antenna and optics design were derived directly from the functional requirements on the instrument FOV. In

Table 7-7. UARS MLS radiometer bands and mission objectives.

Radiometer	LO Frequency (GHz)	Band	Intermediate Frequency Range (MHz)	Primary (Secondary) Parameter	Measurement h_T Range (km)
1	63.283	B1	90–540	Pressure, temperature	30–60
2	203.267	B2	830–1340	ClO	15–45
		B3	1053–1563	(H_2O_2)[a]	
		B4	2610–3120	O_3	15–50[b]
3	184.778	B5	1213–1723	H_2O	15–85
		B6	145–655	O_3	21–80[b]

[a] H_2O_2 = hydrogen peroxide; was a secondary mission goal
[b] Tangent height range refined in post-launch science data analysis [16]

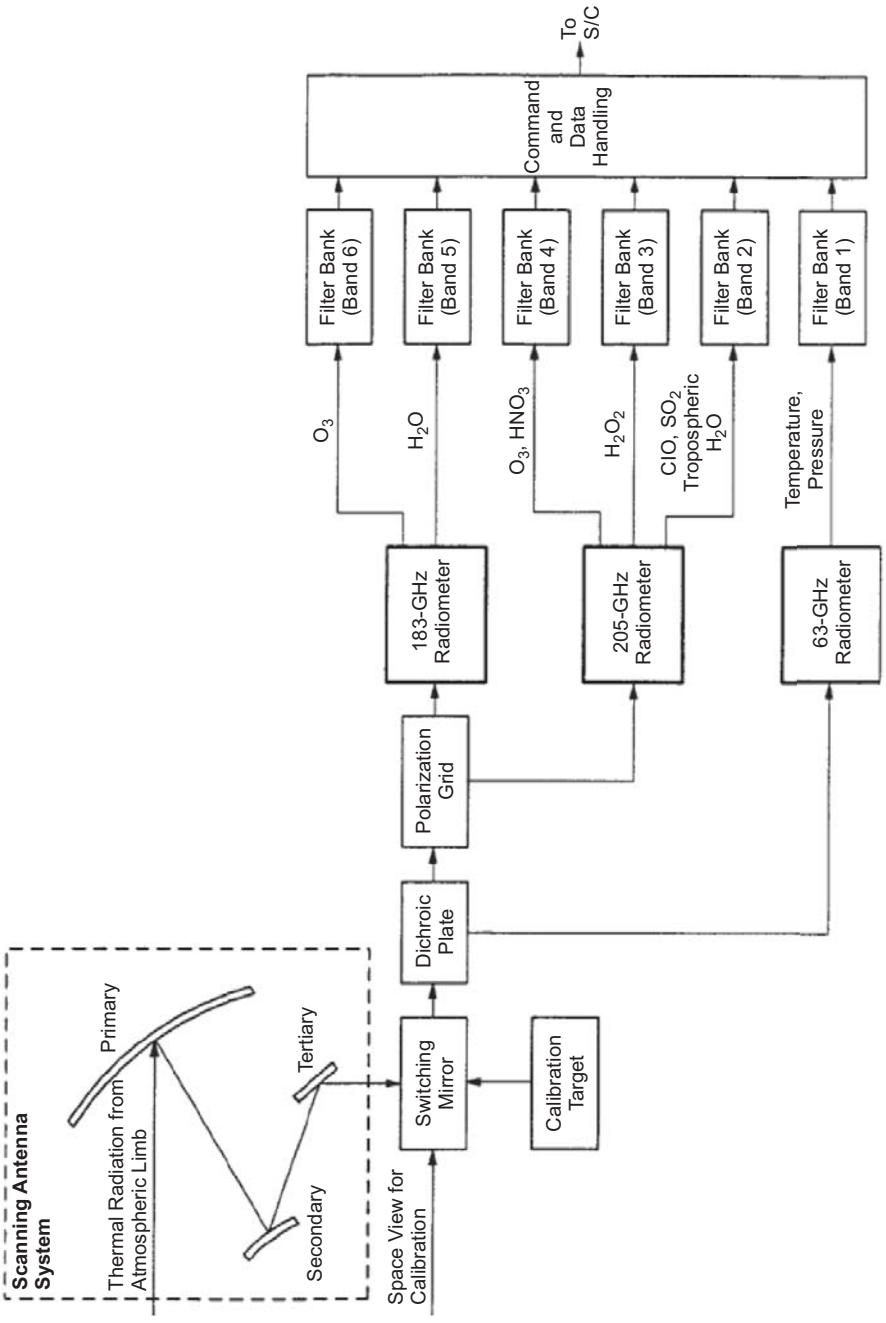

Fig. 7-9. Signal flow block diagram of the Upper Atmosphere Research Satellite (UARS) microwave limb sounder (MLS) instrument.

addition to customary requirements on HPBW, boresight direction, and beam efficiency, the algorithms for atmospheric profile retrievals levied requirements for detailed knowledge of the actual pattern shape. This was supplied by combining analysis with pattern measurements, as functions of frequency and scan angle in both polarizations and overall solid angles.

7.2.1.1 Antenna Requirements. The MLS FOV is defined as the response of the MLS as a function of direction to power received from an isotropic radiation field. This response is normalized to a maximum value of unity; hence, FOV corresponds to antenna directivity, with some qualifications for polarization in the limb-sounding application. FOV half-power beam width (HPBW) is defined as the angle between the half-power points of the FOV function. Requirements levied on the MLS HPBW are given in Table 7-8 and are converted from footprint kilometers to beam angles using the known viewing geometry. The HPBW must be known and stable to within 5 percent of its value measured during FOV calibration.

Table 7-8. UARS MLS requirements.

Radiometer Band	Vertical HPBW		Horizontal HPBW	
	km	deg	km	deg
B1 (63 GHz)	≤12	≤0.25	≤30	≤0.64
B2–4 (205 GHz)	≤3.5	≤0.075	≤10	≤0.21
B5–6 (183 GHz)	≤4.0	≤0.083	≤10	≤0.21

Boresight Pointing Accuracy	Time Scale	Vertical		Horizontal	
		km	arcsec	km	arcsec
Placement	—	3.0	225	30	2250
Knowledge	Mission	3.0	225	30	2250
Stability	65-s scan	0.3	23	3	225
Jitter	1.8-s dwell	0.3	23	3	225

Vertical Scan	
Step size	0.05 ±0.01 deg
Encoder resolution	≤0.001 deg
Dwell time between steps	1.8 ±0.1 s
Time for movement between adjacent steps	<0.3 s
h_T of scan range for atmospheric measurements	0–120 km
h_T of FOV direction for space view	>200 km
Scan axis/UARS velocity vector collinearity	±0.5 deg

FOV boresight is defined as the direction midway between half-power points in the vertical and horizontal planes. Requirements levied on the MLS FOV boresight coincidence ensured that different radiometers observe the same region of the atmosphere to within acceptable limits. The FOV boresights of all bands coincided to within 0.2 of the largest HPBW, and the coincidence was known and stable to within 4 arc seconds in the vertical plane and 20 arc seconds in the horizontal plane.

Beam efficiency is defined as that fraction of power from an isotropic source, which is collected within a specified angular range centered at the antenna boresight. For each MLS band identified in Table 7-7, the beam efficiency was required to be >0.5 within the HPBW and >0.9 within 2.5 HPBW. Beam efficiencies were required to be known and constant throughout the UARS mission to within 1 percent.

Table 7-8 also gives MLS scan requirements and tolerance requirements on FOV placement, knowledge, stability, and jitter. Finally, the lowest mechanical resonance frequency (driven for this instrument by the stiffness of the antenna support cradle) was >35 Hz.

The MLS FOV had to be determined to allow calculation, with the required accuracy, of received signal for a specified atmospheric radiation field. This determination was called FOV calibration in the MLS project, and it consisted of a mixture of antenna pattern measurements with analytical models, both in the solid-angle regions where measurement was infeasible, and of the thermal deformation of the antenna in orbit. As in the formulation for the SMMR [8], we write the antenna temperature

$$T_A = \frac{1}{4\pi} \int_{\text{all directions}} G(\Omega)\, T_B(\Omega)\, d\Omega$$

where $G(\Omega)$ describes the FOV in direction $\Omega(\theta,\phi)$ and is normalized so that $\int G(\Omega) d\Omega = 4\pi$; T_B is a brightness temperature kernel from a set of modeled atmospheric profiles, which vary only in the limb vertical direction for calculating the accuracy and resolution needed for $G(\Omega)$. The requirement is that $G(\Omega)$ be determined with sufficient accuracy and resolution to introduce less than 0.5-percent error in the calculation of T_A from the preceding equation, for FOV boresight directions encountered during the scan in orbit.

Despite this formulation of requirements, analysis of MLS data did not follow the APC method of SMMR, but rather combined FOV calibration data with spectral calibration data (filter shapes and sideband responses) in a forward model which related instrument radiances directly to geophysical parameters[15,17]. The resulting sensitivities were then used with *a priori* climatology profiles to retrieve actual profiles, with a nonlinear retrieval algorithm [16]. This approach has also been used in the successors to the UARS MLS.

7.2.1.2 Trade-off Studies. A reflector antenna system was the only candidate considered capable of producing the electrically large (D ~1000λ) aperture required. Reflectors were offset to avoid blockage, and a dual reflector system was used to achieve both a compact antenna and the moderately large f/D required for quasi-optical multiplexing the various bands and injecting LOs. Since the scan range (including margin and space view) was ~120 × HPBW, the beam scan deviation had to be minimized by scanning in the long f/D portion of the beam, i.e., between the secondary reflector and the multiplexer.

7.2.1.3 Selected Design. The antenna system was a dual-offset Cassegrain with a 1.6 × 0.8 m elliptical aperture. The elliptical aperture saved space in the instrument envelope but constrained the location and curvatures of subsequent mirrors that coupled antenna beams into the receiver feed horns. The primary reflector was an offset paraboloidal section of a 1-m focal length parent surface, with the aperture center offset 0.7 m from the parent axis. With the hyperboloidal secondary reflector, the antenna effective focal length was 5.9 m. A flat tertiary reflector diverted the limb radiation signal along an axis coincident with the mechanical scan axis, into a box housing the optical multiplexer and front ends of the three radiometers. The power illumination level at the primary aperture edge, when projected from the design feed pattern, was 15 dB below the level at aperture center, and it defined the limiting aperture size. The secondary and all subsequent optical elements were sized to truncate at –20 dB.

Since emission from the atmospheric limb is unpolarized (except for Zeeman splitting in the 63-GHz channels), the only degradation due to cross polarization appears as broadening of the net pattern (power sum of co- and cross-polarized patterns), i.e., degraded beam efficiency. Therefore, the angle between hyperboloid and paraboloid axes was relaxed from the Mizuguch value, which in the geometrical optics approximation cancels aperture cross-polarized fields. The actual angle permitted structural support for the secondary and tertiary reflectors with the scan bearings, in a reasonably compact envelope.

Table 7-9 gives the physical characteristics of the three antenna reflectors, and Fig. 7-10 shows the MLS instrument in flight configuration. All reflectors and structure were made of aluminum to ensure homologous deformations, so that the antenna stayed in focus over a wide range of temperatures.

The tolerance requirement for reflector surfaces was met with a net value of 28 μm (root sum square [rss] over three surfaces). Thus, upper bounds on scattering loss were 0.043 for the 183-GHz band and 0.054 for the 205-GHz band. Estimated losses were reduced further by excluding surface errors of large enough correlation length to appear in the measured antenna patterns. The signal-to-noise ratio (SNR) achieved during antenna tests imposed limits on this reduction. SNR was 55 dB for 63 GHz, 42 dB for 183 GHz, and 50 dB for

Table 7-9. UARS MLS physical antenna characteristics.

Parameter	Primary	Secondary	Tertiary
Reflector aperture (m)	1.6 × 0.8	0.45 × 0.24	0.24 × 0.20
Effective focal length (m)	5.9		N/A
Surface accuracy (μm)	23	13	8
Edge illumination (dB)	–15	–20	<–15

205 GHz patterns, resulting in estimated scattering losses of 0.001, 0.012, and 0.008, respectively [18].

Performance of the antenna under orbital heat loads was predicted by feeding temperature fields from a thermal model into a NASA structural analysis computer program (NASTRAN) structural model, which calculated deformations. In turn, these were input to an optics model. Expected changes in pointing direction and aperture phase curvature were well within allocations for all anticipated conditions. Bead-blasting in the final stages of manufacture gave the reflectors their required diffusivity. Effects of this surface treatment were a shift in focal length, corrected with shims during antenna assembly, and a small decrease in antenna reflectivity, to >0.995 per surface, measured radiometrically on witness samples using an engineering model [19].

A calibration switching mirror in the radiometer module diverted the views of radiometers from limb to cold space and ambient temperature targets, like those described above for previous instruments. Its output was separated by a quasi-optical multiplexer into the three radiometers. The multiplexer used wire grid polarizers and dichroic plates for low signal path losses, ranging from 1.0 to 1.5 dB, and included toroidal mirrors to match the elliptical astigmatic beams to the circular beams of radiometer feed horns. Horns were of a dual-mode conical design modified [20] from the Potter horn design for easy fabrication at high frequencies. LO injection for the 183- and 205-GHz frequencies was accomplished using folded ring-resonant Fabry-Perot diplexers. Gaussian beam optics were used throughout the design.

Radiometer feed patterns were measured at the subassembly level to verify proper antenna illumination, alignment sensitivity, and radiometer port spillover levels. These were repeated using the radiometer box assembly for the engineering model. Secondary patterns were characterized on far-field ranges at 3 and 1 km, at 10 scan angles, and at five frequencies within each band. Boresight directions at 63 and 205 GHz were measured to 15 arcsec relative to an optical alignment cube using a theodolite in conjunction with the RF patterns. A more stringent 2-arcsec knowledge of relative pointing between all radiometers was measured with near-simultaneous patterns using two transmitters at known separations.

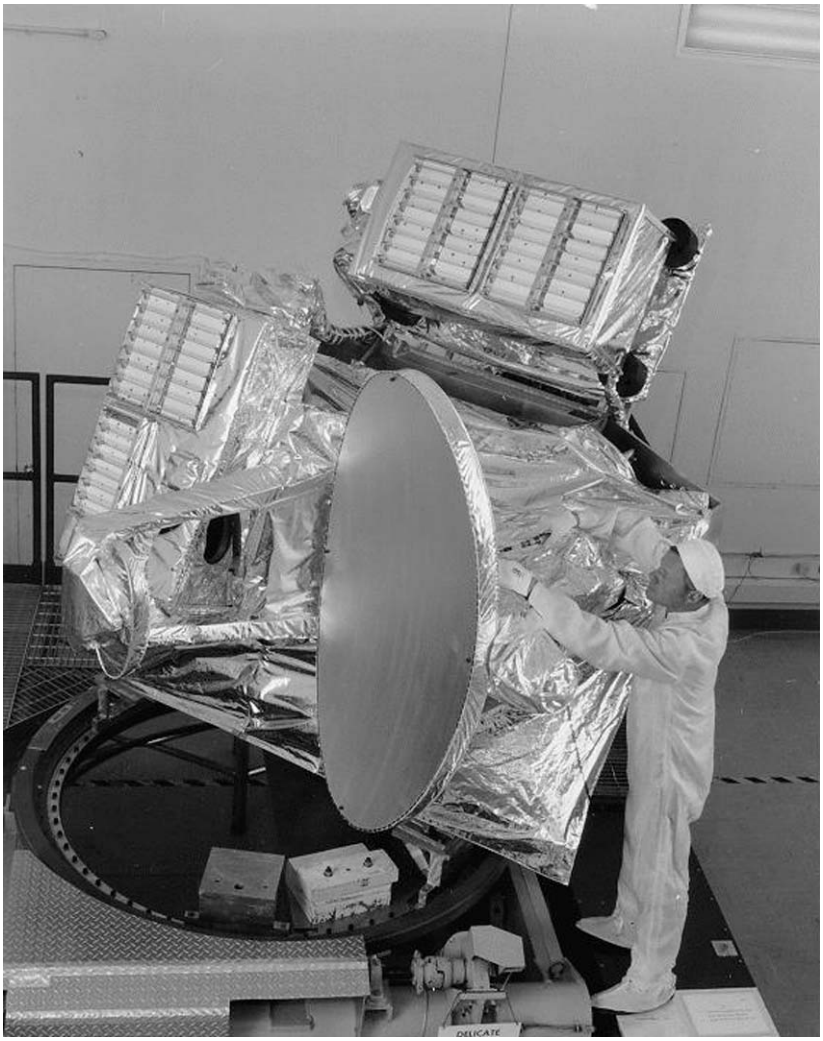

Fig. 7-10. UARS MLS in flight configuration.

Figure 7-11 shows a vertical plane cut of the UARS MLS 205 GHz antenna pattern. Table 7-10 summarizes the UARS MLS antenna performance. Beamwidths and beam efficiencies met the requirements of Table 7-8, as did boresight directions, and the FOV calibration data set sufficed to meet the most stringent mission requirement, measurement of O_3 to an accuracy of 1–3 percent [17].

UARS was launched September 12, 1991 from the space shuttle Discovery into a 600-km altitude, 57-deg inclination orbit. Useful spectra were obtained within days after activating the MLS. Ground calibration and instrument

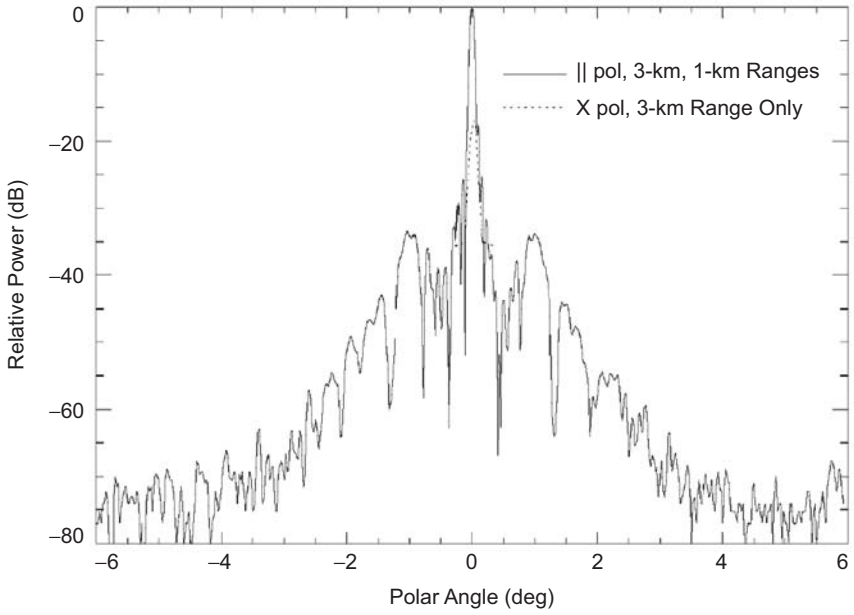

Fig. 7-11. 205-GHz limb vertical antenna pattern of UARS MLS.

Table 7-10. UARS MLS antenna performance.

Parameter	63 GHz (B1)	183 GHz (B5–6)	205 GHz (B2–4)
Vertical HPBW (deg)	0.206	0.077	0.064
1 σ uncertainty	0.002	0.001	0.001
Horisontal HPBW (deg)	0.43	0.152	0.145
1 σ uncertainty	0.008	0.002	0.003
Beam efficiency (1 σ = 0.01)	0.91	0.91	0.9
Polarization (angle from vertical of E projected from feed, at 30-km pointing) (deg)	114	1	91
Peak cross-polarization (dB)	–30	–20	–19
FOV direction knowledge elevation (deg)			
Absolute, B1 to alignment reference	0.0036	N/A	N/A
Relative to B1	N/A	0.0021	0.0016
Ohmic efficiency	0.992	0.992	0.989
Wide-angle efficiency (spillover, scattering, edge diffraction)	0.931	0.977	0.976

operations were of such high quality that several additional products were added to the UARS MLS dataset, including geopotential height, nitric acid (HNO_3), and sulfur dioxide (SO_2) during periods of significant enhancement

(such as following the eruption of Mount Pinatubo), upper tropospheric humidity, and acetonitrile (CH_3CN).

Two discrepancies between pre-launch FOV calibration and in-orbit data were found: An error in absolute pointing of 0.12 deg was attributed to uncertainty in the chain of transformations between alignment transformations from the MLS boresight to UARS reference, and it was corrected in the first few weeks of operation. The second discrepancy was a 15-percent difference in O_3 profiles retrieved from the 183-GHz and 205-GHz radiometers. This was reduced to <5 percent, in part by retrieving the relative pointing of all radiometers using the Moon as a calibration source in periods in which it drifted within range of the UARS MLS scan. The maximum resulting correction to pre-launch pointing was 0.011 deg [21]. Other investigations (using radiances from extremely high altitudes and special roll maneuvers of UARS) confirmed the low sidelobe and spillover levels in the pre-launch calibration dataset.

The UARS mission life was 18 months, set by the cryogen lifetime of the cryogenic limb array etalon spectrometer (CLAES). The MLS design lifetime was 36 months. Its 183-GHz radiometer failed after 19 months of successful operation; the cause was probably slow fracture of a solder joint between filter and a diplexer within the mixer. The MLS scan began to degrade after 3.5 years operation, due to build-up of wear products in the actuator mechanism. Following loss of the solar array drive in 1995 and aging of spacecraft battery systems, the MLS 63-GHz radiometer was switched off in 1997 to conserve power. Pressure profiles were obtained instead from linewidths in the 205-GHz radiometer. Following the most recent span of continuous operation in February 2000, MLS was put into survival mode, making no measurements but ready to be re-activated to obtain overlapping measurements with the Earth Observing System (EOS) MLS, which was launched in July 2004. However, it was never reactivated, and the UARS was scheduled for total deactivation in January of 2006.

7.3 Earth Observing System (EOS) MLS

Richard E. Cofield

A microwave limb sounder on the Aura satellite, the third in a series of satellites of NASA's Earth Observation System (EOS), continues the program of microwave limb sounding from space begun with UARS. Advances in receiver technology and reliability permit us to extend the EOS MLS observations up to 640 GHz, with fractional bandwidths increasing to almost ±10 percent to cover the many rotational molecular lines at these frequencies. The UARS MLS data quality allowed retrieval of profiles to be extended from the stratosphere down to the upper troposphere. Constituents measured by EOS MLS include pressure, temperature, geopotential height, cirrus ice, H_2O, O_3,

carbon monoxide (CO), hydrogen cyanide (HCN), nitrous oxide (N_2O), nitric acid (HNO_3), hydrochloric acid (HCl), ClO, bromine monoxide (BrO), and volcanic sulfur dioxide (SO_2). A measurement of the hydroxyl (OH) radical at 2.5 terahertz (THz) gives insight into hydrogen cycles in stratospheric chemistry.

As with the UARS MLS, the lowest target frequency comes from the vertical coordinate for profiles being pressure, obtained by EOS MLS from the 118-GHz O_2 line. Recent refinements in retrievals show this parameter can be obtained even more accurately from broadening of an isotopic O_2 line at 234 GHz.

UARS yawed 180 deg approximately every month, to keep sensors and their FOVs away from the Sun. To avoid the consequent gaps in global coverage, a polar Sun-synchronous orbit was chosen for the EOS satellites, with different orbital phases. EOS MLS scans in the orbital plane, for better coverage of the poles and with a preferred direction and period of scan. This lets orbital motion compensate for the along-track displacement of tangent points with scan angle, so that each profile is measured over one point on the Earth.

7.3.1 Antenna Requirements

Like the functional requirements of the UARS MLS, the science requirements for the EOS MLS were written explicitly to partition the instrument requirements into radiometric, spectral, and FOV requirements [22]. The latter, defined as requirements on the response to the instrument as a function of angle, were taken almost verbatim as antenna requirements. The following summary of EOS MLS antenna requirements highlights differences from the UARS MLS requirements described above.

Beamwidth requirements for EOS MLS are in Table 7-11. The EOS MLS has a single beam efficiency requirement: >0.95 within an angular range of 2.5 times the HPBW. FOV boresight is defined as the direction given by the peak

Table 7-11. EOS MLS science FOV requirements.

Radiometer Frequency	Footprint Width at 20-km Tangent Height			
	In Vertical Plane		In Horizontal Plane	
	km	deg	km	deg
118 GHz	6.5	0.123	15	0.285
190 GHz	4.5	0.085	10	0.190
240 GHz	3.5	0.066	10	0.190
640 GHz	1.5	0.028	10	0.190
2.5 THz	2.5	0.047	10	0.190

value of the Gaussian function that best fits the antenna response down to the 10-dB power points. FOV boresights of the 190-, 240-, and 640-GHz radiometers shall coincide with the 118-GHz FOV boresight to within one-fifth of the 118-GHz beamwidth. Engineering considerations make it desirable for the 2.5-THz radiometer to have separate optics, which is acceptable provided:

1) The 2.5-THz FOV boresight relative to the 118-GHz FOV boresight shall be known to within one fifth of the 118-GHz beamwidth,
2) The scan plane of the 2.5-THz boresight shall be within 10 km of that of the 118-GHz boresight at the atmospheric limb tangent point, over the tangent height range of 10 to 60 km.
3) The THz and GHz scans shall be synchronized.

The FOV scan plane shall be within 1 deg of the orbit plane. A continuous (i.e., non-stepped) scan, which emphasizes the lower stratosphere and upper troposphere and is synchronized to the orbit period, shall be used for routine atmospheric observations. The nominal scan pattern shall cover tangent heights of 2.5 to 62.5 km for the GHz radiometers and 15 to 62.5 km with 120-km space view for the THz radiometer, with more time spent at lower heights. The nominal scan, including retrace and calibration, shall have a period (24.7 s) that is 1/240 of the orbit period, and at least 75 percent of the time during this period shall be used for atmospheric measurements. The range of scan capability shall extend at least 4 deg to either side of that used for routine atmospheric observations. This provides for occasional scans outside the primary regions of interest, both for calibration purposes and for measurements over extended height ranges.

Tolerance in placement and knowledge of the tangent height of the FOV boresights, after in-orbit adjustments and accounting for Earth oblateness, is ±0.5 km at the start of each limb scan, degrading to ±1 km at the end of the limb scan.

The change in elevation of the FOV boresights with respect to nadir during each limb scan shall be known to an accuracy of 2 arcsecond (3σ), and the rate of change is known to an accuracy of 1 arcsecond per second (3σ), at time scales between 0.17 and 25 s. Jitter in the FOV boresights at time scales shorter than 0.17 s shall not exceed 2 arcsec (3σ).

The spectral and FOV responses of the instrument shall be characterized sufficiently that their separate uncertainties do not introduce uncertainties in the MLS forward model calculations of the atmospheric/Earth radiances of more than (at the 90 percent confidence level):

1) 3 K in the absolute value of the atmospheric/Earth radiances measured through each spectral channel, and
2) 1 percent (or $\Delta I_{min}/3$) in the spectrally-varying component of the atmospheric/Earth radiances measured from one channel or filter to another

throughout a given radiometer. $\Delta I_{min}/3$ is a channel-dependent allowable noise expressed in K and given in [22, Table 3.2-2].

7.3.2 Trade-off Studies

Since the EOS MLS has science requirements so similar to those for the UARS MLS, it was decided to use the same offset Cassegrain antenna system prescription for the newer instrument. The surface figure and roughness requirements were tightened to accommodate the higher frequency radiometers (240 and 640 GHz), and for EOS under-illumination was more extreme (nominal Gaussian beam truncations of –30 dB at the primary reflector and –40 dB elsewhere, versus –15 and –20 dB in the UARS MLS). This was to alleviate concerns with frequency-dependent spillovers within the optical system that could have contaminated the radiometric calibration of UARS [19]; such spillovers would be worse with the wider bandwidths of EOS MLS. In the polar orbit, solar illumination of the EOS MLS antenna, though having small seasonal variations, changes enough in each orbit to make the materials of UARS MLS infeasible (the all aluminum antenna would undergo a 25-percent change in HPBW over 1 orbit. Therefore, the primary reflector is made of graphite epoxy, with an egg-crate structure joining two skins, the front one coated with vacuum-deposited aluminum for the RF reflection and then with SiO_x for thermo-optical properties. The secondary and tertiary reflectors are diamond-turned aluminum, machined on the back to leave ribs. These reflectors are then grit-blasted to achieve the desired emissivity.

7.3.3 Selected Design

Figure 7-12 shows the signal flow diagram of EOS MLS. As with UARS, the incoming signal is split among the GHz radiometers using a multiplexer consisting of a wire grid polarizer and three dichroic plates. The feed mirrors coupling the antenna beam into corrugated horns on the GHz mixers have toric conic prescriptions, like those of UARS, to match the astigmatic beam coming from the 2:1-aspect-ratio antenna to the axisymmetric horn patterns.

A more significant departure from UARS is the antenna for 2.5-THz bands. The science requirements would have allowed use of the innermost part of the aperture for THz signal, and experience led us to expect that reflector figure errors would be dominated by components with long correlation length, so that the center portions could have a surface rms figure enough less than the entire reflector to beat back the growth of Ruze losses at a frequency four times higher than the next GHz band. However, there were enough differences in the scan pattern for OH retrieval, and the ability to perform both alignment and RF focusing through an optical surface was so attractive, that the THz instrument

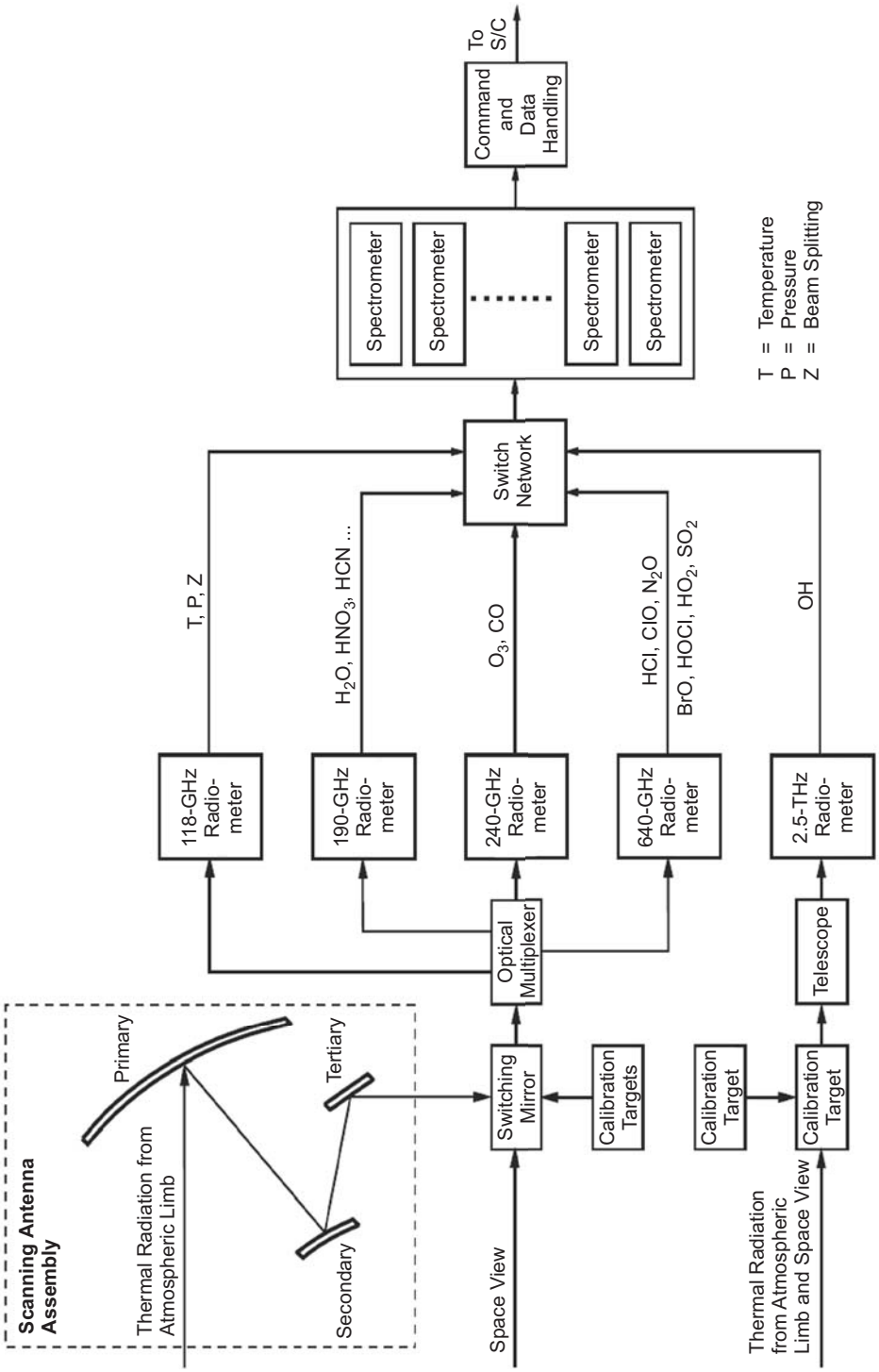

Fig. 7-12. Signal flow diagram for the Earth Observing System microwave limb sounder (EOS MLS) instrument.

was made a separate module. Another factor in separating the two modules was the environment needed for ground calibrations: Water vapor attenuates 2.5-THz signals by 1/*e* in 1 m of ambient air, so the THz calibrations, which require sources much weaker than those available at GHz frequencies, must be performed in vacuum.

Therefore, the THz optics design called for an offset Gregorian telescope with three diamond-turned mirrors, the primary having a 9-in. (22.86 cm) diameter. Beams were circular throughout the optics. The Gregorian design allowed for a pinhole (stop) between primary and secondary reflectors, which spatially filters the non-ideal feed patterns and provides a convenient reference for theodolite alignment looking into the telescope aperture. A diplexer, based on the Martin-Puplett design [23] and comprised of polarization grids and curved and roof-line mirrors, splits the signal and matches beams to two dual-mode horns. These are scaled from the UARS MLS design, and are machined into the input ports of the THz mixers. The diplexer also injects local-oscillator power from a gas laser. The THz FOV is scanned through the Earth limb, and to cold space and calibration load views using a plane scanning mirror; performing the calibration directly between telescope and limb removes the concerns with frequency-dependent spillover, which affect the GHz module optics.

Another innovation for the THz module is the use of a compact range to measure antenna patterns in the vacuum chamber. A test reflector was made with the same focal length but slightly larger than the THz primary reflector, A 900-deg C mercury arc (incoherent source) illuminated the compact range reflector through a slit to allow measurement of one-dimensional patterns with 0.01-deg sampling, using the radiometer power detection, over a range of ±1.3 deg using the scan/switching mirror. Since the radiance seen by the antenna in a limb-sounding orbit varies only in the limb vertical direction (for small horizontal angles), the slit was oriented to measure that direction of the pattern. This achieved in the test set-up what is done for the GHz module by quadrature of patterns measured in two dimensions. With this integration along the slit, the measurement technique achieved a dynamic range of –21 dB.

Water vapor attenuation precluded far-field pattern measurement for the GHz radiometer also. The attenuation is 95 dB/km in the 640-GHz bands, so atmospheric variability and even local weather make the far-field range (9 km required) infeasible. Submillimeter sources do not have sufficient power to illuminate the MLS at this distance; nor are there locations for siting transmitter and receiver in the JPL test facility without severe logistical and range reflection problems.

Using the experience of Goddard Space Flight Center (GSFC) with the Submillimeter Wave Astronomy Satellite, plus expertise gained from the microwave instrument for the Rosetta orbiter (MIRO) project described here, an 8-ft × 8-ft (2.44-m × 2.44-m) planar scanner was procured and phase-locking

electronics developed for near-field range measurement of the GHz module patterns. The planarity of the range, including scanner and electronics in the benign high bay environment, is 5 μm rms, a factor of two better than needed to meet the FOV calibration requirement. Boresight directions are determined between RF measurements using a system of theodolites that measure alignment cubes on the instrument relative to the scan plane coordinates, in which the RF pointing had been measured.

After assembly at JPL, the range was tested on the engineering model of the UARS MLS antenna, then used to baseline the pattern performance of the EOS MLS at a reduced set of scan angles and frequencies, for comparison before and after thermal vacuum tests of the GHz module.

Figure 7-13 is a photograph of the GHz engineering module of EOS MLS on the near-field range. The module is rotated 90 deg from its orientation on the Aura spacecraft to fit better with the preferred motion of the range and so that gravitational deformations affect mostly the limb horizontal plane, where requirements are less stringent.

7.3.3.1 Performance Estimates. The successful use of near-field (for GHz) and compact (for THz module) ranges was crucial in completing the FOV calibration datasets for EOS MLS. The calibration was accomplished in half the time allocated, and it gave unprecedented knowledge of the antenna performance at these frequencies. Radiometer feed patterns could be compared with the near-field patterns of the GHz module, and in one case inspection of near- and far-field patterns revealed a mechanical assembly error for one multiplexer element, which could be corrected within 2 days in the same high-bay environment. Table 7-12 compares the requirements with the measured performance for the EOS MLS beamwidths and beam efficiencies. Figure 7-14 shows principal plane co-polarized amplitude patterns at three frequencies of the 640-GHz MLS radiometer, taken in the near-field range FOV calibration of the GHz module.

Figure 7-15 shows compliance of the EOS MLS GHz boresights with the coincidence requirements, and it illustrates the pattern of footprint centers in the plane normal to boresight at the limb tangent point. The grouping of band centers corresponds to the small misalignments of polarizers and dichroic plates in the optical multiplexer. After integration on the Aura spacecraft, the THz instrument boresight co-alignment with the GHz boresights was 0.048 deg in the azimuth direction (1/4 of requirement), and was later made nearly 0 in the elevation direction by matching scan angles with spacecraft ephemeris and attitude data during flight operation.

7.3.3.2 Conclusions. Figure 7-16 is a photograph of the GHz and THz modules of EOS MLS on the Aura spacecraft prior to thermal vacuum test. A black-body target covered the THz aperture for this test.

Fig. 7-13. EOS MLS GHz module on near-field range.

EOS MLS was launched aboard the Aura spacecraft on July 15, 2004, from the Western Test Range of California's Vandenberg Air Force Base. The instrument produced useful spectra and geophysical retrievals within days after activation. In its first year of operation, the ground calibration of FOV performance was verified within pre-launch error bars, except for ohmic losses; these were overestimated for 240 GHz and underestimated for 640 GHz. The slight discrepancies have been attributed to fabrication differences between the primary reflector and the other two antenna reflectors. Calibration values were

Table 7-12. Requirements and measured performance of the EOS MLS FOV: beamwidth and beam efficiency.

GHz Band	HPBW Vertical (deg)		HPBW Horizontal (deg)		Beam Efficiency (percent)	
	Required	Measured Range	Required	Measured Range	Required	Measured Range
118 R1A	0.123	0.107–0.118	0.283	0.227–0.245	≥0.95	0.978–0.987
R1B	0.123	0.111–0.119	0.283	0.220–0.236	≥0.95	0.980–0.982
190 R2	0.085	0.074–0.084	0.189	0.147–0.168	≥0.95	0.959–0.980
240 R3	0.066	0.058–0.064	0.189	0.116–0.126	≥0.95	0.962–0.973
640 R4	0.028	0.0252–0.0271	0.189	0.0528–0.0572	≥0.95	0.962–0.967
2500 R5	0.047	0.038–0.046	0.189	N/A	≥0.95	1.0 ±0.05

corrected using special scans high above Earth's atmosphere. The correction highlights a significant contributor to stray radiance that will affect future sub-millimeter limb sounders.

7.3.4 Future Radiometer Missions

Future designs for Earth observation are driven more by the demand for greater spatial coverage than by increases in frequency (many of the spectra in [15] peak below 3 THz, above which spectral windows close rapidly due to clouds, rain, and water vapor). For the next generation of microwave limb sounding, the atmospheric region targeted by instrument concepts continues to move downward from the stratosphere to the upper troposphere, where events are more localized in both space and time, calling for greater Earth coverage than the tangent tracks of previous instruments. An azimuth-scanning version of the MLS (SMLS) under study [24] proposes to use toric symmetry in a compact multiple-offset reflector antenna system, which can be useful in the viewing geometry of limb sounding and with shorter integration times made possible by current receiver and cooler technology. An inflatable antenna concept, having a 25-m aperture in an offset parabolic torus configuration, was evaluated for remote sensing of soil moisture and ocean salinity in [25]. Both concepts avoid the need to move entire apertures mechanically for Earth coverage, preferring instead to under-utilize very large apertures having some circular symmetry. This will generate instantaneous FOVs that have moderate performance but nearly identical properties across the swath.

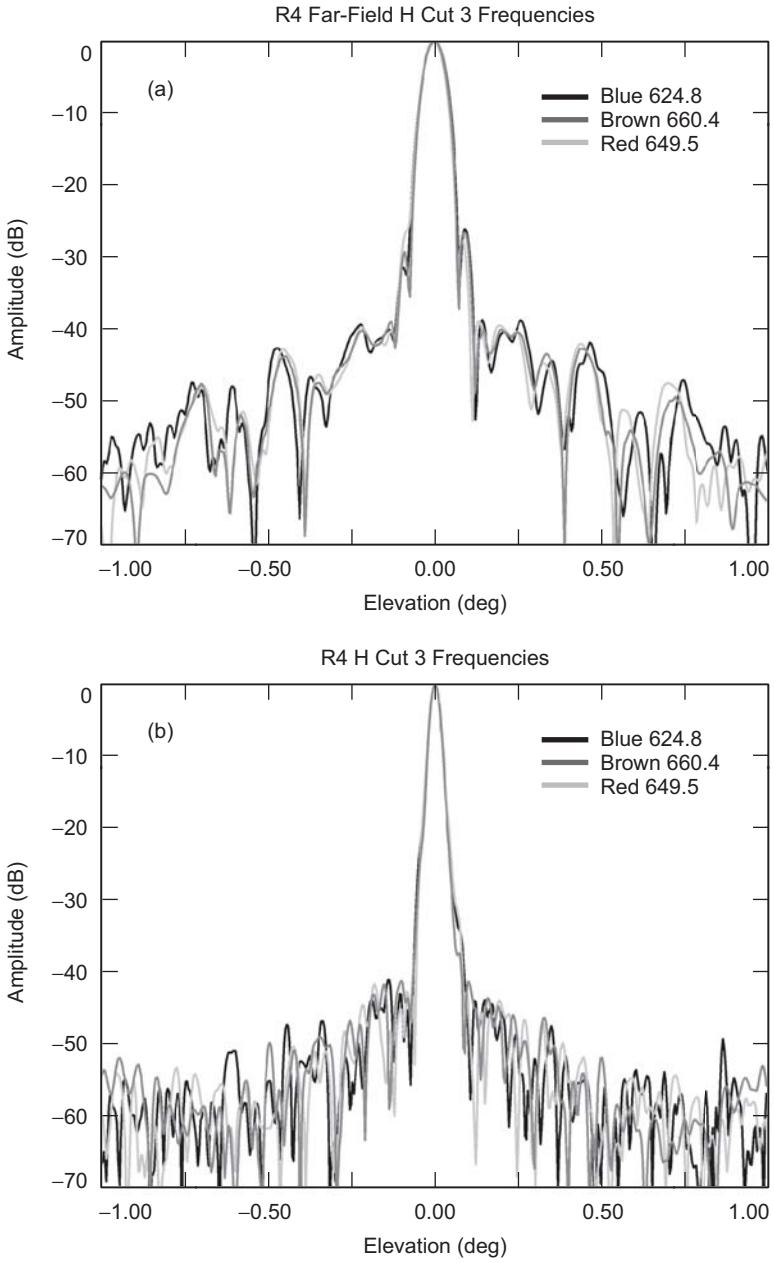

Fig. 7-14. Antenna pattern cuts in principal planes at three frequencies in the 640-GHz bands of EOS MLS: (a) V cut and (b) H cut.

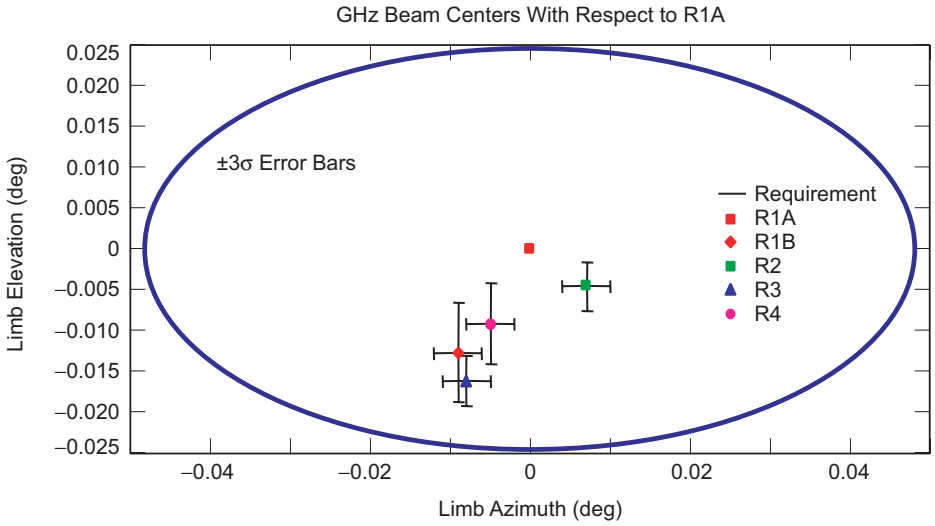

Fig. 7-15. Boresight coincidence of EOS MLS GHz radiometers.

7.4 Scatterometers

Richard E. Cofield

A scatterometer is a microwave remote sensing instrument using an amplitude-calibrated radar for measuring the scattering coefficient σ^0 (bi-static scattering cross-section per unit area). The strong dependence of σ^0 on incidence angle led to development of fan-beam Doppler antenna systems capable of simultaneous measurement over incidence angles from 5 to 60 deg. The Doppler filtering is a unique advantage of fan-beam scatterometry, using the time domain to replace multiple beam systems for horizontal resolution. An equally strong dependence of σ^0 on wind direction relative to the radar azimuth angle is the basis for measurement of vector winds by scatterometers. It was found in early experiments that the scattering coefficient at $\lambda = 2.2$ cm wavelength interacts with capillary waves induced by local winds at speeds down to 3 m/s. However, the dependence is weak, and hence the operating frequency can be chosen somewhat freely (as is not the case in radiometry) to trade radar power against antenna gain; hence, early scatterometers operated from 4 to 11 GHz; while their spaceborne descendents operate from 10 to 15 GHz.

The impetus for making scatterometers to operate from Earth orbit began with the confirmation, by a scatterometer flown aboard Skylab in 1973–1974, that the scattering coefficient varies monotonically with wind speed over the ocean—a prime candidate for global remote sensing. The measurement depends on both surface roughness and Bragg scattering from ocean surface areas

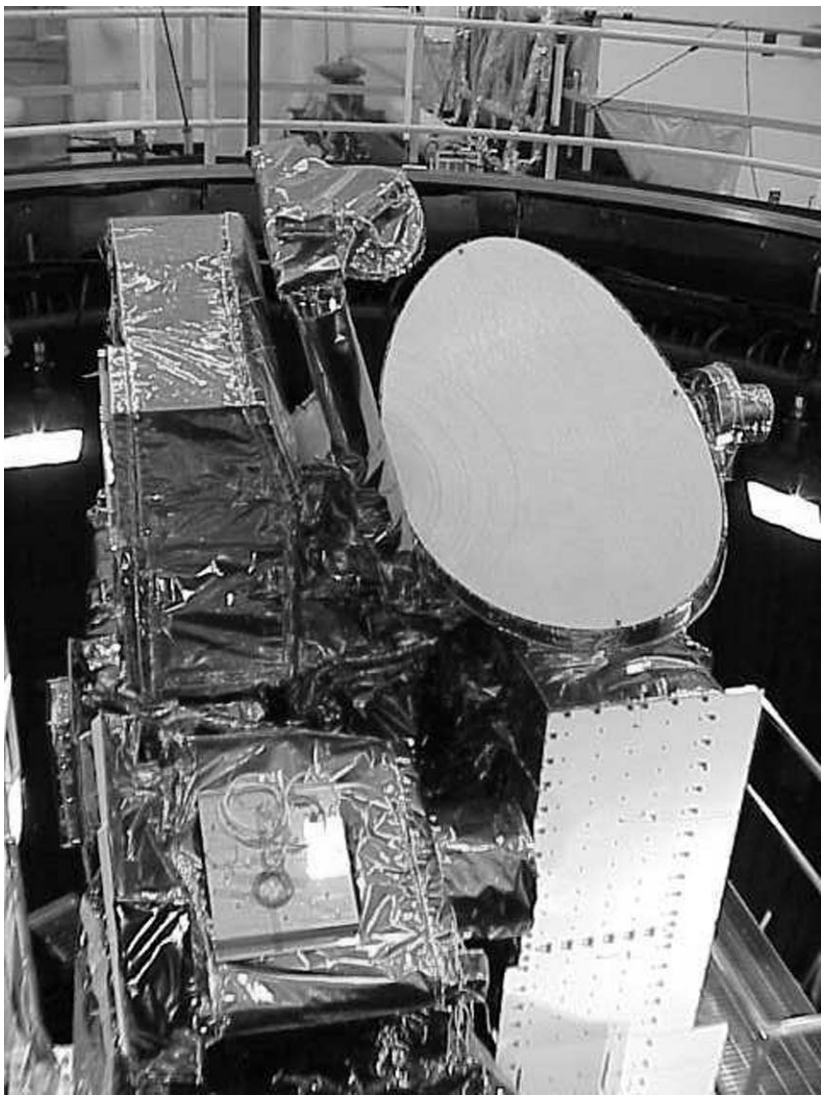

Fig. 7-16. EOS MLS GHz and THz modules on Aura spacecraft for thermal vacuum test.

spatially correlated over scales comparable to the radar wavelength, given some statistical variation of incidence angle [26].

7.4.1 Fan-Beam Instruments: Seasat-A Scatterometer

The Seasat-A scatterometer system (SASS), a Doppler scatterometer with four orthogonal fan beams, was developed for the Seasat oceanographic

satellite [27]. Wind retrieval was based on an empirical model for σ^0 as a linear function of the logarithm of wind speed, developed using results from both Skylab and other (aircraft) instruments. Mission requirements for SASS were to measure wind speed within ±2 m/s and wind directions within ±20 deg.

7.4.1.1 Requirements. Gain errors, both peak (G_0) and per-Doppler cell (G/G_0), and narrow dimension HPBW (φ_A), all contribute to fixed-bias errors. The gain knowledge errors contribute 90 percent, and HPBW 5 percent, of the sources of error contributing to ±0.84 dB rms uncertainty of σ^0. Antenna pointing errors and spacecraft attitude errors translate to errors in G/G_0. Attitude errors were not systematic, but 0.1-deg knowledge of antenna squint angle was determined in flight and found to be affected by orbital thermal variations up to 15 deg C over the length of the antenna, and 11 deg C over one orbit.

Figure 7-17 shows the viewing geometry of the Seasat-A Satellite Scatterometer (SASS). The footprints of the four antennas cover a swath extending 950 km on either side of the subsatellite track. This is divided into two swaths on either side, in which winds were to be retrieved at various speeds depending on incidence angle, and a third swath centered on the nadir track (small incidence angle θ_i). Earlier aircraft measurements had indicated that σ^0 was independent of surface roughness near θ_i = 10 deg. When a constraint on SASS design provided a channel at 8 deg instead of the desired 10 deg, it was hoped that the center swath would indicate instrument stability; later refinements moved the σ^0-invariant point to 13 deg, and the center swath data was not a useful indicator of stability, except in low wind speeds of 2–10 m/s [27]. In designing subsequent fan-beam scatterometers to measure winds, the center swath, having small θ_i, was removed from mission requirements; the resulting gap later led the fan-beam design into disfavor, as described below.

Ground truth for validating performance of the SASS instrument and algorithms was obtained from 11 orbits over the Amazon jungle, for which Skylab data had shown σ^0 to be isotropic and polarization insensitive. After partitioning the data set into early-morning and afternoon passes, the scatterometry was shown to perform near theoretical limits over periods up to 150 s with long-term stability better than a few tenths of 1 dB.

The flawless performance of the SASS instrument over the short lifetime of Seasat, and success of its algorithms in meeting the mission requirements, led to JPL's next spaceborne fan-beam scatterometer.

7.4.2 Fan Beam Instruments: NASA Scatterometer (NSCAT)

The NASA scatterometer (NSCAT) project was started in 1985 with plans to build on the Seasat experience with another set of fan-beam antennas flown aboard a Navy satellite in 1988; however, several delays prompted cancellation

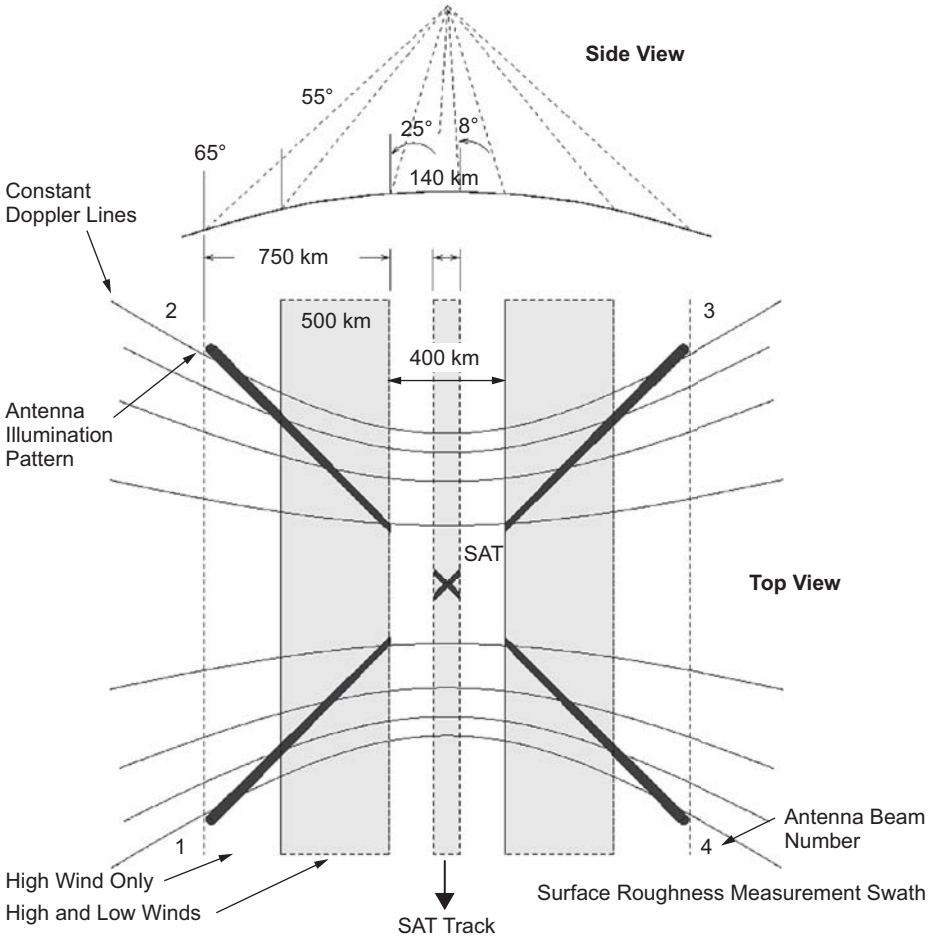

Fig. 7-17. Viewing geometry of the Seasat-A satellite scatterometer (SASS), from [27].

of that satellite program, leaving NSCAT to await a launch on the Advanced Earth Observation Satellite (ADEOS) by Japan's Space Agency NASDA.

The principal objective of NSCAT and its successors is vector winds measurement at the ocean surface, which is crucial for understanding air-surface dynamics. Altimeters and radiometers can measure wind speed but not direction except for recently developed polarimetric radiometers. Using a near-polar orbit, coverage is global, and measurements can be made in all weather conditions. Like SASS, NSCAT operates at 14 GHz. Table 7-13 gives the NSCAT mission objectives.

7.4.2.1 Trade-off Studies. Antenna systems for scatterometry have been of either the Doppler filtered-fan beam class or the scanned spot-beam class. The

Table 7-13. Major NSCAT mission objectives.

Parameter	Value
Wind speed	2 m/s rms for 3–20 m/s 10 percent for 20–30 m/s
Wind direction	20 deg rms for 3–30 m/s
Spatial resolution	25 km for σ^0 cells 50 km for wind cells
Location accuracy	25 km rms absolute 10 km rms relative
Coverage	90-percent ice-free ocean every 2 days
Mission lifetime	36 months

fan-beam design was chosen for NSCAT because of SASS heritage, particularly in the wind-retrieval algorithms.

Because scatterometry of ocean winds needs collocated radar reflections from multiple azimuths and a wide swath for global coverage, antenna design is the most severe constraint in a spaceborne scatterometer instrument. σ^0 depends weakly on wind speed and direction for near-normal incidence; this dictates large incidence angles which also incur a swath gap about the subsatellite track. The resulting instantaneous footprints are several hundred kilometers long but only few kilometers wide, and they have large variation in incidence angle near grazing incidence.

Among several enhancements of the Seasat instrument, the most significant for the antenna is addition of another antenna on each side, i.e., three antenna azimuths in each of two swaths to reduce fourfold ambiguity in wind direction in the SASS measurements.

7.4.2.2 Selected Design. Figure 7-18 is an artist's concept of the NASA scatterometer on the ADEOS spacecraft, showing antennas deployed plus footprints and swath coverage of the Earth NSCAT beam geometry: Each of two 600-km swaths on each side is swept out by three antennas: one at 45-deg azimuth from the orbit plane and H-polarization; one at 135-deg azimuth, V-polarization; and one at 65-deg azimuth, (forward one side, backward the other), H and V-polarization; For horizontal resolution, the 600-km swath is divided into 24 cells, each 25 km wide. In the 795-km orbit (101-minute period) of the ADEOS platform, the ground track velocity is 6.7 m/s, hence to make the along-track resolution also 25 km, NSCAT must cycle through all eight antennas in 3.74 s [28].

The NSCAT Antenna subsystem consists of six identical fan-beam antennas and associated deployment mechanisms. Each antenna is composed of two separate horns fed by a slotted waveguide array; only one polarization is

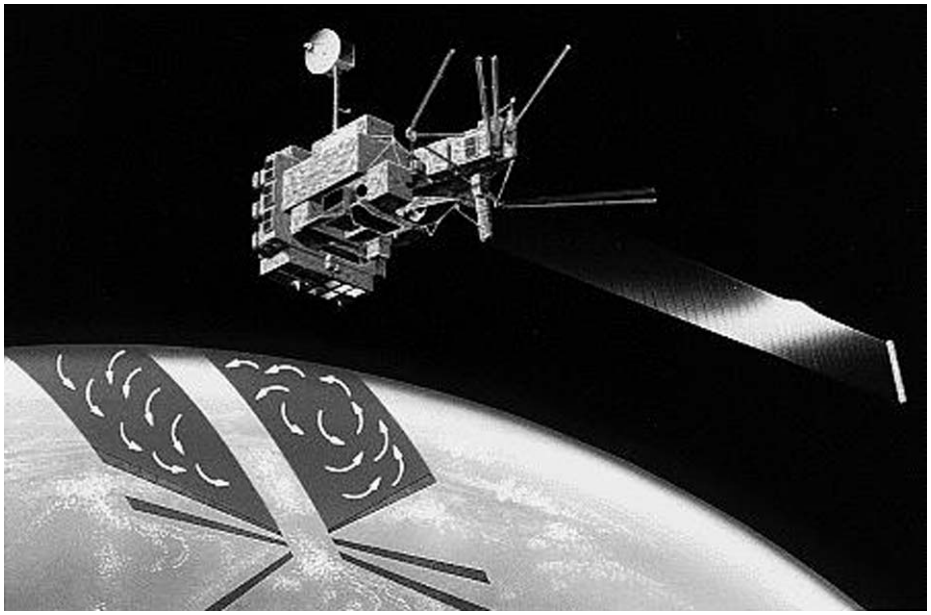

Fig. 7-18. NSCAT scatterometer on the ADEOS spacecraft.

used for all but the two 65-deg azimuth antennas. The horn walls are made of graphite-epoxy for dimensional stability in the orbital thermal environment. Thin aluminum foil provides the conducting surface inside the horn, and the 202-slot waveguide is also aluminum. Horn dimensions are 120 in. (305 cm) long, 2.5 in. (6.35 cm) wide, and 4.5 in. (11.43 cm) deep, to produce the desired fan beam. Figure 7-19 is an end view of one dual-horn flight antenna.

Nominal peak gain is 33.5 dB, tilted toward the far swath to compensate for longer slant range there. The first sidelobes have relative intensities of –15 and –20 dB in the wide and narrow beams, respectively. Antenna requirements and performance measured by the vendor are in Table 7-14, from [29]. These results were duplicated and augmented with alignment information when the antennas were calibrated on the cylindrical near-field range at JPL.

Transforming the NSCAT mission requirements into antenna specifications revealed two key performance requirements: (1) Signal-to-noise ratio (SNR) shall exceed –8 dB for 3 m/s winds, and (2) the combined rms variation due to antenna pattern knowledge, beam pointing, and other non-antenna effects shall not exceed 0.5 dB, 1 σ over 8 minutes. With the long delay between antenna fabrication and integration of NSCAT on a new platform, it was necessary to repeat antenna measurements in a more rigorous fashion before delivery, in order to demonstrate compliance with these requirements.

Antenna gain was calibrated during ground test to 0.25 dB, with in-orbit gain variations to be corrected using temperature data from sensors mounted

Fig. 7-19. Dual-polarized NSCAT flight antenna, end view.

Table 7-14. Required and measured performance of the NSCAT antennas.

		H-Polarization			V-Polarization		
			Flight Predict.[a]			Flight Predict.[a]	
Parameter	Required	Measured	Low	High	Measured	Low	High
Frequency			13.995 ±5 MHz				
HPBW (narrow beam) (deg)	0.41 ±0.02	0.41 ±0.01	0.40	0.42	0.42 ±0.01	0.40	0.42
Squint (narrow beam) (deg)	1.75 ±0.25	1.81 ±0.01	–1.78	–1.81	–1.72 ±0.01	1.69	1.72
Gain (dBi)	33.5, Goal 34	33.64 ±0.37	33.62	33.53	34.1 ±0.37	34.15	34.16
Sidelobes (dB)	–20 below peak	–20.2 ±0.7	–22.3	–19.9	–22.6 ±0.7	–22.1	–21.9

[a] Low predicted temperature of –129 deg F (–89 deg C); high predicted temperature of 182 deg F (103 deg C).

along the horn length. The ground patterns were measured on a cylindrical near-field range coaxial with the phase center line along the slotted waveguide. [30]

Alignment of the range fixture and waveguide mechanical features to alignment cubes gave knowledge of the RF and mechanical boresights with respect to the interface with the deployment hinge. Further cube-to-cube

alignments then allowed this alignment knowledge to be transformed back to the attitude control system of ADEOS.

One issue which arose late in the program of pattern calibration was whether to fly with or without covers over the horn apertures; this has been a perennial question with radiometer missions also. Expected thermal deformations made the covers highly desirable, but as the original vendor measurements of Table 7-14 show, a small price would be paid in sidelobe level at extreme temperatures. The principal effect of the covers, a pointing change, was accounted for by the alignment portion of the calibration. NSCAT was flown with covers. This is in contrast to the radiometer missions: despite much smaller horn throats at the higher frequencies, the degradation in voltage standing wave ration (VSWR) and resultant spectral baseline were deemed even worse than the risk of contamination, so the radiometer instruments have flown without horn covers.

Table 7-15 shows how uncertainties in pre-launch calibrations of antenna gain, beamwidth, and pointing contributed to bias and time-varying components of uncertainty in σ^0.

NSCAT was launched August 16, 1996 aboard the ADEOS spacecraft from Tanegashima, Japan. It operated from September 1996 until failure of the spacecraft power system on June 30, 1997. A post-launch calibration campaign, begun shortly after turn-on, confirmed the ground calibrations of antenna gain, sidelobes, and nominal antenna deployment. Antenna pointing was calibrated in orbit by three methods:

1) A calibration ground station was deployed, capable of both transmitting to and receiving from NSCAT. Antenna gain patterns in the narrow-beam

Table 7-15. Pre-launch calibration of the NSCAT antennas.

Antenna Calibration Parameter	Pre-launch Calibration Bias		Time-Varying Calibration Error	
	Parameter Error	σ^0 Error	Parameter Error	σ^0 Error
Peak gain	0.35 dB	0.7 dB (2-way)	0.10 dB	0.20 dB (2-way)
Broad-beam pattern	0.02 dB/dB	0.40 dB max (2-way)		
Beam width	0.015 deg	0.16 dB	0.005 deg	0.05 dB
Squint	0.05 deg	0.09 dB max	0.007 deg	0.01 dB
Pointing	0.05 deg each axis	0.05 dB	0.08 deg each axis	0.13 dB
Other contributors, rss	—	0.61	—	0.19
rss sums	Pre-launch bias = 1.03 dB		K-factor = 0.31 dB	

Uncertainty of post-launch bias removal: 0.2 dB beam-to-beam, 0.5 dB absolute

direction were measured during NSCAT overpasses and the beam peak used to infer spacecraft attitude.

2) Natural targets, such as the Brazilian rain forest (as described previously for SASS) and central Russia, were observed along with beam-to-beam bias over open ocean.

3) Attitude was determined independently, using raw housekeeping data.

All three methods indicated that attitude varied over one orbit by as much as a few tenths of 1 deg—an order of magnitude higher than the reported ADEOS stability. This resulted in uncertainty in σ^0 of a few tenths of a dB. Comparison of NSCAT wind vectors with *in-situ* data, from 27 moored open-ocean buoys, indicates that NSCAT met science requirements for wind speed and direction accuracy [31].

7.4.3 Pencil-Beam Scatterometers: QuikSCAT and SeaWinds

The SeaWinds on QuikSCAT mission was a "quick recovery" mission to fill the gap created by the loss of data from the NASA Scatterometer (NSCAT), when ADEOS lost power in June 1997, until a second SeaWinds could be deployed on the ADEOS-II satellite. SeaWinds instruments for QuikSCAT and ADEOS-II are functionally identical, but the platform attitude controls differ: a star tracker on QuikSCAT gives 0.05 deg attitude knowledge (3σ), whereas ADEOS-II used Sun/Earth sensors and gyros to attain 0.2 deg (3σ) [32]. Table 7-16 summarizes the science requirements of the SeaWinds missions, which are very similar to those of NSCAT.

Scatterometers developed at JPL after NSCAT were designed with conically-scanned pencil beams, to avoid several drawbacks of the fan-beam approach: With satellite motion, two conically scanned beams (which can share

Table 7-16. SeaWinds science requirements.

Measurement Parameter	Performance Requirement	Instrument Performance
Wind field resolution	50 km; 25 km goal for data products	3-dB beamwidth + pulse modulation
Wind speed accuracy	The greater of 2 m/s and 10-percent rms of wind speed	Post-launch science analysis to show requirement is met
Wind direction accuracy	Less than 20 deg rms	Post-launch science analysis to show requirement is met
Coverage; revisit period	90 percent of global sea surface every 2 days	Orbit design and swath coverage of 1800 km
Mission life	3 years; 5 years goal	Flight qualified parts and materials; key electronics redundancy

the same reflector antenna system) trace out helical footprint paths which overlap at different points along the orbit track, meeting the scatterometry requirement to measure each surface element from different azimuths. Moreover, a full conical scan will measure at a given ocean surface point twice, once from the forward and once from the backward-looking part of the scan. The nadir gap vanishes, directional accuracy is inherent in the beam and not a function of Doppler gating, and the retrieval is simplified by having measurements at a small number of incidence angles. Finally, the pencil-beam concept occupies much less space on the platform, since a compact dish replaces the multiple fan-beam antennas. Cost and risk are less for the continuously rotating conical scan mechanism than for the older concept, which involved one-time deployment and had greater susceptibility to orbital thermal gradient [33].

Table 7-17 gives the measurement geometry and antenna specifications for the SeaWinds scatterometer. Figure 7-20(a) shows the conical spot-beam illumination. The antenna designed for the SeaWinds instruments (Fig. 7-20(b)), is a parabolic reflector with an elliptical projected aperture. The antenna is built of composite lightweight material (this includes the reflector surface shells, waveguides, struts, and feed horns) and has an rms surface error of 0.2 mm. It is oriented at an angle of 43 deg from nadir, as illustrated. The

Table 7-17. Viewing geometry and antenna specifications for the SeaWinds scatterometer.

Parameter	Inner Beam	Outer Beam
Polarization	H	V
Half-cone angle from nadir	40 deg	46 deg
Surface incidence angle	47 deg	55 deg
Slant range	1100 km	1245 km
3-dB footprint dimensions (az × el)	34 × 44 km	37 × 52 km
Rotation rate	18 rpm	
Along track spacing	22 km	
Along scan spacing	15 km	
Instrument frequency	13.402 ±0.5 GHz	
Expected range of σ^0	–37 to –2 dB	
3-dB beam dimensions (az × el)	1.8 deg × 1.6 deg	1.7 deg × 1.4 deg
Antenna peak gain	38.5 dBi	39 dBi
Antenna peak side lobe	–15 dB or less	
Minimum antenna resonant frequency	>94 Hz	

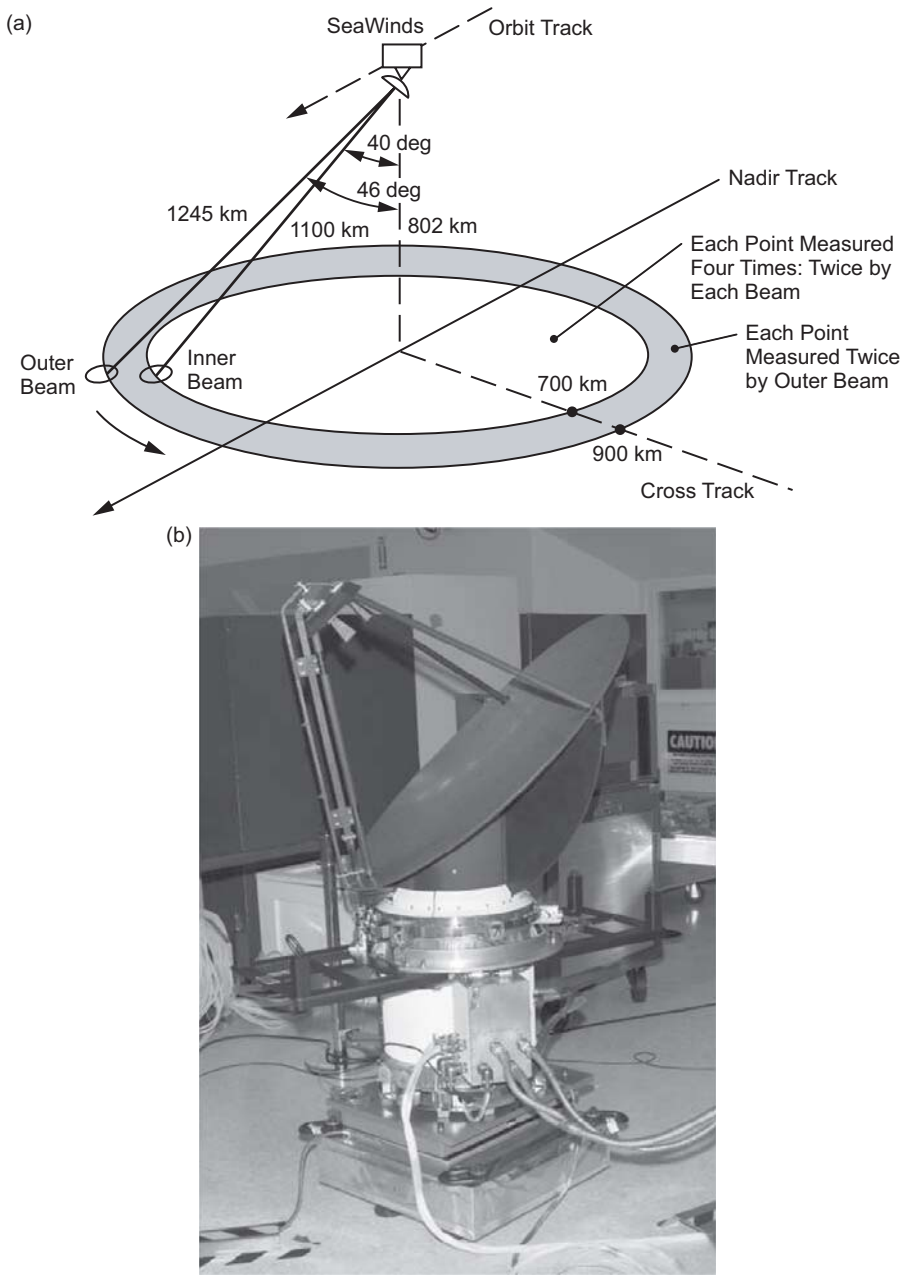

Fig. 7-20 (a) SeaWinds conical-scan spot-beam scan pattern and (b) 1.07 m x 0.96 m Ku-band SeaWinds dual-feed reflector antenna. The reflector shell, waveguides, and feeds are made of lightweight composite material (total weight is 6.40 kg).

projected elliptical aperture of the antenna is 1.07 × 0.96 m for the major and minor axis, respectively. Two feed horns are each displaced 0.0345 m from the boresight axis of the antenna to produce two independent pencil beams at angles of 40 deg and 46 deg from nadir. The inner beam (beam closer to nadir) has horizontal polarization; the outer has vertical [34].

SeaWinds antenna patterns were measuring using a cylindrical near-field range (CNFR) developed for NSCAT. This range was qualified for SeaWinds by measuring both a standard gain horn and the SeaWinds antenna, on both the CNFR and a 3000-ft (915-m) far-field range at JPL (9 times longer than $2D^2/\lambda$).

Figure 7-21 shows the principal plane cuts of the SeaWinds antenna beams, from both near- and far-field measurements. Coma lobes are evident in the elevation plane patterns, as expected for scanning 2 to 3 times HPBW in an f/D ~1 system. Even though inner and outer beam feeds were displaced symmetrically from the focus of the paraboloid, the outer beam's first sidelobe is higher by 5 dB. Nevertheless, at –15 dB down from main beam peak it still meets the requirement. Table 7-18 summarizes requirements and measured performance of the SeaWinds antenna for both inner and outer beams, before and after vibration tests.

QuikSCAT was launched on June 19, 1999, from Vandenberg Air Force Base, California, into a nearly polar orbit with a maximum altitude of about 800 kilometers, and it has continued operation to the present. The second SeaWinds instrument was launched December 14, 2002, aboard ADEOS-II, renamed Midori-2, and it operated until a solar storm in October 2003 caused permanent loss of the satellite.

7.4.4 Future Scatterometer Missions

Loss of the Midori-2 spacecraft left JPL with only the QuikSCAT scatterometer operational and has created a loss of coverage in measurement of vector winds. Currently planned JPL missions are addressing this gap with concepts involving large deployed apertures in pencil-beam configuration, possibly teamed with next-generation radiometers (for atmospheric and oceanic science) as was done in the 1978 Seasat mission.

7.5 CloudSat

William A. Imbriale

CloudSat (scheduled for launch in the fall of 2005) is a multisatellite, multisensor experiment designed to measure those properties of clouds that are critical for understanding their effects on both weather and climate. The mission's primary science goal is to furnish data needed to evaluate and improve the way clouds are parameterized in global models, thereby contributing to better predictions of clouds and thus to the poorly understood cloud-climate feedback problem.

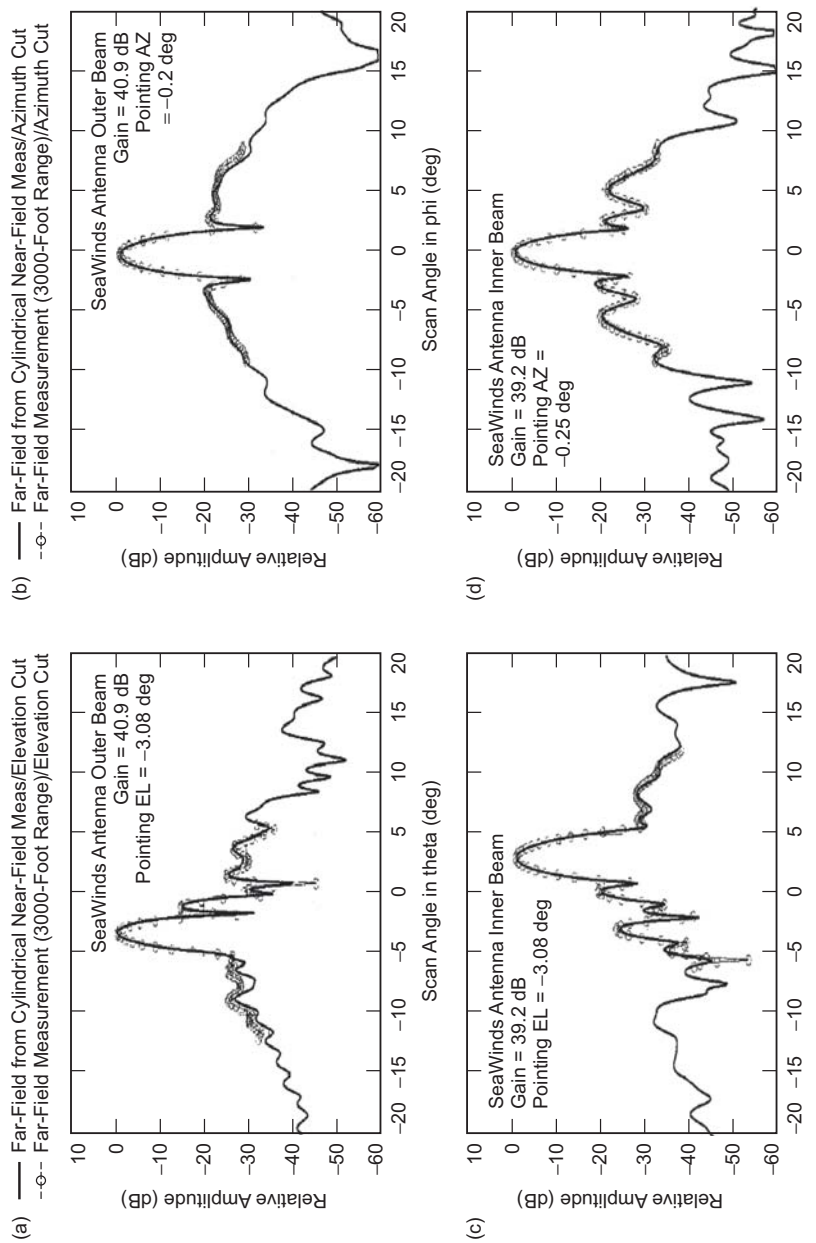

Fig. 7-21. Antenna pattern cuts of inner and outer beams of the SeaWinds antenna, from [30]. Co-polarized principal plane cuts from both near- and far-field measurements are shown: (a) outer beam, elevation; (b) outer beam, azimuth; (c) inner beam, elevation; and (d) inner beam, azimuth.

Table 7-18. SeaWinds antenna performance through vibration tests.

	Gain	X-pol*	Beamwidth		Pointing	
	dBi	dB	Az (deg)	El (deg)	El (deg)	Az (deg)
V-Polarization						
Requirement	>39.5	<–20	1.4 ±0.1	1.7 ±0.1	46 ±0.1	—
Post-vibration	40.91	–25.63	1.35	1.69	46.08	–0.05
Pre-vibration	40.86	–25.56	1.34	1.7	46.08	+0.05
Difference	0.05	0.07	0.01	0.01	0.00	0.1
H-Polarization						
Requirement	>39.2	<–20	1.6 ±0.1	1.8 ±0.1	40 ±0.1	—
Post-vibration	39.27	–26.97	1.66	1.76	40.01	0.00
Pre-vibration	39.22	–26.54	1.66	1.76	40.02	+0.10
Difference	0.05	0.42	0.0	0.0	0.01	0.1

* relative to co-polarized beam peak

The key observations are the vertical profiles of cloud liquid water and ice water contents and related cloud physical and radiative properties. The spacecraft payload consists of a 94-GHz cloud profiling radar (CPR). CloudSat will fly in tight formation with the Cloud-Aerosol Lidar and Infrared Pathfinder Satellite Observation (CALIPSO) [35] satellite (formerly known as PICASSO-CENA/ESSP3) carrying a backscattering lidar, and these two satellites will follow behind the Aqua satellite [36] in a somewhat looser formation. The combination of data from the CloudSat radar with coincident measurements from CALIPSO and Aqua provides a rich source of information that can be used to assess the role of clouds in both weather and climate.

7.5.1 Cloud Profiling Radar (CPR)

The CloudSat cloud profiling radar (CPR) [37] provides calibrated radar reflectivity (i.e., radar backscatter power) as a function of distance from the spacecraft. The design has a strong heritage derived from existing ground-based [38] and airborne cloud radars [39].

The choice of radar frequency, 94 GHz, is a trade-off between sensitivity, antenna gain, atmospheric transmission, and radar transmitter efficiency. Sensitivity and antenna gain increase with frequency while atmospheric transmission and transmitter efficiency decrease with frequency. Since a space-based platform sets strong constraints on antenna size, a frequency of 94 GHz provides an optimum compromise between the competing factors. An international frequency allocation at 94 GHz has recently been set aside for spaceborne radar use. The choice of frequency means that a small percentage of

the time when very thick clouds or heavy precipitation is present, CPR will not be able to penetrate to the cloud base. The mission objective dictates this choice.

The CPR consists of six primary subsystems. The digital subsystem performs the timing and control of the radar, and acquires and processes the reflectivity data. The upconverter generates and up-converts the lower frequency pulse to 94 GHz. The high-power amplifier consists of an extended interaction klystron (EIK), which amplifies the 3.33-μs long transmitted pulse to 1.5 kW peak, and a high-voltage supply that provides 16 kV. The power distribution unit supplies power to all the low-voltage electronics.

The antenna subsystem, which is shown in Figs. 7-22 and 7-23, consists of a quasi-optical transmission line (QOTL) and a collimating antenna. The QOTL couples the transmitted (or received) signal to (from) the collimating antenna and provides the required duplexing function to separate the transmitted and received 94-GHz radar pulses. The QOTL has three mirrors, a ferrite Faraday rotator, and a wire-grid polarizer. The collimating antenna focuses the radiation and reception of the 94-GHz pulses with the required gain and radiation pattern. It has three mirrors: a large shaped primary (M1) that implements an ~1.85-m wide noncircular radiating aperture, a shaped secondary (M2), and a third mirror (M3) that is used to properly relay the energy to the QOTL.

7.5.2 Antenna Requirements

The CloudSat instrument is driven by several mission and science requirements. Particularly relevant to the antenna system is the 1.5-dB absolute reflectivity measurement accuracy goal, the less than 2-km diameter instantaneous Earth surface radar footprint, the low sidelobe envelope (50 dB below gain peak for angles larger than 7 deg from boresight), and the –26 dBZ minimum detectable cloud reflectivity at the end of the 2-year mission (dBZ is a weather radar unit that corresponds to decibels relative to a reflectivity factor Z of 1 mm^6/m^3 [40]). These requirements drive the 94-GHz frequency choice, the collimating antenna topology and aperture size, and the required antenna system efficiency. The details of the antenna subsystem design and the performance measurements were derived from [41] and the various design review packages.

7.5.3 Quasi-Optical Transmission Line

The QOTL performs two functions in the CPR: signal relaying and duplexing. More specifically, when the CPR transmits, the QOTL delivers the RF energy pulse from the EIK to the collimating antenna. When the CPR receives, the QOTL delivers the reflected signal from the collimating antenna to the receiver. Since the radiated transmitted and received signals have identical frequency and linear polarization, the required duplexing is accomplished

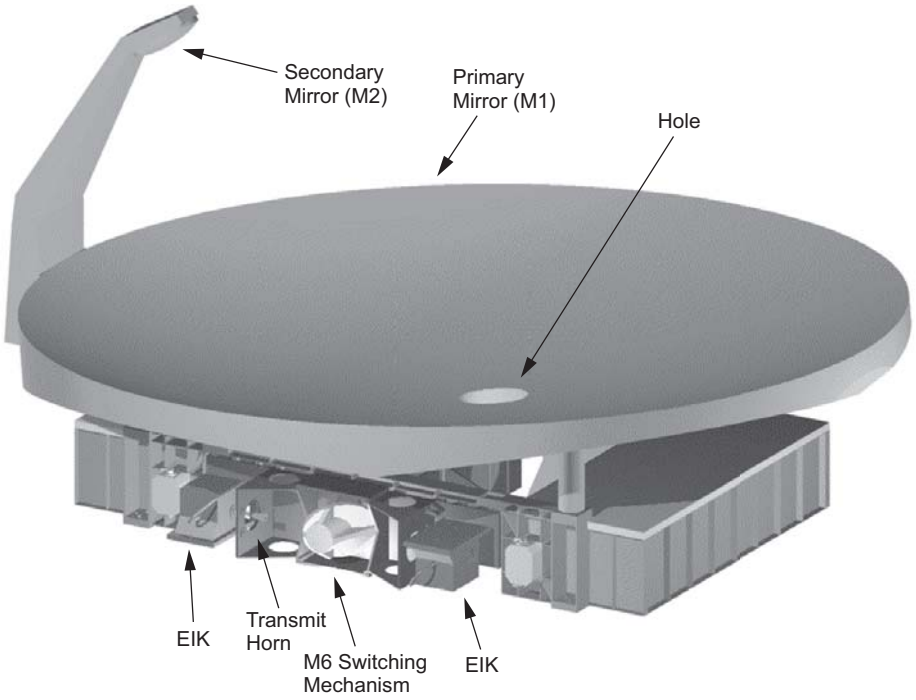

Fig. 7-22. CloudSat antenna system (EIK = extended interaction klystron).

through the use of a non-reciprocal component (a Faraday rotator) and a polarization grid located in the path common to both the transmitted and received signals [42]. The Faraday rotator creates a spatially orthogonal polarization relationship between the transmit and received signals, which are then separated by the polarization grid. Distinct feed horns are used to transmit and receive. To increase reliability, the CPR has two independent EIKs and associated feed horns, which are selected by the mirror M6 (see Fig. 7-22) and its switching assembly. Note that all horns are identical, as well as mirrors M5 and M6.

The schematic drawing of Fig. 7-24 details the operation of the QOTL. The transmitted 94-GHz pulse emanates from the active EIK through its corresponding feed horn. The pulse then reflects at the switching mirror, passes through the polarizing grid, and then passes through the Faraday rotator, which spatially rotates the linear polarization by 45 deg. From the Faraday rotator the beam heads to the collimating antenna. The returned radar pulse is received by the collimating antenna and routed to the Faraday rotator, where the field is rotated an additional 45 deg in the same direction as the transmitted pulse. The pulse leaving the Faraday rotator is then spatially filtered by the polarization grid, which reflects towards the receive horn only the component orthogonally

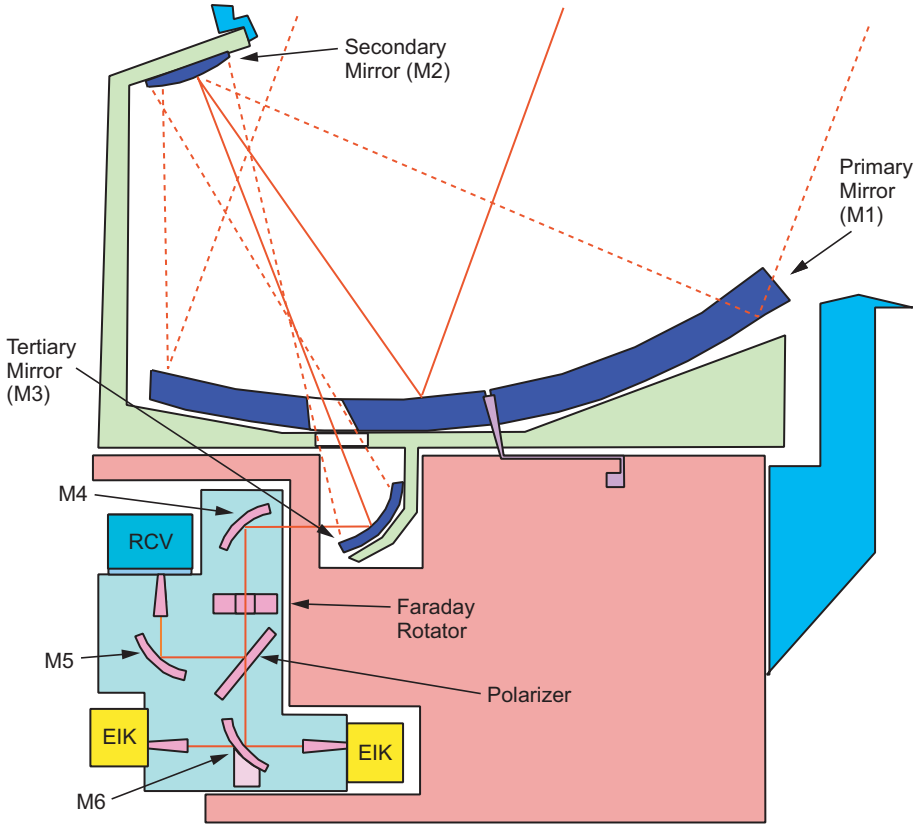

Fig. 7-23. CloudSat antenna system block diagram.

polarized to the transmitted signal at the polarization grid. Because of the net 90-deg rotation, the pulse that reaches the receive horn is co-polarized with the transmitted pulse at the collimating antenna aperture. The actual implementation of the QOTL (as shown in Fig. 7-22) uses extra mirrors M4 and M5 to route the signals in the proper direction.

The pulse-relaying and duplexing tasks of the QOTL can in principle be accomplished by waveguides and circulators. However, the relatively large physical size of the EIKs determined their location on the CloudSat spacecraft bus and would have imposed relatively long waveguide runs. Since a typical WR-10 waveguide has about 3.3 dB/m of loss at 94 GHz, the utilization of the QOTL (with its free-space propagation advantage) yields substantially less loss to the antenna system.

7.5.3.1 Requirements. The requirements for the QOTL are summarized below:

- Transmit loss: 0.5 dB

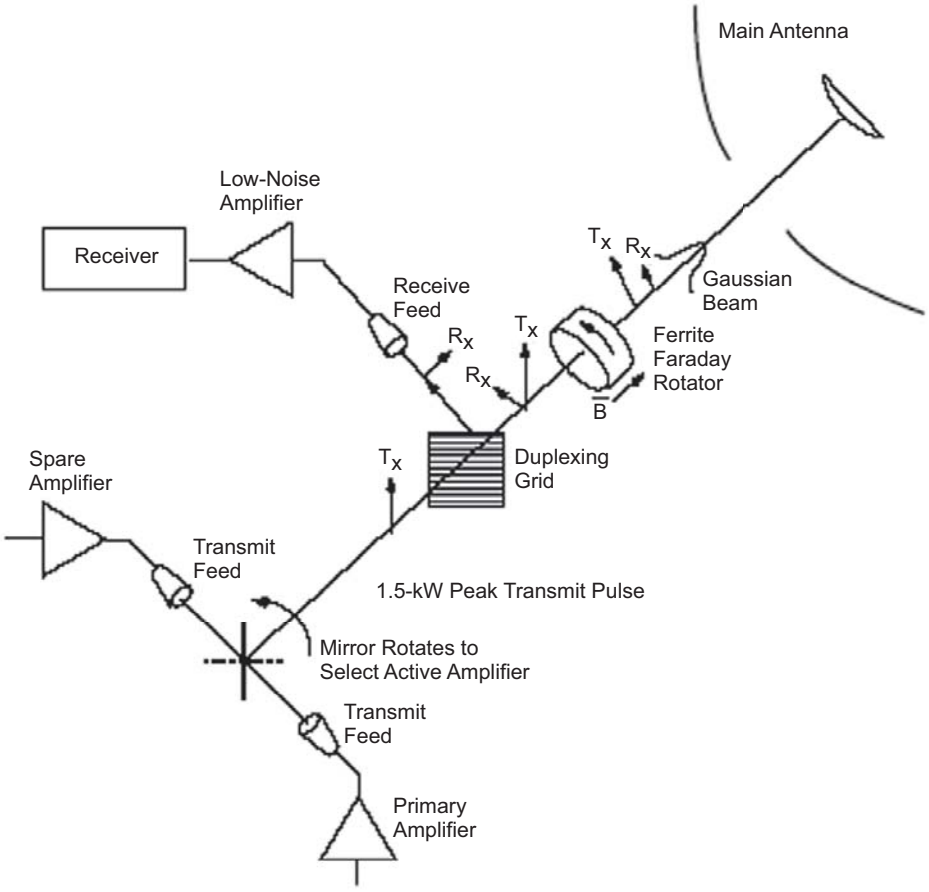

Fig. 7-24. CloudSat quasi-optical transmission line schematic drawing.

- Receive loss: 0.5 dB
- Isolation: 35 dB
- Power handling capacity: 2.0 kW, peak
- Operating temperature: –20 to +65 deg C
- Vibration: 9.8 grms, first mode: 70 Hz
- Magnetic: residue dipole < 0.1 A/m^2, 25 G demagnetized

To facilitate the QOTL and collimating-antenna development efforts, a circular corrugated test horn was designed to provide test excitation to both mirror M4 of the QOTL and mirror M3 of the collimating antenna. Use of this horn allowed the QOTL and collimating antenna to be developed and tested almost independently of each other, and combined only in the last stages of the program (an important convenience since the two systems were developed separately). This was possible because in the ideal case where the radiation

pattern of M4 (with the QOTL transmitting) and the radiation pattern of M3 (with the collimating antenna receiving a plane wave) are conjugate matched, the coupling of the QOTL and the collimating antenna will have no loss due to pattern mismatch [43]. The design goal was then to have the QOTL and the collimating antenna match the pattern of the test horn, which was designed for a nearly invariant radiation pattern from the far zone up to 100 mm from the horn aperture. The calculated radiation pattern of the test horn is depicted in Fig. 7-25.

7.5.3.2 Polarizer Design. The polarizer separates the received signal from the transmitted signal, and it is made from a periodic array of parallel conductors that reflects signals polarized parallel to the conductors, and transmits signals polarized perpendicular to the conductor axis.

A free-standing wire grid polarizer was used to minimize losses. Commercial polarizers were available with conductor spacing of 8 per mm, giving 24 conductors per wavelength (at 94 GHz, $\lambda = 3.18$ mm). This is sufficient density for low transmission and reflection losses.

A square aperture with all wires the same length is used to match the mechanical resonant frequency from wire to wire. The polarizer was fabricated with gold-plated tungsten wires. The gold plating gives lower transmission loss than bare-tungsten designs.

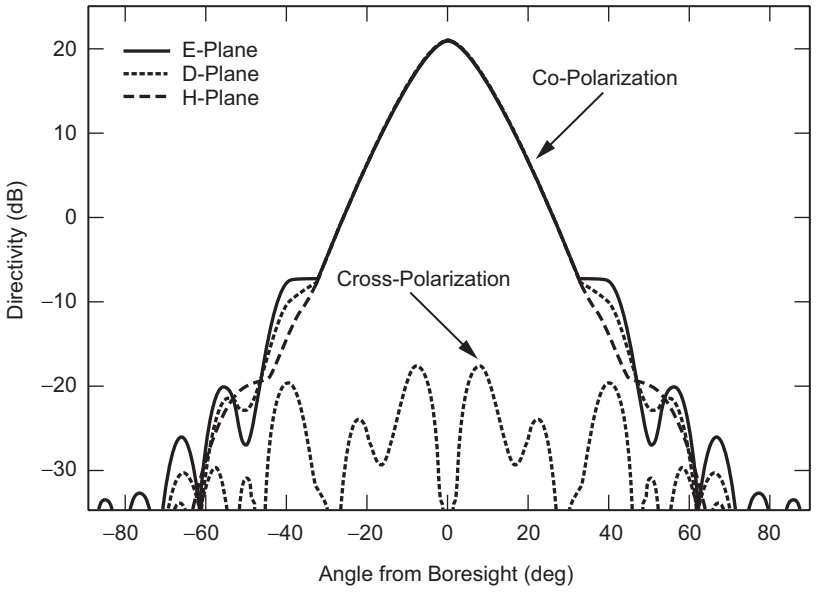

Fig. 7-25. CloudSat test horn radiation pattern, calculated on a 130-mm radius sphere centered on the phase center.

7.5.3.3 Faraday Rotator Design. The Faraday rotator (schematic shown in Fig. 7-26) consists of a ferrite disc, two quartz quarter-wave plates, and a bias permanent magnet; with axial-beam propagation. The Faraday rotation angle of a ferrite disc is given by:

$$\theta = \frac{\pi\sqrt{\varepsilon}}{c}\gamma 4\pi M_S T$$

where: γ = gyromagnetic ratio (28 GHz/T)
$4\pi M_S$ = ferrite saturation magnetization
T = Thickness

The bias field exceeds the saturation magnetization of the ferrite to provide adequate bias over the volume and minimize perturbations from external fields. The rotator is made from a 1-kilogauss (kG) permanent magnet, a rotator disc of 8.7-mm thick Transtec G-4259 ferrite, and quartz quarter-wave plates 0.406 mm thick.

7.5.3.4 Performance. The estimated losses of the QOTL are shown in Table 7-19. The radiation pattern of M4 calculated on a 130-mm radius sphere centered at the phase center is shown in Fig. 7-27.

7.5.4 Collimating Antenna

In the initial proposal for the CloudSat mission, an axially symmetric Cassegrain collimating antenna was suggested. Due to blockage by the subreflector and its supporting structure, the axially symmetric Cassegrain has inherently higher sidelobe levels and larger pattern prediction uncertainty than a clear-aperture geometry. Since in a spaceborne atmospheric radar a large

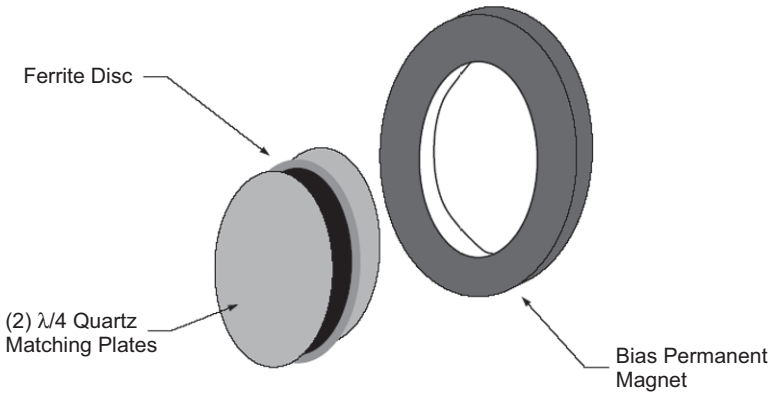

Fig. 7-26. Schematic of the CloudSat rotator design.

Table 7-19. QOTL losses.

Component	Loss, dB	Notes
Rotator ferrite	0.27	For $4\pi M_S$ = 800 gauss, ε_r = 14.8, μ_r = 38, tanϕ = 0.00015, 8.7-mm thick
Quartz plates	0.03	For ε_r = 3.79, tanϕ = 0.001, 0.41-mm thick
Mismatch	0.001	r = 0.0087
Angle error	0.03	5-deg error
Polarizer	0.2	From MLS, bare tungsten wire
Total	**0.53**	**Slightly over requirement**

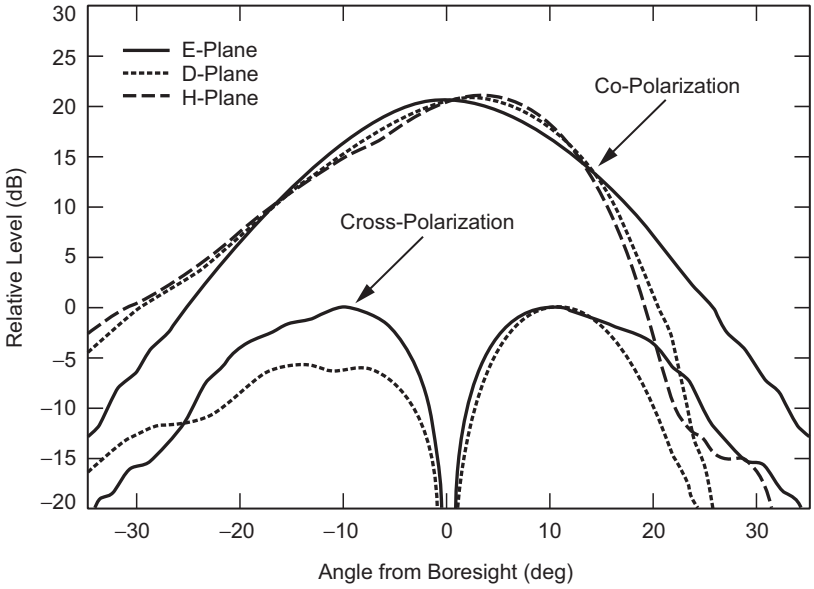

Fig. 7-27. Radiation pattern of M4, calculated on a 130-mm radius sphere centered on the phase center (EIK 1 path).

amount of Earth surface clutter comes through the antenna sidelobes, the axially symmetric Cassegrain geometry may yield intolerable sidelobe levels. To overcome this potential problem, the CloudSat designers planned on implementing a frequency diversity scheme in its digital subsystem, where a slight frequency shift would be impressed in the sequence of transmitted pulses. This would allow the cloud reflection to be separated from the surface clutter, alleviating the antenna sidelobe requirement. However, after the radar program was initiated, the use of an offset collimating antenna was proposed. The clear aperture of the offset geometry yields low sidelobes that can be accurately modeled. Due to this, the additional electronics needed to support the frequency diversity were removed.

The collimating antenna is severely constrained by the available spacecraft envelope (the translucent surface shown in Fig. 7-28), and several clear-aperture options were considered. Since there was no severe cross-polarization requirement, the highly compact open Cassegrain geometry was chosen [44]. This offset configuration, which is depicted in Figs. 7-22 and 7-28, offers excellent packaging characteristics and, although requiring a hole in mirror M1, is free of all the other blockage-related scattering problems present in an axially symmetric configuration. The M1 hole increases the radiated sidelobe levels, but the hole can be made quite small, and its scattering characteristics can be predicted with high degree of confidence. In fact, this high degree of confidence allowed the collimating antenna to be manufactured without the usual engineering and breadboard models, producing significant savings in both cost and implementation time.

The collimating antenna is depicted in the scale drawing of Fig. 7-29. The mirror M3 surface is ellipsoidal and, in the transmit mode of operation, transforms the QOTL (or test horn) pattern from about 21 dBi directivity to about 34 dBi directivity at the surface of M2. The mirror M2 is shaped to provide an almost uniform amplitude illumination of the collimating antenna aperture. M1 is also shaped to correct the phase error introduced by the shaped M2. To maximize the gain, the rim of M1 is also shaped to optimize the

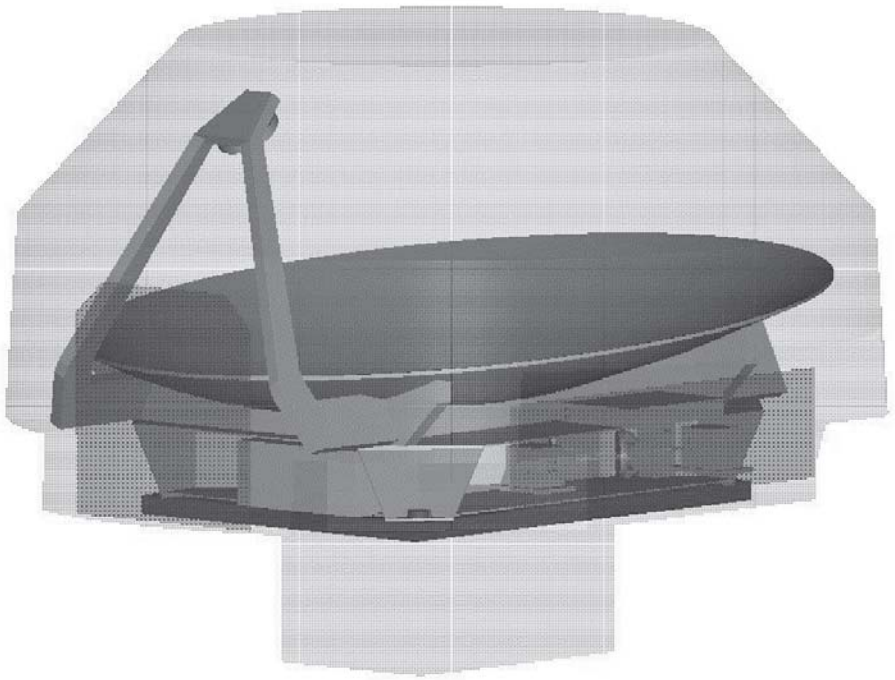

Fig. 7-28. CloudSat instrument in spacecraft envelope.

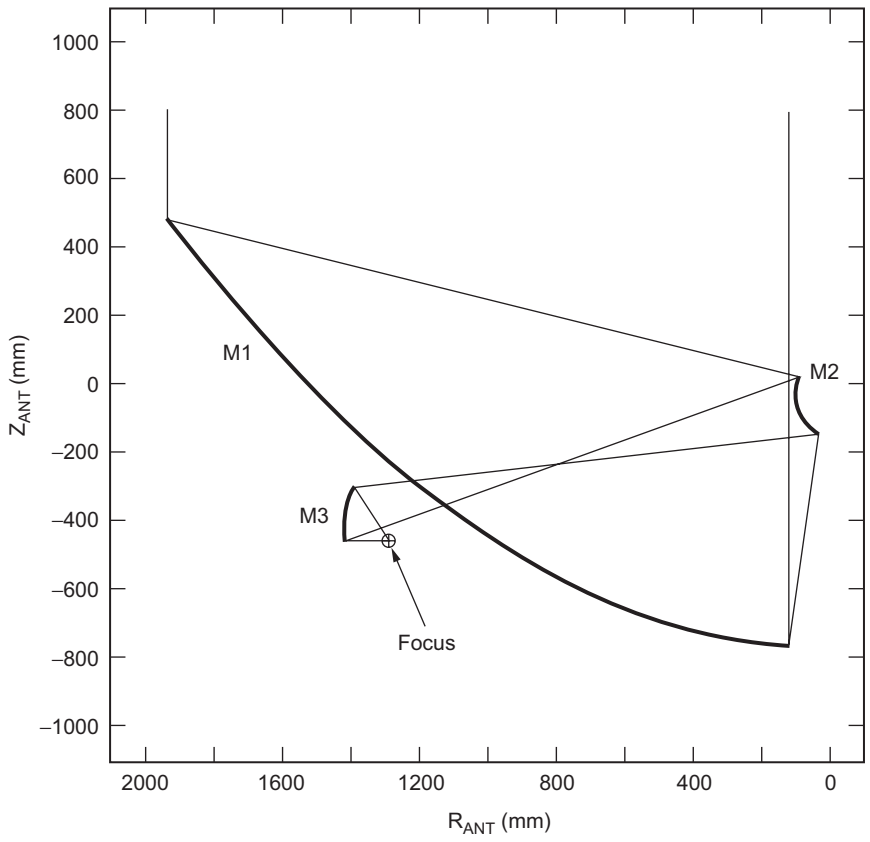

Fig. 7-29. Scale drawing of the CloudSat collimating antenna (shaped reflector system geometry in Y = 0 plane).

utilization of the available spacecraft fairing envelope (the projected M1 aperture is not circular). The end result is a projected collimating antenna aperture area of 2,798,018 mm^2, which yields a predicted 64.70 dBi directivity (85-percent efficiency since the maximum theoretical directivity of this aperture is 65.39 dBi) when excited by the test horn. This number does not include mechanical imperfections.

Due to the large asymmetry and non-circular projected rim, none of the shaping methods available in the literature (for example Section 1.2.4) can be applied to the collimating antenna; consequently, a new shaping method was developed for this antenna.

Since the surface area of M1 is much larger than the area of M2, M2 controls the amplitude of the aperture field, and M1 controls the phase of the aperture field. The shaping method developed uses numerical optimization with scattering tools to generate the shape of M2 and M1 that maximizes the

collimating antenna directivity. Since a numerical optimization is employed, arbitrary M1 and M2 rims can be used.

The numerical procedure is as follows. The radiation pattern of the test horn illuminating M3 at 94.05 GHz was determined and used as a "shaping feed'' (with an imposed spherical wavefront). The M2 surface was defined by 20 adjustable points and an interpolator based on thin-plate deformation theory [45].

These adjustable points were the optimization variables (symmetry was used to half the optimization variables). One M2 point was held fixed to establish the M2 location (nine optimization variables). The path length from the shaping feed to the aperture was held fixed and determined using geometrical optics on M2. This established the M1 shape and its position. Physical optics was used to determine the antenna directivity (on both M1 and M2). The directivity is the parameter to be maximized during the optimization process. To reduce computation time the shaping was performed at 24.05 GHz (and required ~14 hours on a 450-MHz personal computer (PC)).

As mentioned previously, the radiation of M3 reaches M2 through a hole on the surface of M1. The hole is approximately elliptical in shape and has an aperture-projected major axis of about 110 mm. This assures small scattering by the hole and allows the collimating antenna to meet the sidelobe envelope requirement with more than 10 dB margin at 7 deg from boresight. The edge tapers on M3 and M2 are 25 dB and 23 dB, respectively (space loss not included). On the hole, the M3 radiation has a 30-dB edge taper. These high edge taper values yield a total spillover loss of only 0.16 dB for the entire collimating antenna (i.e., M3 + hole + M2 + M1).

The near-boresight and far-from-boresight radiation patterns of the collimating antenna, when excited by the test horn, are depicted in Figs. 7-30 and 7-31, respectively. The electric field is polarized in the paper plane of Fig. 7-29. The near-boresight pattern was computed by sequentially using the physical optics (PO) technique starting from the test horn pattern and proceeding to M1 (the radiation of M3 through the M1 hole was modeled using the equivalence principle). Fig. 7-30 depicts the scattering of M1 and its hole, which are the only significant scattering effects in the angular range shown.

The far-from-boresight pattern of Fig. 7-31 is a composite result of two patterns that were computed using a combination of geometrical theory of diffraction (GTD) and PO scattering techniques [46]. This is needed because, for angles far from boresight, the required integration grid over M1 is very dense; and hence, the computation time to determine the radiation pattern becomes prohibitively large. The first pattern of the composite was the radiation of M1 and its hole. It was obtained by first computing the radiation over M2, emanating from the M1 hole, as described for the near-boresight pattern. This pattern was then used to excite M2, and its scattering over M1

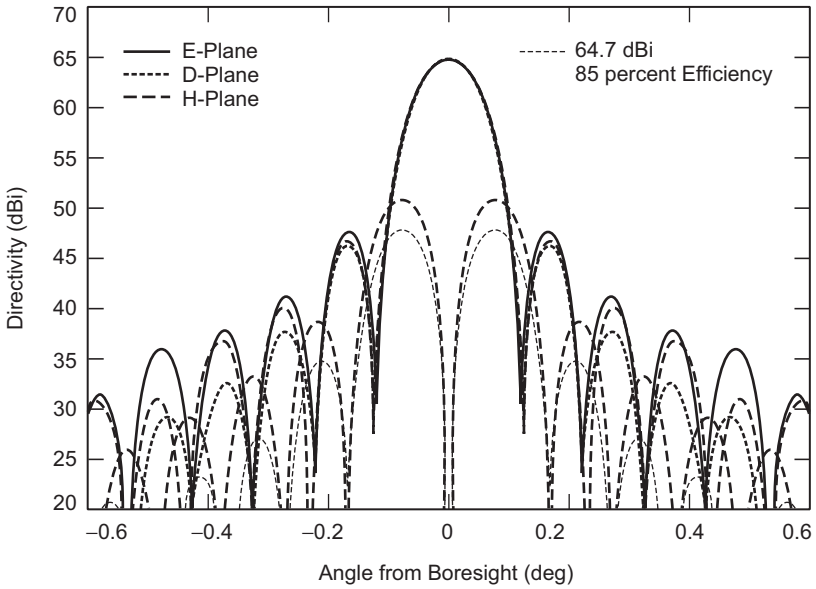

Fig. 7-30. CloudSat collimating antenna calculated near-boresight far-zone radiation pattern (excited by the test horn).

determined using GTD. The radiation from M1 and its hole was then determined using PO and plotted in Fig. 7-31. The second pattern of the composite is the M2 scattering and its spillover. It was determined as described for the near-boresight pattern and also plotted in Fig. 7-31. This composite pattern then shows, as an envelope, the dominant pattern of the two parts of the composite. Clearly seen in Fig. 7-31 is the effect of the M1 hole (oscillations that peak at about every 2 deg, and can be seen between approximately –30 and +30 deg), the M2 spillover (in the neighborhood of –70 deg), and the M1 top-rim spillover (beyond about +65 deg). Although the shaped rim increases the sidelobes, the –50 dB sidelobe envelope requirement (relative to peak gain) for angles greater than 7 deg is met with ~12 dB of margin (worst case). Since the edge of the Earth is at about 65 deg from nadir, the M1 and M2 spillovers do not significantly contribute to clutter.

The mirror M1 and its associated support structure was manufactured using composite materials to reduce weight while yielding an rms surface accuracy better than 50 μm.

The surface of M1 was coated with a vacuum-deposited aluminum film to provide a highly reflective surface at W-band. The mirror M2 was machined in aluminum to an accuracy better than 25 μm. Both the M1 and M2 surfaces were subsequently made Lambertian to reduce coherent scattering at infrared wavelengths, and hence minimize thermal loading. All other mirror surfaces

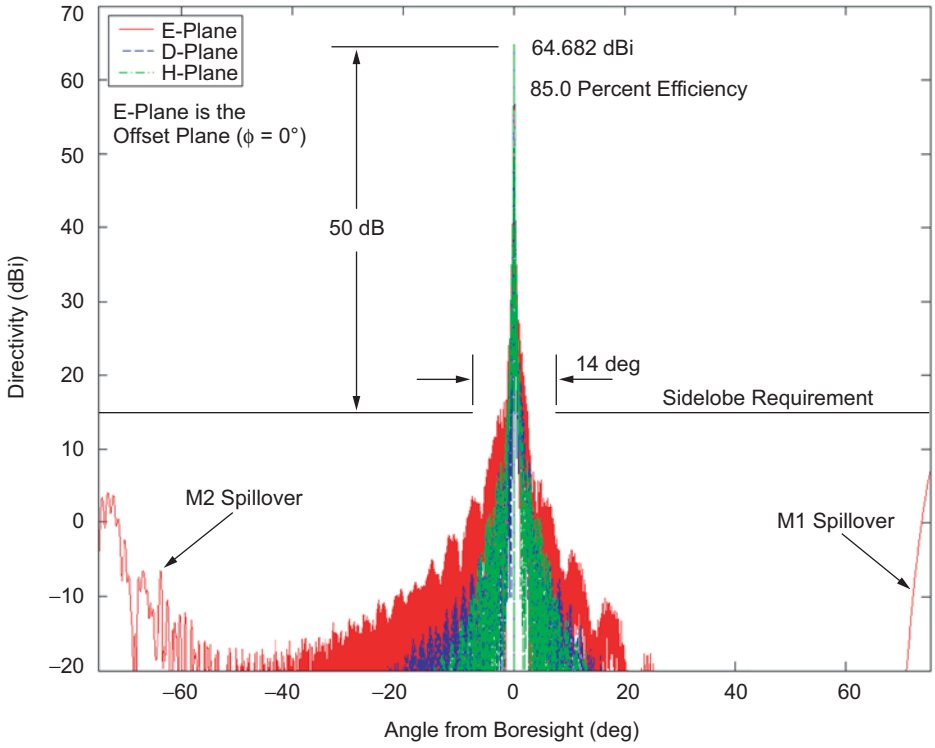

Fig. 7-31. CloudSat collimating antenna far-from-boresight radiation pattern (excited by the test horn).

(i.e., M3–M6) were machined of aluminum to an accuracy significantly better than that of M1 and M2.

Table 7-20 summarizes the expected performance of the CPR antenna system, and provides a breakdown of its various loss components. As mentioned previously, the QOTL paths for the EIK 2 and the receiver have the worst performance with an overall gain of 63.1 dBi. The EIK 1 path has a better performance with a gain of 63.2 dBi. These numbers correspond to overall efficiencies for the CPR antenna system of 59.0 percent and 60.5 percent, respectively.

7.5.5 Measured Performance

The gain, sidelobes, and pointing were measured on both the near-field range and a quasi-far-field range at JPL. Measurements were also made before and after the vibration test. The results were:

1) Gain met specification, with close to promised uncertainty.

Table 7-20. Gain loss budget for the CPR antenna system.

Loss/Gain Path Elements	EIK 1 (dB)	EIK 2 (dB)	RCVR (dB)
Collimating antenna directivity	64.70	64.70	64.70
Primary – mirror M1			
Reflectivity	–0.04	–0.04	–0.04
Surface error	–0.10	–0.10	–0.10
Secondary – mirror M2			
Reflectivity	–0.012	–0.012	–0.012
Surface error	–0.05	–0.05	–0.05
Tertiary – mirror M3			
Reflectivity	–0.02	–0.02	–0.02
Surface error	–0.012	–0.012	–0.012
QOTL to collimating antenna coupling	–0.25	–0.45	–0.45
QOTL mirror M4			
Spillover	–0.05	–0.03	–0.03
Reflectivity	–0.02	–0.02	–0.02
Surface error	–0.012	–0.012	–0.012
Faraday rotator			
Ferrite dielectric loss	–0.26	–0.26	–0.26
Matching plates	–0.03	–0.03	–0.03
Reflectivity	0.00	0.00	0.00
Angular error	–0.03	–0.03	–0.03
Duplexing polarizer	–0.20	–0.20	–0.20
QOTL mirror M5			
Spillover			–0.11
Reflectivity			–0.02
Surface error			–0.012
QOTL mirror M6			
Spillover	–0.11	–0.11	
Reflectivity	–0.02	–0.02	
Surface error	–0.012	–0.012	
Feed horn waveguide flange pair	–0.10	–0.10	–0.10
Feed horn and waveguide losses	–0.12	–0.12	–0.12
Total overall gain (dBi)	**63.2**	**63.1**	**63.1**

2) Pre-post vibration gain differences well within uncertainty, and pattern shapes tracked well.
3) Patterns had some sidelobe discrepancies.
4) On elevation and azimuth cuts, sidelobe levels were exceeded.
5) Outermost sidelobe specification met (>7 deg).

6) Pre-post vibration change in pointing within uncertainty. Pointing uncertainty somewhat larger than anticipated.
7) Beam co-pointing within specification (±0.01 deg)

7.6 Wide Swath Ocean Altimeter

Richard E. Hodges

The Ocean Surface Topography Mission (OSTM) [47] is a cooperative effort between NASA, the National Oceanic and Atmospheric Administration (NOAA), the European organization for the Exploitation of Meteorological Satellites (EUMETSAT), and the Centre National d'Etudes Spatiales (CNES), the space agency of France. OSTM is a follow-on to Jason [48] and will provide continuity of ocean topography measurements beyond Jason and TOPEX/Poseidon [49]. OSTM will measure sea surface height to an accuracy of <4 cm every 10 days. Sea surface topography, as measured by satellite altimeters, has numerous applications important to global environmental monitoring, including predicting hurricane intensification, improving tide models, mapping deep-ocean bathymetry, monitoring, and forecasting El Niño Southern Oscillation, measuring the rate of global sea-level rise, and charting surface currents.

OSTM will carry six scientific instruments. NASA will provide the advanced microwave radiometer (AMR), the global positioning system payload (GPSP), the laser retroreflector array (LRA), and the experimental wide swath ocean altimeter (WSOA). CNES will provide the nadir altimeter and the Doppler orbitography and radio positioning integrated by satellite (DORIS) instruments. The nadir altimeter will provide vertical measurements of sea-surface height. The AMR will provide atmospheric correction for the nadir altimeter. The GPS payload, the LRA, and the DORIS will provide precision orbit determination, and the WSOA will demonstrate new high-resolution measurement of ocean surface topography. The following describes the development of the WSOA.

WSOA is a cross-track interferometer with a 6.4-m baseline. WSOA will produce a full three-dimensional map of ocean height, which will provide key information on oceanic energy transport and eddy currents.

An enabling technology for this instrument is the pair of antennas used to form the Ku-band interferometer operating at 13.285 GHz. WSOA requires two 2.2- by 0.35-m projected apertures that are stowed by folding and that provide dual-beam, dual-polarization, ~20-dB sidelobes, and 50-percent aperture efficiency in a low mass package. A unique offset-fed reflectarray antenna design was developed to meet these needs and also minimize overall system mass and moment of inertia. Each antenna has two feeds located off the focal point to produce two beams scanned ±3.3 deg from nadir.

Each antenna is comprised of a reflectarray and two slotted waveguide feeds. A reflectarray is a relatively new type of antenna that uses non-Snell's law reflection optics to enable a flat surface to function as a focused reflector comparable to a traditional parabolic reflector [50–52]. The reflectarray is realized using a uniform array grid of variable-sized microstrip patch elements. These elements are designed to reflect an incident field with the phase shift needed to collimate a beam. An important discovery in this work is that a flat offset-fed reflectarray provides dramatically better scan performance than a comparable reflector antenna. Indeed, for this application a parabolic reflector antenna is not viable because the scan loss from positioning the feeds off-focus to obtain ±3.3 deg beam positions is ~3 dB.

An experimental breadboard of the reflectarray was built and successfully demonstrated that the performance requirements can be achieved using this new technology. The reflectarray antennas are made up of five separate flat panels, which can be folded for compact stowage and ease of deployment. The panels consist of an aluminum honeycomb core and a thin dielectric substrate upon which the square patch elements are etched. The slotted waveguide feeds utilize Taylor amplitude weighting to achieve low spillover. Since the reflectarray surface is in the near field of the feeds, a cylindrical phase taper is used on the feed aperture to focus the feed pattern at the 2.8-m reflectarray focal distance.

7.6.1 Antenna Requirements

WSOA is a cross-track interferometer that requires a pair of dual-polarized antennas separated by a 6.4-m baseline as illustrated in Fig. 7-32. The key antenna electrical requirements are summarized in Table 7-21. A projected aperture size of approximately 2 m × 0.35 m is needed to achieve the gain and beamwidth requirements.

To obtain a 39.2-dB gain with this aperture, the antenna must realize an overall efficiency of approximately 50 percent. To accommodate the length and baseline separation of these apertures, the antennas must fold up for launch stowage and be compatible with a mast deployment mechanism. Spacecraft mass allocation, moment of inertia, and center of gravity lead to requirements for very low mass (<14 kg).

Several options (including a reflector, a microstrip patch array, and a waveguide array) were considered for the WSOA. A reflectarray design was selected because it is the only option that meets all of the requirements. For example, a reflector antenna cannot fold flat for stowage and does not meet requirements for two beams in the offset configuration. A microstrip patch array and waveguide array could not meet the mass requirements. The key drawback of the reflectarray design option is lack of flight heritage—to date, a reflectarray has not been flown on a space flight mission.

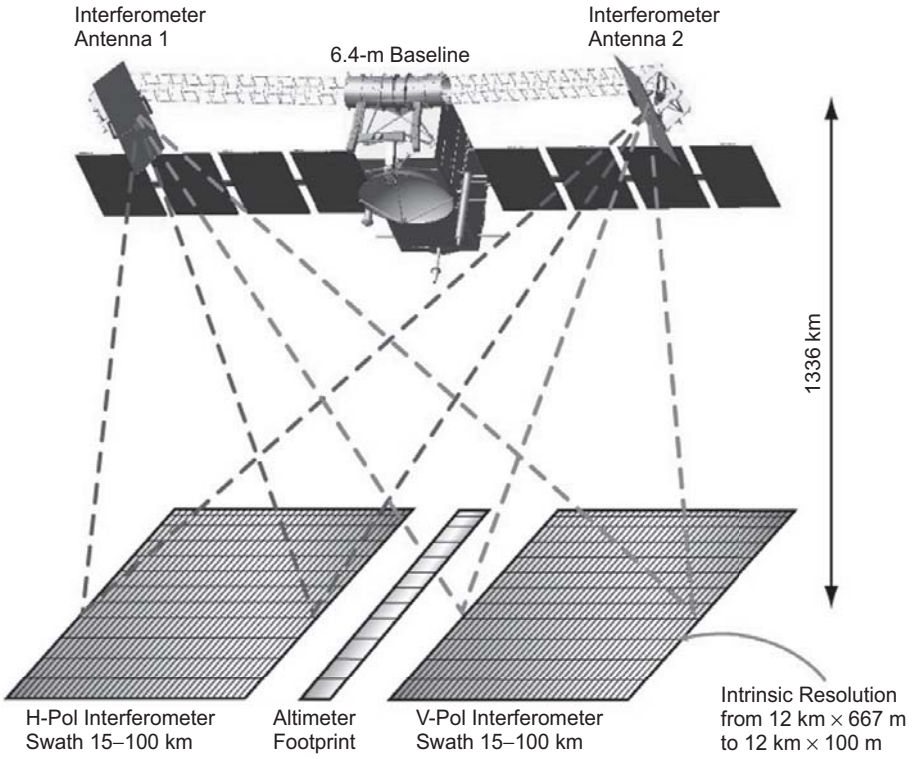

Fig. 7-32. WSOA system concept.

Table 7-21. WSOA antenna requirements.

Parameter	Value
Center frequency	13.285 GHz
Bandwidth	20 MHz
Gain per antenna	≥39.2 dBi
Elevation 3-dB beamwidth	≥3.8 deg
Azimuth 3-dB beamwidth	<0.65 deg
Beam pointing (V-polarization/H-polarization)	±3.3 deg
Sidelobe ratio (elevation)	–13 dB
Sidelobe ratio (azimuth)	–20 dB
Cross polarization	–20 dB
Return loss	>20 dB
Peak power handling	130 W
Panel mass (10 panels)	11.26 kg
Feed mass (4 feeds)	2.5 kg

Two concepts were developed to meet the system requirements. The initial concept was a symmetric-fed antenna design [53]. Although this design was proven in breadboard testing, the placement of electronics and cabling could not meet system requirements. To overcome this problem, a novel offset-fed reflectarray design was developed. Although this design significantly increased the technical risk, the design software developed for the symmetric design enabled rapid development of the offset-fed design.

Figure 7-33 illustrates the offset-fed reflectarray antenna design developed for the WSOA interferometer [54,55]. The offset-fed design improves spacecraft antenna accommodation by arranging the reflectarray optics to locate the focal point near the spacecraft bus. The focal length is 2.8 m, and the two feeds are offset from the focal point in order to realize a ±3.3-deg elevation beam scan (Fig. 7-34). This feed placement allows all transmitter and receiver electronics to be co-located on the spacecraft bus, which eliminates the need for separated electronics boxes and associated cables to distribute RF, power, and control signals along the mast. If the reflectarray panels are sufficiently low mass, this results in reduced mass and moment of inertia. In addition, the flexibility to reposition the panels enables a designer to adjust instrument center of gravity.

7.6.2 Panel Design

Each reflectarray is comprised of five panels and a two feeds, one feed for vertical polarization and one for horizontal polarization. A mechanical deployment mechanism is used to fold the flat panels into a stowage

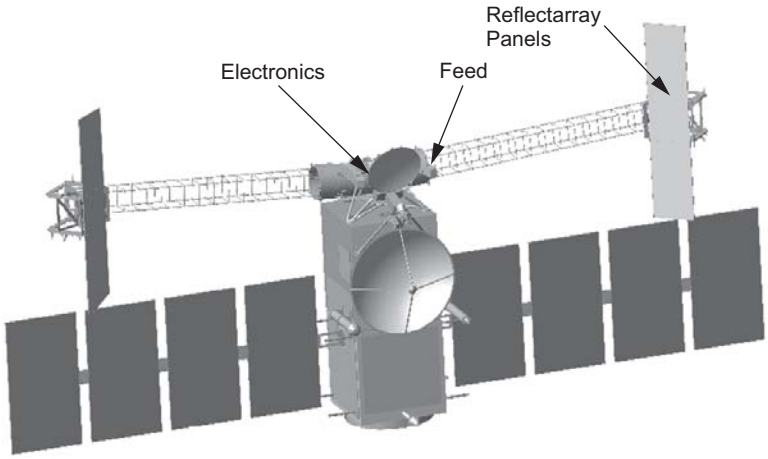

Fig. 7-33. Illustration of WSOA offset-fed reflectarray antennas spacecraft accommodation.

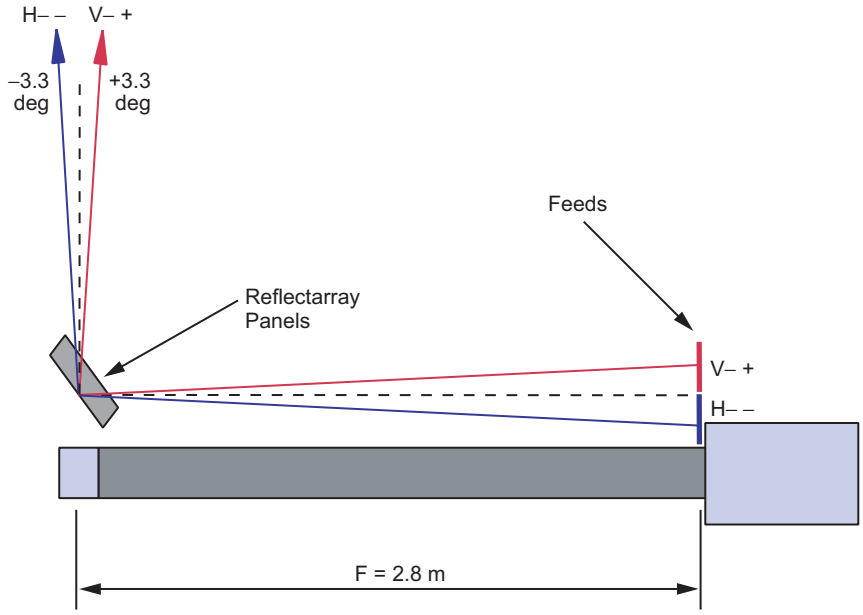

Fig. 7-34. WSOA offset-fed feed scanning arrangement.

configuration for launch. The panels use variable-sized square patch reflectarray elements printed on dielectric substrates. Unlike in the symmetric configuration [53], a piecewise parabolic configuration will not work for the offset-fed reflectarray because excessive scan loss precludes the ±3.3-deg elevation beam scan. Fortunately, it was found that a flat reflectarray geometry yields acceptable scan loss, and therefore, enables one to obtain the required ±3.3-deg elevation beam scan.

Pozar's variable patch design procedure was used for the reflectarray electrical design [52]. The procedure uses infinite array (Floquet mode) reflection coefficients to determine the phase of the field scattered by each patch. This approximation introduced risk because reflectarray element sizes vary over the array face, thus creating a non-periodic array environment. Since patch elements can only generate ~360-deg phase shift, "phase wraps" occur when the required phase shift exceeds this value.

7.6.3 Feed Design

A waveguide slot array was selected as the feed design for an appropriate combination of high efficiency, relatively low mass, higher power-handling capability, and an ability to control the pattern shape by adjusting the amplitude and phase coefficients at each radiating slot. It also provided a simple geometry that could be easily modeled with basic array theory in the calculation of the secondary reflectarray pattern.

The interferometric baseline and availability of space on the flight vehicle set the geometry shown in Fig. 7-35. Basic system requirements specified the scan angle and beamwidth for both the azimuth and elevation directions. The design task was to provide an illumination on the reflectarray to satisfy these requirements.

A Taylor distribution was used to determine the slot amplitudes in both the azimuth and elevation directions, while a cylindrical phase taper was used to focus the beam at the center of the reflectarray to minimize spillover. An iterative approach was then used to vary the feed position and amplitude weighting on the slots to achieve the required scan angles and beamwidths. Simple array theory was used for each iteration to calculate the resulting field at each patch element for use in calculation of the secondary reflectarray pattern.

Once the correct patterns were established, then the waveguide feed network that fed the slots could be designed by combining various waveguide components (such as T-splitters and couplers) to transfer power between different waveguide layers in the feed. Four unique feed designs are needed for WSOA—two V-pol and two H-pol. One feed of each polarization is described below. The other two feeds use the same basic design, but the number of rows is varied to adjust the beamwidth needed to obtain the desired reflectarray illumination.

7.6.3.1 Vertical-Polarization Feed. The geometry selected for the radiating slot layer of the vertical-polarization (V-pol) feed is an offset longitudinal-shunt

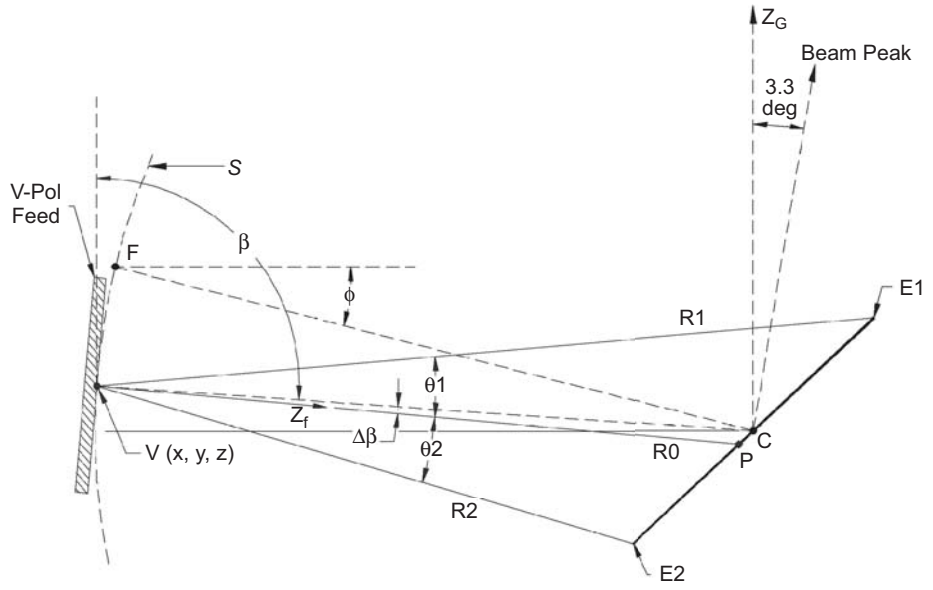

Fig. 7-35. WSOA basic geometry and design parameters (not to scale).

slot array. There are a total of eighteen three-by-one subarrays. A full-wave moment method procedure was used to design the required slot offsets, and the calculated patterns showed excellent agreement with those from array theory. An 18-way power divider with the appropriate power splits and phase delays provides the correct input excitation to each subarray.

The final breadboard configuration consists of four machined aluminum layers, with couplers transferring the power between the layers. Silver paint is used to provide electrical contact between the layers for breadboard testing. The flight hardware will use dip-brazed aluminum fabrication to minimize mass and ensure consistent electrical contact between all parts.

The performance of the assembled feed was excellent. The input return loss was 24 dB, which met the specification of 20 dB. The measured patterns, shown in Fig. 7-36, also agreed very well with those calculated by the moment method. Note that the elevation patterns are de-focussed in the far-field but are properly focused in the near feed at a radius of 2.8 m due to the cylindrical phase aperture illumination. The measured gain of 24.1 dB was also in good agreement with the calculated gain of 24.2 dB. The silver-painted breadboard feed achieved an efficiency of 87 percent.

7.6.3.2 Horizontal Polarization Feed. A design procedure similar to V-pol was followed for the horizontal-polarization (H-pol) feed. The feed geometry selected for the H-pol feed is a 4 × 16 element array comprised of eight 4 × 2 subarrays. Each 4 × 2 subarray consists of four 1 × 2 longitudinal-shunt slot subarrays. The eight 4 × 2 subarrays are fed from another layer consisting of eight rows of series-shunt angled coupling slots–four slots per row. An eight-way power divider on a third layer provides the correct amplitude and phase taper to each of the eight angled coupling slot rows.

The final H-pol configuration consists of four machined aluminum layers, with couplers transferring the power between the layers. The resulting patterns are shown in Fig. 7-37. The measured gain of 24.8 dB agreed very well with the calculated gain of 24.9 dB. The return loss was 17 dB at the design frequency but was 23 dB about 0.1 GHz higher, which can be tuned in a future iteration.

7.6.4 Breadboard Test Results

A breadboard model of the offset-fed antenna was designed, built, and tested to verify the accuracy of the modeling capability. Figure 7-38 shows the breadboard test antenna mounted in the NASA/JPL cylindrical near-field test facility. The panels and feeds are supported by a rigid aluminum frame structure to maintain the proper geometrical orientation of the panels relative to the feeds. The frame is covered with absorber material to eliminate spurious scattering lobes in the antenna pattern.

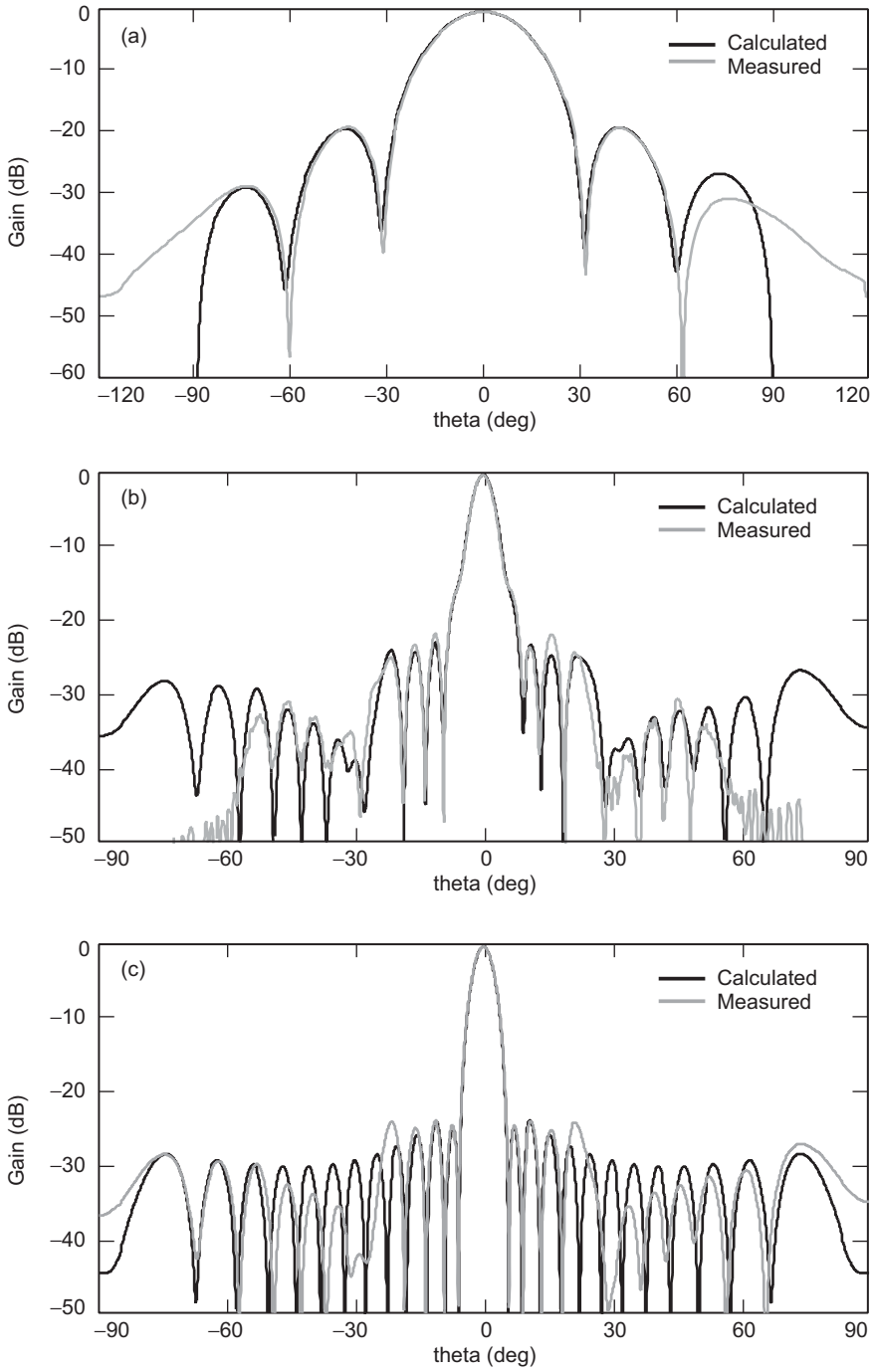

Fig. 7-36. WSOA measured vs. calculated feed patterns with V-polarization: (a) azimuth, (b) far-field elevation, and (c) near-field elevation.

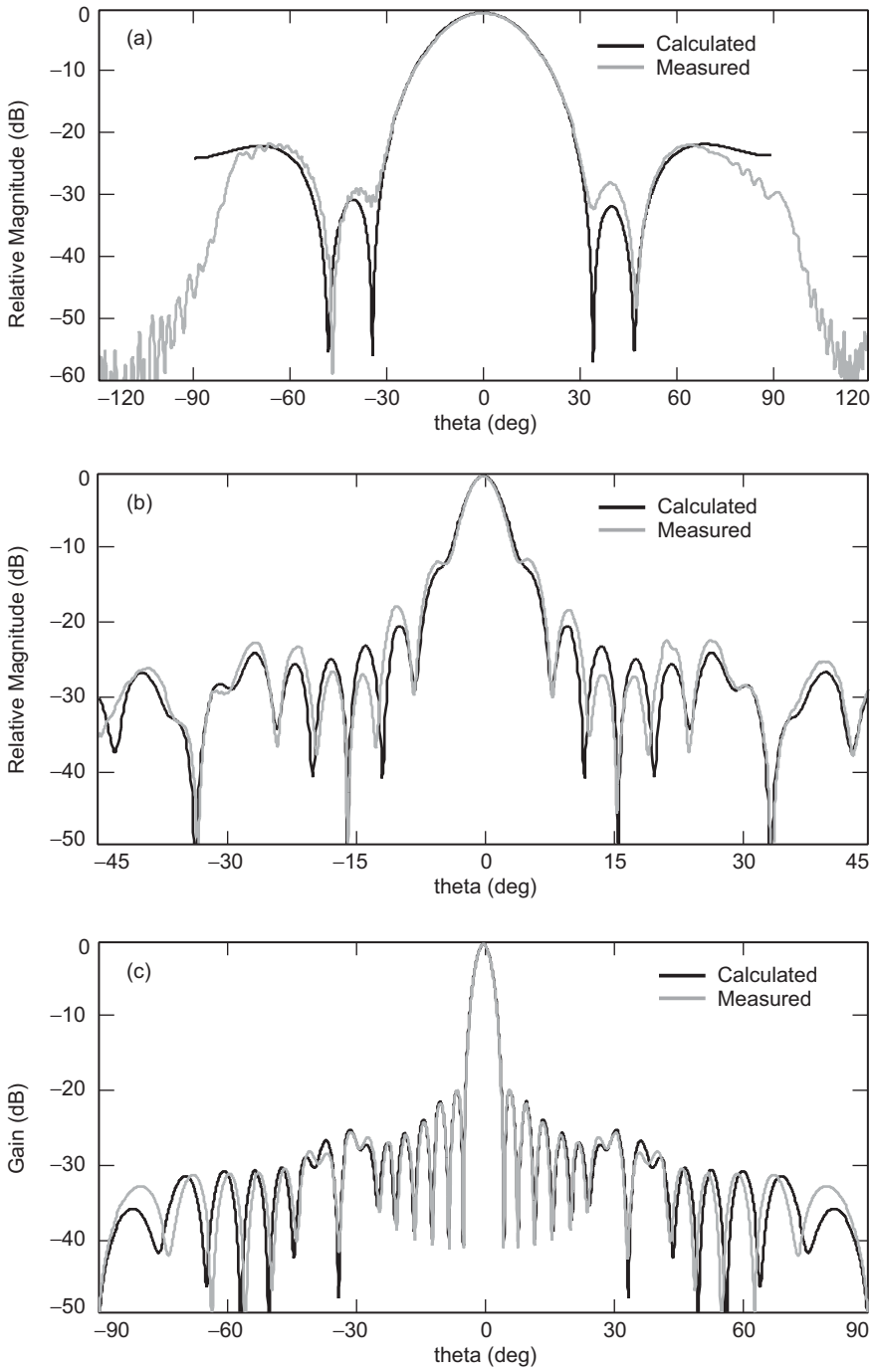

Fig. 7-37. WSOA measured vs. calculated feed patterns with H-polarization: (a) azimuth, (b) far-field elevation, and (c) near-field elevation.

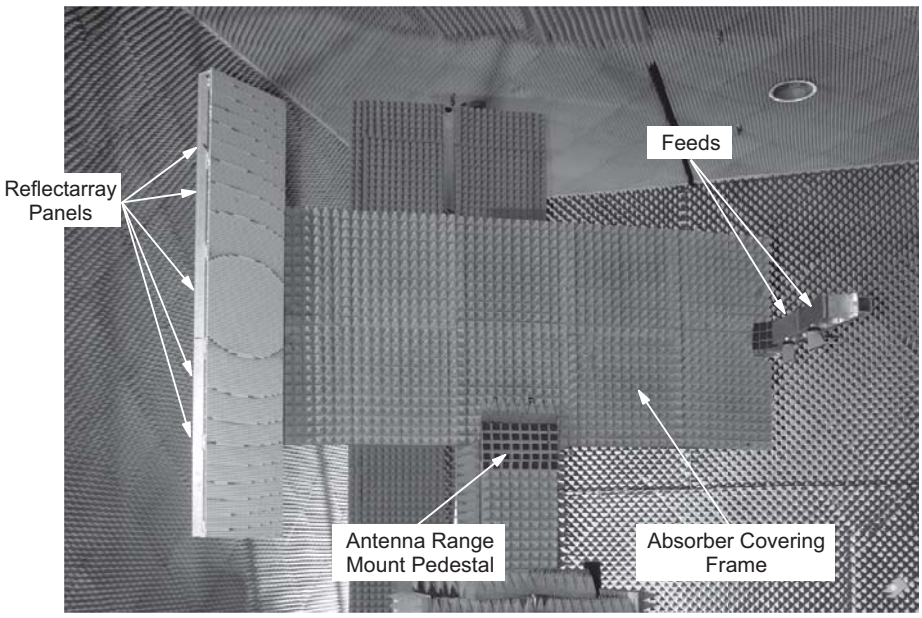

Fig. 7-38. WSOA offset-fed reflectarray breadboard mounted in NASA JPL cylindrical near-field test facility.

Figures 7-39 and 7-40 compare measured and calculated antenna patterns using the V-pol feed of the breadboard antenna. The patterns for H-pol are similar. The data show excellent agreement with predicted patterns. It should be noted that predicted patterns are calculated entirely from theoretical models, and do not account for errors in surface flatness or feed misalignment which were measured by a laser metrology system. The results tabulated in Tables 7-22 and 7-23 demonstrate good agreement between predicted and measured performance, and more importantly show that the specifications in Table 7-21 can be achieved. Note that the projected aperture is 2.2×0.35 m, so that the measured aperture efficiency is 48 percent for V-pol and 51 percent for H-pol. Efficiency is expected to improve slightly with flight-model feeds that are brazed instead of silver painted.

7.6.5 Conclusions

A reflectarray antenna offers a unique combination of advantages that can be a mission-enabling antenna design concept. The key characteristics of a properly designed reflectarray include relatively simple to obtain dual polarization, improved scan capability, low mass, good launch stowage, good efficiency (~50 percent), and relatively low cost.

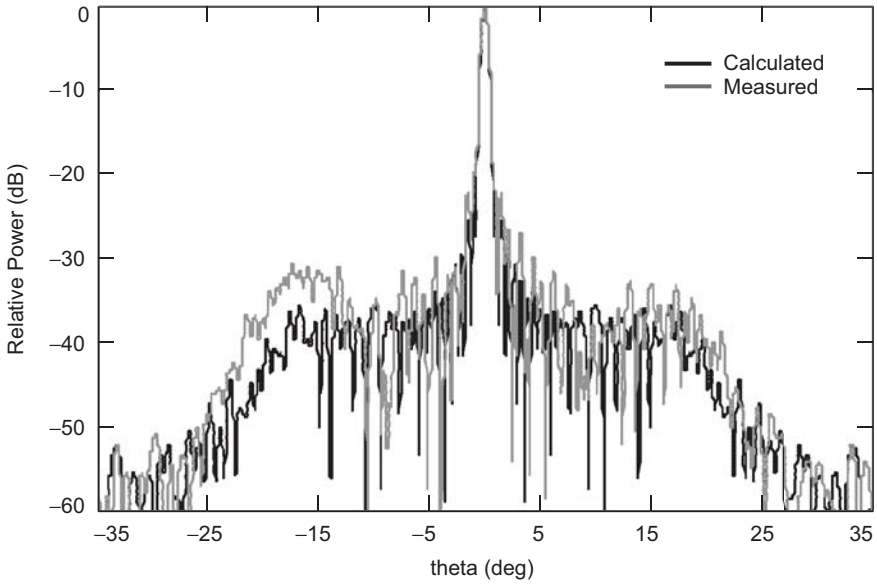

Fig. 7-39. Comparison of WSOA measured vs. calculated breadboard offset-fed reflectarray antenna patterns (V-pol azimuth).

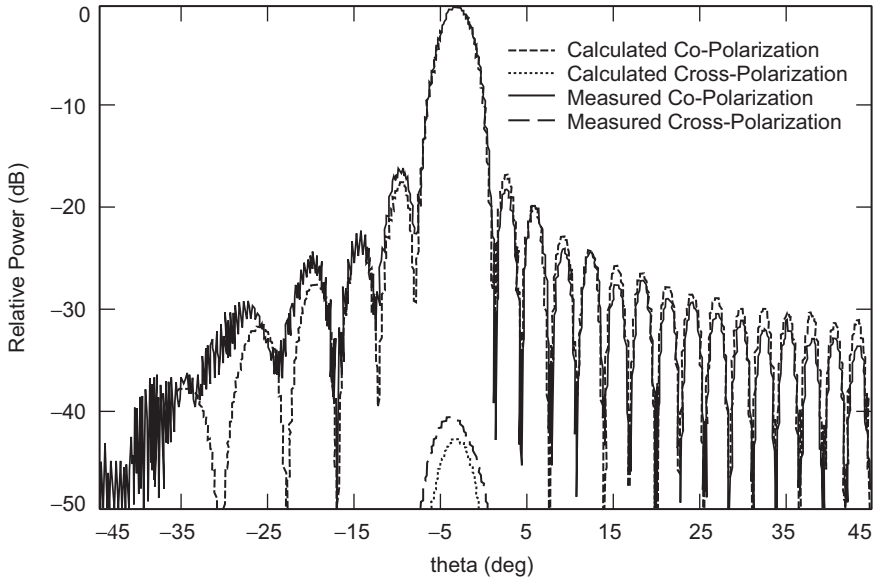

Fig. 7-40. Comparison of WSOA measured vs. calculated breadboard offset-fed reflectarray antenna patterns (V-pol elevation).

Table 7-22. V-pol reflectarray performance summary.

	Predicted	Measured
Gain	39.81 dB	39.31 dB
El beamwidth	3.85 deg	3.88 deg
Az beamwidth	0.625 deg	0.626 deg
El sidelobes (max)	–18.0 dB	–16.9 dB
Az sidelobe (max)	–21.90 dB	–19.5 dB

Table 7-23. H-pol reflectarray performance summary.

	Predicted	Measured
Gain	40.15 dB	39.53 dB
El beamwidth	3.84 deg	3.93 deg
Az beamwidth	0.616 deg	0.630 deg
El sidelobes (max)	–21.7 dB	–21.3 dB
Az sidelobe (max)	–21.5 dB	–18.7 dB

Compared to a reflector antenna, the reflectarray has smaller frequency bandwidth [56,57] and lower aperture efficiency. However, reflectarray fabrication is lower cost because it uses standard planar printed circuit fabrication techniques and does not require precision molds and custom lay up processes needed to produce lightweight composite reflectors.

7.7 Summary

Richard E. Cofield

In conclusion, JPL's development of radiometer and scatterometer antennas for instrument packages has combined an extensive heritage of theory and experience from JPL's telecommunications antenna programs, with the rigorous and ambitious regimens for qualifying spaceborne observational instruments. The following points distinguish these instruments' antennas from their ground-based predecessors.

Antenna performance requirements for scatterometers and radiometers generally differ slightly from those for telecommunications antennas. Radiometers typically view extended sources, especially in Earth remote-sensing applications. Therefore, requirements are often set for beam efficiency, rather than gain. Moreover, the atmospheric sounders can tolerate substantial cross-polarized power, as long as it is accurately known. In contrast, scatterometers typically have stringent gain and polarization isolation requirements but less demanding requirements on sidelobe level.

An important part of the development of spaceborne instrument antennas is pattern (or FOV) calibration. With the environment and observation scene often very different in space than during ground calibration, the analysis of flight data often requires the antenna performance knowledge as a mixture of measured patterns plus estimates of far-angle scattered power envelope. In many cases this demands an in-flight calibration campaign, using ground calibration sources (active or passive), known properties of homogeneous scenes for ground truth, or celestial objects (Sun, Moon, etc.) for in-orbit verification of the antenna pattern shape or its pointing.

Signals for radiometry in current instruments lie increasingly in submillimeter bands between windows for optical and telecommunications applications. With the need to fly as few receivers as possible, this drives us to broader bandwidths rather than for antennas in the other applications.

The expense of launch and the difficulty of instrument retrieval continue to make it critical to verify performance requirements through environmental tests, and to understand interactions between instrument and spacecraft. For antennas, this makes the following crucial:

1) FOV calibration must be properly sequenced with environmental qualification (such as vibration and thermal vacuum tests). The engineer must demonstrate with ever-increasing clarity how the antenna meets requirements before, during, and after these tests.
2) Alignment of the antenna boresight to spacecraft reference combines optomechanical methods with RF patterns. For extreme orbital environments these results must be interpreted using thermal and mechanical models of the spacecraft in flight, augmented where possible with temperature or dynamic-telemetry data. Alignment instruments packaged for hostile environments promise to help in this interpretation.
3) Analysis of flight data depends on both placement and knowledge of the alignment of co-aligned multiple sensors. Until now, this has been successful on a single platform, but future missions call for formation flying, which will increase the difficulty of co-alignment.

We expect that the synergy between spaceborne instrument antennas and their ground-based and telecommunications counterparts will continue to benefit both programs as JPL continues developing space missions.

References

[1] D. Staelin, P. W. Rosenkranz, F. T. Barath, E. J. Johnson, J. W. Waters, “Microwave Spectroscopy Imagery of the Earth,” *Science*, vol. 197, no. 4307, pp. 991–993, 1977.

[2] P. Swanson, W. Harris, and E. Johnston, "The Tiros-N Microwave Sounder Unit," *1980 MTT-S International Microwave Symposium Digest*, vol. 80, no. 1, pp. 123–125, 1980.

[3] M. J. Schwartz, W. V. Snyder, and W. G. Read, *EOS MLS Mesosphere-Specific Forward Model Algorithm Theoretical Basis Document*, JPL D-28534 (internal document), version 1, Jet Propulsion Laboratory, Pasadena, California, also available on line, June 4, 2004, accessed September 15, 2005. http://mls.jpl.nasa.gov

[4] P. Goldsmith and R. Kot, "Microwave Radiometer Blackbody Calibration Standard for Use at Millimeter Wavelengths," *Review of Scientific Instruments*, American Institute of Physics, vol. 50, no. 9, pp. 1120–1122, September 1979.

[5] P. Gloersen and F. Barath, "A Scanning Multichannel Microwave Radiometer for Nimbus-G and Seasat-A," *IEEE Journal of Oceanic Engineering*, vol. 2, no. 2, pp. 172–178, 1977.

[6] E. Njoku, J. Stacey, and F. Barath, "The Seasat Scanning Multichannel Microwave Radiometer (SMMR): Instrument Description and Performance," *IEEE Journal of Oceanic Engineering*, vol. 5, no. 2, pp. 100–115, 1980.

[7] K. Green, *Final Report on Design Study of NIMBUS-G SMMR Antenna Subsystem*, Technical Report, Microwave Research Corporation, North Andover, Massachusetts, 1975.

[8] E. Njoku, E. Christensen, and R. Cofield, "The Seasat Scanning Multichannel Microwave Radiometer (SMMR): Antenna Pattern Corrections Development and Implementation," *IEEE Journal of Oceanic Engineering*, vol. 5, no. 2, pp. 125–137, 1980.

[9] C. Ruf, S. Keihm, and M. Janssen, "TOPEX/Poseidon Microwave Radiometer (TMR). I. Instrument Description and Antenna Temperature Calibration," *IEEE Transactions on Geoscience and Remote Sensing*, vol. 33, no. 1, pp. 125–137, 1995.

[10] M. Janssen, C. Ruf, and S. Keihm, "TOPEX/Poseidon Microwave Radiometer (TMR). II. Antenna Pattern Correction and Brightness Temperature Algorithm," *IEEE Transactions on Geoscience and Remote Sensing*, vol. 33, no. 1, pp. 138–146, 1995.

[11] C. Ruf, S. Keihm, and B. Subramanya, "TOPEX Microwave Radiometer in-Flight Performance Evaluation," *International Geosciences and Remote Sensing Symposium*, (IGARSS) 1993, pp. 1759–1761, 1993.

[12] F. Soltis and S. Kaki, *Jason-1 Project Microwave Radiometer Functional Requirements*, JPL D-14917 (internal report), Jet Propulsion Laboratory, Pasadena, California, October 1997.

[13] C. L. Kahn, "Challenges in Developing the Microwave Instrument for the Rosetta Orbiter," *IEEE Aerospace Conference Proceedings*, vol. 2, pp. 2-575–2-582, 2002.

[14] V. Jamnejad, "A Dual Band Telescope for Microwave Instrument on Rosetta Orbiter (MIRO)," *IEEE Aerospace Conference Proceedings*, vol. 3, pp. 3-265–3-269, 1999.

[15] J. W. Waters, "Microwave Limb Sounding," *Atmospheric Remote Sensing by Microwave Radiometry*, M. A. Janssen, editor, chapter 8, John Wiley, New York, New York, 1993.

[16] N. Livesey, W. G. Read, L. Froidevaux, J. W. Waters, M. L. Santee, H. C. Pumphrey, D. L. Wu, Z. Shippony, R. F. Jarnot, "The UARS Microwave Limb Sounder Version 5 Data Set: Theory, Characterization, Validation," *Journal of Geophysical Research*, vol. 108, no. D13, article no. 4378, pp. ACH 2-1–ACH 2-21, 2003.

[17] R. F. Jarnot, R. E. Cofield, J. W. Waters, D. A. Flower, and G. E. Peckham, "Calibration of the Microwave Limb Sounder on the Upper Atmosphere Research Satellite," *Journal of Geophysical Research*, vol. 101, no. D6, pp. 9957–9982, April 1996.

[18] F. T. Barath, M. C. Chavez, R. E. Cofield, D. A. Flower, M. A. Frerking, M. B. Gram, W. M. Harris, J. R. Holden, R. F. Jarnot, W. G. Kloezeman, G. J. Klose, G. K. Lau, M. S. Loo, B. J. Maddison, R. J. Mattauch, R. P. McKinney, G. E. Peckham, H.M. Pickett, G. Siebes, F. S. Soltis, R. A. Suttie, J. A. Tarsala, J. W. Waters, and W. J. Wilson, "The Upper Atmosphere Research Satellite Microwave Limb Sounder Instrument," *Journal of Geophysical Research*, vol. 98, no. D6, pp. 10751–10762, June 20, 1993.

[19] R. F. Jarnot and R. E. Cofield, *Microwave Limb Sounder (MLS) Instrument Calibration Report*, JPL. D-9393, version 1.0 (internal document), Jet Propulsion Laboratory, Pasadena, California, August 28, 1991.

[20] H. M. Pickett, J. C. Hardy, and J. Farhoomand, "Characterization of a Dual-Mode Horn for Submillimeter Wavelengths," *IEEE Transactions on Microwave Theory and Techniques*, vol. 32, pp. 936–937, August 1984.

[21] R. E. Cofield, "Field of View Calibration of the Microwave Limb Sounder on the Upper Atmosphere Research Satellite," *International Geoscience and Remote Sensing Symposium (IGARS)*, August 1994.

[22] J. W. Waters and R. F. Jarnot, *Science Requirements on the EOS Microwave Limb Sounder*, JPL D-14421, Rev. 2.0 (internal document), Jet Propulsion Laboratory, Pasadena, California, September 15, 1999.

[23] D. H. Martin and E. Puplett, "Polarized Interferometric Spectrometry for the Millimetre and Submillimetre Spectrum," *Infrared Physics*, vol. 10, p. 105, 1969.

[24] R. E. Cofield, T. A. Cwik, and N. A. Raouf, "Toric Offset Three-Reflector Antenna for an Advanced Microwave Limb Sounder," *Proceedings of SPIE*, vol. 4849, *Highly Innovative Space Telescope Concepts*, pp. 235–244, August 2002.

[25] E. Njoku, Y. Rahmat-Samii, J. Sercel, W. Wilson, and M. Moghaddam, "Evaluation of an Inflatable Antenna Concept for Microwave Sensing, " *IEEE Transactions on Geoscience and Remote Sensing*, vol. 37, no. 1, pp. 63–78, 1999.

[26] F. T. Ulaby, R. K. Moore, and A. K. Fung, *Microwave Remote Sensing, Active and Passive*, Addison-Wesley, Reading, Massachusetts, 1981.

[27] J. Johnson, J. Williams, L. E. Bracalente, F. Beck, and W. Grantham, "Seasat-A Satellite Scatterometer Instrument Evaluation," *IEEE Journal of Oceanic Engineering*, vol. 5, no. 2, pp. 138–144, 1980.

[28] F. Naderi, M. Freilich, and D. Long, "Spaceborne Radar Measurement of Wind Velocity over the Ocean: An Overview of the NSCAT Scatterometer System," *Proceedings of the IEEE*, vol. 79, no. 6, pp. 850–866, 1991.

[29] W. Crosswell, R. Roddewig, C. Pewsey, R. Moye, and W. Jones, "A Waveguide Fed Composite Horn Antenna," *Antennas and Propagation Society International Symposium 1988, International Symposium Digest: Antennas and Propagation*, vol. 1, pp. 338–341, 1988.

[30] Z. Hussein and Y. Rahmat-Samii, "Application of Cylindrical Near-Field Measurement Technique to the Calibration of Spaceborne Radar Antennas: NASA Scatterometer and SeaWinds," *IEEE Transactions on Geoscience and Remote Sensing*, vol. 37, no. 1, pp. 360–373, 1999.

[31] W.-Y. Tsai, J. Graf, C. Winn, J. Huddleston, S. Dunbar, M. Freilich, F. Wentz, D. Long, and W. Jones, "Postlaunch Sensor Verification and Calibration of the NASA Scatterometer," *IEEE Transactions on Geoscience and Remote Sensing*, vol. 37, no. 3, pp. 1517–1542, May 1999.

[32] C. Wu, Y. Liu, K. Kellogg, K. Pak, and R. Glenister, "Design and Calibration of the SeaWinds Scatterometer," *IEEE Transactions on Aerospace and Electronic Systems*, vol. 39, no. 1, pp. 94–109, 2003.

[33] M. Spencer, C. Wu, and D. Long, "Tradeoffs in the Design of a Spaceborne Scanning Pencil Beam," *IEEE Transactions on Geoscience and Remote Sensing*, vol. 35, no. 1, pp. 115–126, 1997.

[34] Z. Hussein, Y. Rahmat-Samii, and K. Kellogg, "Design and Near-Field Measurement Performance Evaluation of the SeaWinds Dual-Beam Reflector Antenna," *Antennas and Propagation Society International Symposium Digest*, vol. 2, pp. 852–855, 1997.

[35] CALIPSO Home page, Langley Research Center, Hampton, Virginia, site accessed August 4, 2005. http://www-calipso.larc.nasa.gov

[36] M. R. Schoeberl, "The AURA Mission and the A-Train," *The World Space Congress* (Houston, Texas), October 10–19, 2002.

[37] E. Im, S. L. Durden, C. Wu, and T. R. Livermore, "The 94 GHz Cloud Profiling Radar For the CloudSat Mission," *2001 IEEE Aerospace Conference Proceedings* (Big Sky, Montana, March 10–17, 2001), pp. 1803–1809, 2001.

[38] J. B. Mead, A. L. Pazmany, S. M. Sekelsky, and R. E. McIntosh, "Millimeter-Wavelength Radars for Remotely Sensing Clouds and Precipitation," *Proceedings of the IEEE*, vol. 82, no. 12, pp. 1891–1906, 1994.

[39] G. A. Sadowy, R. E. McIntosh, S. J. Dinardo, S. L. Durden, W. N. Edelstein, F. K. Li, A. B. Tanner, W. J. Wilson, T. L. Schneider, and G. L. Stephens, "The NASA DC-8 Airborne Cloud Radar: Design and Preliminary Results," *Proceedings of the International Geoscience and Remote Sensing Symposium (IGARSS)*, Singapore, August 3–8, 1997, pp 1466–1469, 1997.

[40] R. Meneghini and T. Kozu, *Spaceborne Weather Radar*, Chapter 2, Artech House, Inc., Boston, Massachusetts, 1990.

[41] S. Spitz, A. Prata, Jr., J. Harrell, R. Perez, and W. Veruttipong, "A 94 GHz Profiling Radar Antenna System," *2001 IEEE Aerospace Conference Proceedings* (March 10–17), pp. 2-685–2-694, 2001.

[42] G. M. Smith, C. P. Unsworth, M. R. Webb, and J. S. G. Lesurf, "Design, Analysis and Application of High Performance Permanently Magnetized, Quasi-Optical, Faraday Rotators," *1994 IEEE MTT Symposium Digest*, pp. 293–296, 1994.

[43] M. K. Hu, "Near-Zone Power Transmission Formulas," *1958 IRE National Convention Record* (New York, New York, March 24–27, 1958), Part 8, pp. 128–138, 1958.

[44] W. V. T. Rusch, T. S. Chu, A. R. Dion, P. A. Jensen, and A. W. Rudge, "Quasi-Optical Antenna Design and Applications," *The Handbook of Antenna Design*, edited by A. W. Rudge, K. Milne, A. D. Olver, and P. Knight, Peter Peregrinus Ltd., London, England, Chapter 3, 1982.

[45] A. R. Keith and A. Prata, Jr., "Interpolation of Reflector Surfaces Using Deformed Plate Theory,'' *Proceedings of the International IEEE AP-S Symposium* (Newport Beach, California, June 18–23, 1995), pp. 885–888, 1995.

[46] W. V. T. Rusch and P. D. Potter, *Analysis of Reflector Antennas*, Academic Press, New York, New York, 1970.

[47] *Ocean Surface Topography from Space: Missions–OSTM*, Jet Propulsion Laboratory, Pasadena, California, web site accessed August 4, 2005. http://topex-www.jpl.nasa.gov/mission/ostm.html

[48] *Ocean Surface Topography from Space: Missions–Jason-1*, Jet Propulsion Laboratory, Pasadena, California, web site accessed August 4, 2005. http://topex-www.jpl.nasa.gov/mission/jason-1.html

[49] *Ocean Surface Topography from Space: Missions–TOPEX/Poseidon*, Jet Propulsion Laboratory, Pasadena, California, web site accessed August 4, 2005. http://topex-www.jpl.nasa.gov/mission/topex.html

[50] R. E. Munsen, H. Haddad, and J. Hanlen, "Microstrip Reflectarray for Satellite Communications and RCS Enhancement or Reduction," U.S. Patent 4684952, August 1987.

[51] J. Huang, "Microstrip Reflectarray," *IEEE International Symposium on Antennas and Propagation*, Ontario, Canada, June 1991, pp. 612–615, 1991.

[52] D. M. Pozar, S. D. Targonski, and H. D. Syrigos, "Design of Millimeter Wave Microstrip Reflectarrays," *IEEE Transactions on Antennas and Propagation*, vol. AP-45, no. 2, pp. 287–296, February 1997.

[53] R. E. Hodges and M. S. Zawadzki, "Design of a Large Dual Polarized Ku Band Reflectarray for Space Borne Radar Altimeter," *Antennas and Propagation Society Symposium* (Monterey, California, June 20–25), vol. 4, pp. 4356–4359, 2004.

[54] R. E. Hodges and M. S. Zawadzki, "Scanning Properties of Large Reflectarray Antennas," *URSI Symposium Digest* (Monterey, California), June 20–25, 2004.

[55] R. E. Hodges and M. S. Zawadzki, "A Reflectarray Antenna for use in Interferometric Ocean Height Measurement," *2005 IEEE Aerospace Conference* (Big Sky, Montana), March 2005.

[56] J. Huang, "Bandwidth Study of Microstrip Reflectarray and a Novel Phased Reflectarray Concept," *1995 IEEE International Antennas and Propagation Symposium Digest* (Newport Beach, California, June 1995), pp. 582–585, 1995.

[57] D. M. Pozar, "Bandwidth of Reflectarrays," *Electronic Letters*, vol. 39, no. 21, pp. 1490–1491, October 16, 2003.